UNIVERSITÀ
DEGLI STUDI
FIRENZE

DOTTORATO DI RICERCA IN

International Doctorate in Atomic and Molecular Photonics

CICLO XXX

COORDINATORE Prof. Roberto Righini

Quantum Cascade Laser and Frequency Comb Synthesizer for Terahertz metrology

Settore Scientifico Disciplinare FIS/03

Dottorando
Dott. Campa Annamaria
Annamaria Campa
(firma)

Tutore
Dott. Bartalini Saverio
Saverio Bartalini
(firma)

Coordinatore
Prof. Roberto Righini
(firma)

Anni 2014/2017

International doctorate in atomic and molecular photonics

Quantum cascade laser and frequency comb synthesizer for Terahertz metrology

Abstract

The teraherz (THz) window of the electromagnetic spectrum has been an underexploited region for many years. Despite THz technologies did not experience the progress of the other spectral regions, THz is now emerging as a new promising frontier for many interdisciplinary research fields.
In THz range many molecules have strong rotational and rovibrational transitions with very large line-strengths with respect to infrared and microwave transitions. For this reason, THz main interest concerns molecular spectroscopy.
The work done during the three year PhD course addressed the development and application of THz spectroscopic tools. The aim was to improve the performance of the THz spectrometers developed in the past years by my advisor's group and based on THz Frequency Comb Synthesizer (FCS) in combination with THz Quantum Cascade Lasers (QCL).
To this purpose, the development of high-resolution THz spectroscopic techniques is a mandatory condition for further accuracy improvements.
In this thesis I describe my experimental activity and the studies performed during almost three years of work in the *Non-linear optics and precision spectroscopy* group at LENS, the *European Laboratory for Non-Linear Spectroscopy*. The research group is part of the Italian National Institute of Optics - CNR-INO).
The first part of this work concerns the study and the experimental realization of THz cavity resonators, that give access to longer interaction lengths between light and absorbing gas. They could also provide a narrow reference for a QCL, allowing a reduction of its free-running linewidth and the deployment of the most advanced cavity-enhanced techniques, such as cavity-ring-down spectroscopy. With achieved quality factors $Q \approx 10^6$, these THz cavities represent significant advance for the next generation of high-sensitivity and high-resolution THz spectroscopic experiments based on QCLs.
In the second part of the thesis the improvement of the metrological-grade system, based on a phase-locking of THz QCLs to a THz FCS is presented and discussed. In the past, such a system achieved an accuracy of 10^{-9} in the determination of the absolute frequency of a molecular transition.
Concerning the performance of the THz FCS, an upgrade of this system is proposed by changing the pump source. Then, both the efficiency of THz generation and the detection of beat-notes between the THz-comb and a THz-Quantum Cascade Laser are improved. In fact, the detection of the beat-note is the first step for the phase-locking of the QCL to the THz comb in order to stabilize and control the QCL emission.

With this improved metrological grade system, two different kinds of QCLs are characterized.
The first kind of QCL is based on intracavity difference-frequency generation. The work deals with the measurement of its free-running emission linewidth, its tuning characteristics, and its absolute emission frequency with an uncertainty of few parts in $4x10^{-10}$.
The second device is a broadband multimode QCL, specifically developed for a coherent comb-like operation thanks to the four-wave mixing processes occurring in its active region. At first, the absolute centre frequency of the QCL modes and its tuning characteristics are measured. Then, the focus is on the demonstration that the comb-like spectrum of the QCL can be, in principle, completely controlled, once provided the proper actuators.
Finally, a preliminary evidence of the coherence between the phases of different QCL modes is given by a direct simultaneous and real-time phase measurement, thus confirming the true comb-like nature of such devices.

Annamaria Campa

Contents

Dedicated to my lovely family

Introduction

The interest in terahertz spectroscopy raised during the mid 1970s. A decade later, as a result of the works of many researchers and scientists, advanced techniques in optical rectification and photoconduction were developed. In fact, these techniques represented the first milestone to produce directly THz radiation using broadband lasers.
Despite THz technologies did not experience the progress of the other spectral regions, THz is now emerging as a new promising frontier for many interdisciplinary research fields. In fact, the recent advances in generation and detection, and the constantly evolving technology of new materials, have stimulated an increasing number of applications, in fields as diverse as biomedical diagnostics, communication technology, security and defence. However, in the THz range many molecules have strong rotational and rovibrational transitions with very large line-strengths with respect to infrared (IR) and microwave (MW) transitions. For this reason, a key field for THz is molecular spectroscopy.
In recent years, among the different sources of THz radiation, Quantum Cascade Lasers (QCLs) are emerging as very promising sources not only for a practical exploitation of THz technology, but also for fundamental research, e.g. in the field of THz metrology. Indeed, the combination of inherently high spectral purity (with intrinsic linewidths as low as 100 Hz) and mW level output powers, makes QCLs the ideal candidates for high resolution and high sensitivity spectroscopy as well as for local oscillators in astronomical spectrometers.
Furthermore, another recent achievement has been reached by the extension to the THz region of Optical Frequency Comb Synthesizers (OFCSs), enabling direct and broadband phase or frequency referencing for any THz source and allowing to set up a new tool for high-precision measurements of THz frequencies.
The combination of the absolute referencing provided by THz combs with the mW level power of THz QCLs recently allowed to set up a metrological grade QCL-based THz spectroscopy with an unprecedented level of accuracy.

Outline of the thesis The work done during the three years PhD course addressed the development and application of THz spectroscopic tools. The aim was to improve the performance of the THz spectrometers developed in the past years by my advisor's group and based on THz Frequency Comb Synthesizer (FCS) in combination with THz QCL.

To this purpose, the development of high-resolution THz spectroscopic techniques is a mandatory condition for further accuracy improvements.
This thesis is structured as follows.
In **Chapter 1** a wide introduction to THz radiation is given. The most important THz sources (multiplied frequency chains, tunable far IR lasers, difference frequency generation processes) will be described, giving more details about the THz QCL, which is one of the main sources used in this thesis. The chapter ends with a description of the detection mechanisms used for THz light.
Chapter 2 focuses on THz cavities injected by a continuous-wave QCL. Indeed, the first important activity has been the study and experimental realization of THz cavity resonators, that give access to much longer interaction lengths between light and absorbing gas.
I will describe the three different cavity configurations: a V-shaped, a ring-shaped and a bow-tie resonator. After a theoretical background, the experimental implementation is shown. Each cavity is characterized, and its relevant parameters (Q factor, enhancement factor, optical coupling) are compared with the prediction of the theoretical model for the corresponding geometry.
In **Chapter 3** the second part of the thesis is discussed. The improvement of the metrological-grade system, based on phase-locking of THz QCLs to a THz FCS is presented. Such a system had previously achieved an accuracy of 10^{-9} in the determination of the absolute frequency of a molecular transition. The system consisted in a FCS generated by a non-linear crystal ($LiNbO_3$) by optical rectification of a Ti:Sapphire fs laser and the generation is based on Cherenkov emission.
The theoretical aspects of the non-linear process, that is the optical rectification, are explained in the first part of the chapter. Particular importance will be given to the experimental realization of the THz comb, the description of the non-linear crystal used and the characterization of the pump laser. Then, the alignment step and the characterization of the THz comb are described in details.
Furthermore, the metrological grade system has been employed for the characterization and exploration of the properties of THz sources. Indeed, the detection of a beat-note is the first step for the phase-locking of a QCL to the THz comb in order to stabilize and control the QCL emission. With this improved metrological grade system, two different kinds of QCLs have been characterized. This topic is presented in **Chapter 4**.
First, a brief introduction to the experimental setup and to the method used for the absolute measurement of the emission is given. Then, the characterization of the two different devices is presented in two separate sections.
The first device under analysis is a QCL based on intra-cavity difference-frequency generation, made in the Department of Electrical and Computer Engineering at the University of Texas in Austin. The results about the measurement of its free-running emission linewidth, its tuning characteristics, and its absolute emission frequency are described in detail.
The second device is a broadband multimode QCL, made in the Institute

of Quantum Electronics (ETH) in Zurich. The QCL has been specially developed for a coherent comb-like operation thanks to the four-wave mixing processes occurring in its active region. The absolute center frequency of the QCL modes and its tuning characteristics are measured. Moreover, further analyses demonstrate that the comb-like spectrum of the QCL can be, in principle, completely controlled, once the proper actuators are provided. A wide discussion on the achieved results is given.
Finally, a preliminary evidence of the coherence between the phases of the QCL modes is presented by a direct simultaneous and real-time phase measurement, thus confirming the true comb-like nature of such devices.

Chapter 1

Terahertz radiation

The terahertz region of the electromagnetic spectrum has been traditionally named as "far-infrared". In fact, THz radiation comprises electromagnetic waves situated between infrared and microwave frequencies.
Nowadays, the THz region has become one of the most exciting areas for the exploration of scientific phenomena. Nevertheless, terahertz remains one of the least developed spectral regions, despite its proven potentiality for a variety of applications.
In this chapter, I will provide an overview of the recent progress in the generation, detection and applications of the terahertz radiation. Then, I will classify the main methods for THz generation into four groups: direct laser action, frequency-down conversion of microwaves light, frequency-up conversion of visible/infrared light and free electron sources.
A wide description will concern a particular type of source, i.e. Quantum Cascade Laser (QCL). More details about its physical principles and its recent advances will be given, since QCL is the most promising source in THz range. For this reason, QCL is one of the main sources used in this thesis as well as the THz comb, generated by frequency-down conversion in nonlinear crystals, that will be widely described in Chapter 3.

1.1 Characteristics and motivations for generation of THz waves

Commonly, the THz window refers to the range 0.1-30 THz, even if waves within the band of frequency from 10 THz to 30 THz can be considered a portion of the mid-infrared band. For this reason, in this thesis, the THz radiation refers to the frequency range of $\nu = (0.1 \div 10)$ THz, corresponding to $\lambda = (3000 \div 30)$ μm.

As previously said, the light at these frequencies lies between the microwave and infrared regions of the electromagnetic spectrum (Fig.1.1). As a result, THz frequencies cannot be simply measured with conventional solid-state optical and electronic technologies, leading to the THz range being called the "THz gap". In the past this has involved difficulties in generation and detection of THz radiation. As a consequence, THz range has been an unexplored window for many years. On the other hand, despite the technological limitations, many research groups are working to improve THz technologies and to expand its potential role within many fields of research.

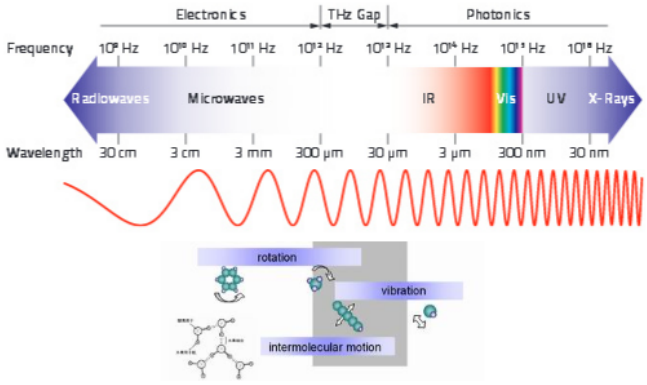

FIGURE 1.1: Electromagnetic spectrum. THz window is the bridge between the electronic approach and the photonic one.

In comparison with the microwave spectral region, THz waves have higher frequency, meaning that they can be used in higher-speed communications [1]. However, THz waves cannot propagate very far through atmosphere, because water vapor has a very high absorption coefficient in the THz region. In fact, except for narrow windows, water absorbs efficiently most of the THz region (Fig.1.2).

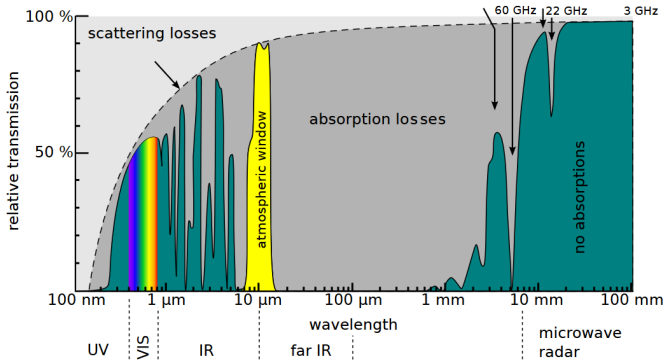

FIGURE 1.2: Relative transmission of the Earth atmosphere from UV to microwave frequency. Absorption losses prevail in the THz region.

Therefore, this feature involves a disadvantage from a technological point of view: experimental setups for THz radiation have to be very compact, avoiding long optical paths, to preserve most of the power. Alternatively, THz experimental setups are generally closed in boxes purged with nitrogen gas.
Although water absorption hinders the propagation of the THz waves, this remains a fundamental feature for applications in many fields. Indeed, THz waves are efficient to detect the presence of water, for example to discriminate hidden objects carried by a man since the water content of human body is about 60%.
Moreover, despite water absorption hampers to go deep in human body tissues (e.g. 4 mm is the maximum depth skin), imaging of these tissues at THz frequencies [2] can be useful for the identification of cancer boundaries [3].

The interest in medical field is enhanced by the fact that THz waves exhibit low photon energies (i.e. 4meV at 1THz), thanks to the high value of the associated wavelength. The result is that, unlike UV light or X-rays, THz is a non-ionizing radiation ensuring safe operation without damage biological tissues. This feature leads to the use of non-invasive imaging making THz waves useful for security applications, such as for airport security [4].
Whilst water absorption hinders THz propagation in hydrated substances, THz radiation can penetrate a wide variety of non-conducting materials, such as polymers, papers, ceramics, chemical powders and plastics. In order to exploit this feature, recent works have demonstrated the huge applications of THz imaging for cultural heritage preservation [5].
The main interest concerns the fact that THz-waves can pass through opaque dry media, i.e. that are opaque to visible and near-infrared waves. With this feature THz can be used to characterize the quality of paper products or also the defects of polymer and plastic materials with huge applications in food, plastic and paper industry.
These peculiarities involve many imaging applications, e.g. for the identification of substances such as drugs, explosives or weapons. Moreover, THz imaging retrieves strong applications in pharmaceutical industry with quality control and optimization of industrial manufacturing processes [6].
Astronomical and space science is another area of interest where THz radiation has an important role. Remote signals from astronomic systems [7] or chemical/biochemical molecules are identified thanks to their spectroscopic lines (fingerprint) in the THz region. Furthermore, terahertz thermal emission from gases in the stratosphere and upper troposphere, such as water, oxygen, chlorine and nitrogen compounds, is useful for the study of chemical processes related to ozone depletion, pollution monitoring and global warming [8].
Nevertheless, the primary application involving terahertz radiation is spectroscopy. Atoms in a molecule can bend, stretch and rotate with respect to one another, and these excitations are, to a large extent, optically active. Many important molecular low-frequency vibrational modes can be measured in the terahertz region from rocking, torsional, and conformational molecular changes. Linestrengths [1] of molecular transitions in THz are generally larger than in the microwave region and comparable with the strongest fundamental ro-vibrational transitions in the mid-IR [9]. Hz-linewidth transitions represent key molecular signatures and the THz range can well represent a *novel molecular fingerprint region*.
In the past, the lack of investigation of materials with THz-rays was due to the lack of convenient and high-power THz sources. To address the requirements for THz spectroscopic applications, several technologies providing tunable THz emission have been developed in the last few decades.
The advent of novel THz emitting laser sources, such as Quantum Cascade Lasers (QCLs), has assigned to the THz radiation a key role in high precision molecular spectroscopy. This was gained thanks to the improvement of the

[1] The intensity of a spectrum line

sensitivity and resolution of newly developed THz spectroscopic techniques to the levels reached in other spectral regions.

1.2 Methods for THz generation

The first method to generate terahertz light was set up at the end of the 1960s and in the early 1970s with the innovative works by Faries et al. [10], Morris et al. [11] and Yang et al. [12]. They first reported on tunable far-infrared radiation by optical difference-frequency-mixing in non-linear crystals. These works reported the possibility to generate THz radiation using non-linear crystals by difference-frequency process as well as parametric amplification and optical rectification [13], [14].
The improvement of pulsed laser technology rushed the development of different THz sources satisfying the requirement of wideband and high-power sources. As a result, the THz region became more attractive for the research of new methods for generating THz-waves based on picosecond and femtosecond laser pulses.
Since 2001, huge progress in THz field has been reported thanks to the development of compact laser sources, i.e. QCL. Nowadays, many different sources can generate THz-radiation either in short-pulse mode or Continuous Wave (CW) mode with an output power ranging from the nano-Watt level up to few Watts.
Nevertheless, the techniques to generate THz by multiplication of microwave frequencies or visible/infrared light reach very low power (100 nW) with very complex devices. For this reason, the generation of radiation at terahertz frequencies (1-10 THz) through high-efficiency room-temperature system allows to investigate and strengthen the role of terahertz in many applied fields. The importance of this topic concerns the necessity to explore the THz radiation in molecular spectroscopy, which is the THz key role. In this case, sources with higher and higher accuracy are required. Indeed, the possibility to identify the molecular transitions with higher and higher accuracy is a fundamental step to explore the energy level structure of molecules.
For the sake of clarity, examples of accuracy level for the most common THz sources are reported in table 1.1 along with the typical power and operating temperature.

TABLE 1.1: Examples of accuracy level, power level and operating temperature for the most common THz sources.

Source Type	Power	Accuracy($\nu > 1$ THz)	Operating Temperature (K)
TuFIR	100 nW	$10^{-10} - 10^{-11}$	300
Chains	$(1 \div 10)$ μW	$10^{-10} - 10^{-12}$	300
DFG	$(10 \div 15)$ μ W	$10^{-8} - 10^{-10}$	300
QCL	$(1 \div 100)$ mW	..	< 70

Albeit sources such as tunable-far infrared lasers (Tu-FIR), described in the following section, provide the highest accuracy, their emitting power is

very low. On the contrary, even if a QCL reaches high power, a metrological reference is required to achieve a high level of accuracy in spectroscopic measurements.
However, each source has advantages and disadvantages, therefore a compromise is reached for each kind of applications. For this reason, researchers are working on the realization of a compact, high-power, room-temperature and wideband source.
In the following sections, a description of these sources is presented. According to similarities in their physical mechanisms, the most common sources can be classified in direct lasing action, frequency-up conversion, frequency-down conversion and free electron laser sources.

Direct THz lasing action

Examples of coherent THz sources are optically pumped Far-InfraRed lasers (FIR). This kind of source is based on the emission of a radiation from a finite set of discrete molecular transitions.
The physical principle of a FIR source consists on the excitation of a molecular gas from its ground vibrational state, to a higher vibrational state performed by an external laser source. Population inversion is then obtained between two rotational levels within the excited vibrational state. More specifically, the wavelength of the exciting laser is tuned in order to coincide with an absorption line in the molecular gas that typically lies in the $10\mu m$ region. In this way, all infrared emitting lasers are potential candidates for FIR laser pumping.
Carbon dioxide (CO_2) lasers are emitters of coherent radiation at a large number of discrete wavelengths around $10\mu m$. Since typical molecular absorption bands lie within the CO_2 laser spectrum, FIR laser pumps are usually pumped by a CO_2 laser.
Heavy molecules preferentially produce longer wavelengths and, despite the abundance of observed FIR laser lines, only a limited number of them are intense enough to be used in practical applications.
Even if a FIR source provides high enough power levels, the disadvantage concerns the sophisticated operation and the intrinsically limitation due to the active media transition frequencies.

QCLs are very compact devices which are special kinds of semiconductor laser. Their structure is composed of alternated slices of semiconductor material, grown with epitaxial methods, that define quantum wells in which electrons make intersubband transitions. A detailed description of its physical principles is reported in section 1.3 since the device is widely used in this thesis.
This unipolar source emits a high power (100 mW), but operates at cryogenic temperatures. However, new designs of QCL, e.g. based on Difference Frequency Generation (DFG) [15], have just reached nitrogen temperature and other ones are reaching room temperatures [16].

Despite the cryogenic operation, THz QCLs have attracted considerable attention thanks to the high output power ($\approx$ 100 mW), spectral purity, stability, compactness and reliability. These features involve that QCLs have a realistic chance to achieve a deep impact on technological applications.
Among the crucial features of a THz QCL, a repeatable and tunable single-frequency emission has a fundamental role for several applications. To this purpose, many quantum-design related approaches, technological solutions and/or optical configurations have been recently tested to tune the emission frequency of THz QCL sources over quite a large bandwidth.
Applications of QCLs, as frequency and amplitude stabilized local oscillators (LO) in THz heterodyne spectrometers, have been only recently explored. In fact, only in the last few years, THz QCLs have recently shown a quantum limited linewidth of 100 Hz [17]. This means that, in principle, once properly frequency stabilized, QCLs can be used for ultra-high resolution molecular spectroscopy, paving the way to several key applications as well as to fundamental studies on molecules. Nevertheless, for many spectroscopic applications of practical interest, the crucial parameter is sensitivity, while resolution requirements are often not so challenging.

Frequency-down conversion

Beyond the possibility to generate THz with a direct lasing system, another approach concerns the conversion of higher or lower frequencies to THz frequencies. Methods about conversion of high frequencies involve the optical frequencies, e.g. visible or infrared light, converted in a non-linear media or in a photo-conductive antenna.

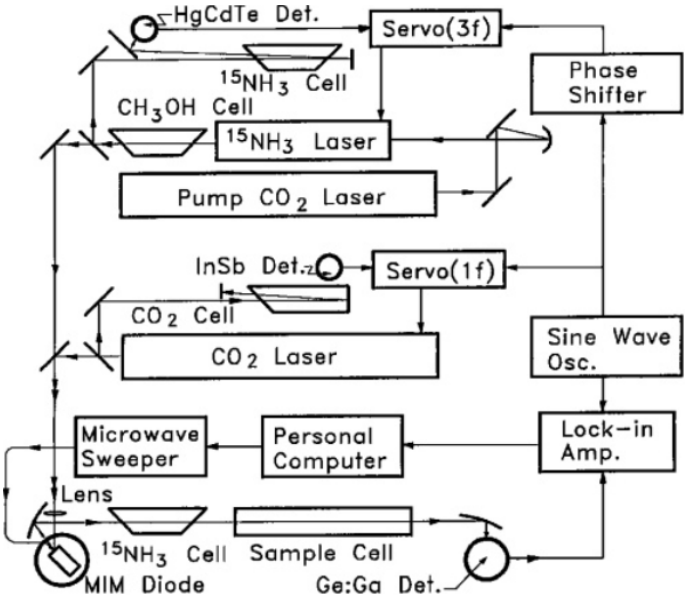

FIGURE 1.3: Sketch of a typical Tu-FIR spectrometer. Figure is reprinted from Ref. [18].

In the past, this approach was realized with the combination of two CO_2 lasers (Fig.1.3) and a RF signal in a metal insulator metal diode (MIM), which

generates a tunable frequency difference in the THz range [19].
Within this method, an alternative to the FIR lasers (Tu-FIR) is given by overcoming the limitation in tunability. In fact, by proper choices of laser lines, this approach demonstrated an overall tunability range from the microwave region up to about 9 THz. In this case, for fixed laser lines the continuous tunability was of 40 GHz and the emitted power was few hundred nanowatts.
The MIM diode was for many years a key device for frequency metrology, and it is interesting to compare its properties with present-day methods that consists on the frequency-down conversion of visible/infrared light in nonlinear media or in photo-conductive antennas (PCA).

Mourou et al. [20] reported the first works on PCA effect in the microwave (gigahertz) range. Later this effect was further expanded into the THz region by Auston's research groups at Bell Labs and Grischkowsky's group at IBM Watson Research Center in 1984. It was demonstrated that THz radiation can be generated from a biased PCA excited by laser beams.

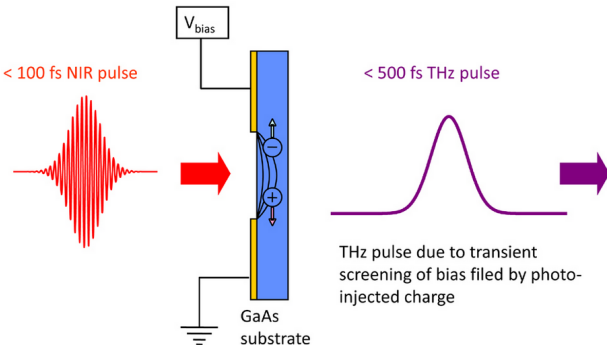

FIGURE 1.4: Photoconductive antenna (PCA). After the interaction of a near-infrared pulse on the PCA, a THz pulse is generated. Figure is reprinted from Ref. [21].

A PCA (see Fig.1.4) is composed of two metal electrodes deposited on a semiconductor substrate with a gap between the two electrodes. A voltage is applied across the electrodes to generate THz pulses and electric energy is stored in the gap area because the substrate is also semi-insulating.
When an optical beam illuminates the gap between the electrodes, photocarriers are generated and then a static bias field accelerates the free carriers. This photocurrent varies in time corresponding to the incident laser beam intensity [22].
The PCA is one of the most frequently used components for THz generation as well as detection. This device generates and detects THz pulses by transient photo-carriers induced with ultrafast laser pulses. Moreover, its peculiarity concerns the fact that PCA can be used as photomixer: two laser beams with different frequencies are mixed and a CW THz radiation is generated at the beat frequency.
Furthermore, the tuning range can be exceptionally broad providing a high-quality, tunable, dual-frequency laser system. Despite this, the primary disadvantage of this method is that the output power is relatively low compared

with other techniques of CW THz generation. Indeed, its optical-to-THz conversion efficiency is $10^{-6} - 10^{-5}$ and the typical output power is in the microwatt range.

Concerning the use of non-linear crystals, in 1983 D.H. Auston from Bell Labs first reported the generation of sub-picosecond electro-optic shockwaves in non-linear materials through the use of ultrafast laser pulse.
This technique generates THz radiation exploiting a non-linear medium in which incident electromagnetic waves undergo non-linear frequency conversion. More specifically, the interaction of two optical photons at two frequencies (ω_1, ω_2) with a non-linear crystal generates THz photons at frequency $\omega_T = \omega_1 - \omega_2$. Details about THz generation in non-linear crystals are described in Chapter 3.
The main limitation of these sources relies on the low power achieved, due to the low efficiency of the second order phenomenon implied in the generation. In order to improve the overall generation efficiency, different experimental setups have been tested. One favourable option is to enclose the generation crystal into an optical cavity for the visible/near IR radiation. These setups can achieve output powers of few mW at 1.9 THz with intra-cavity power as high as 500 W. It is worth noting that the generated power scales with the product of the intensities of the two pump beams. As a consequence, the emitted THz power can be also enhanced by confining the THz radiation in a small space. To this purpose, ridged and implanted waveguides have been realized, achieving efficiencies of 10^{-9} in the THz generation.

Frequency-up conversion

The most common method useful to obtain low-frequency terahertz radiation (0.5-2 THz) is the non-linear multiplication of a lower frequency oscillator (100-200 GHz) by chains of Schottky doublers and triplers. The key element of the THz generation by frequency-up conversion of lower frequencies, i.e. the electronic ones (microwave), is a solid-state diode. Indeed, this method consists on the use of microwave synthesizer that can generate output signals in the frequency range of 10-100 GHz. Then, the signal is multiplied by the solid-state THz sources using Schottky barrier diodes.
Conceptually, the frequency multiplication of microwaves is analogous to the harmonic generation of optical waves in a non-linear crystal. In a frequency multiplier, Schottky diodes behave as non-linear media, converting the incoming microwaves into their harmonic waves.
Such a device delivers continuous-wave narrowband power with limited tunability ($<< 10\%$) resulting suitable as a LO for mixing. However, the output power falls off rapidly with increasing frequency due to reduced multiplication efficiency. The power reaches sub-milliwatt level for $f > 1$ THz and microwatt level or below for $f > 1.6$ THz.
Despite these limitations, a relevant number of physical results on molecules and atoms could be achieved. Moreover, these chains are intrinsically easy to be referenced to primary frequency standards, in order to precisely know

their emission frequency.

Free electron type source

In a Free Electron Laser (FEL), electron accelerator produces extremely bright THz radiation using relativistic electrons. This method is based on a femtosecond laser pulse that triggers an electron source to generate an ultrashort pulse of electrons. After being accelerated to a relativistic speed, the electrons are smashed into a metal target, or forced into circular motion by a magnetic field. Coherent THz radiation is generated by this transient electron acceleration.
The fundamental physical process of FELs is applicable to a wide spectral range from microwaves to X-rays. The prime advantage deals with their broad and continuous tunability. In addition, the radiation wavelength is determined by a small number of parameters such as wiggler period, magnetic field strength and electron beam energy. FELs can also produce high-power radiation, because electrons are the only medium involved in lasing. This is the reason why they are free of the conventional problems of high-power laser systems, such as thermal lensing and material damaging.
THz generation mechanism of FEL is similar to THz system based on backward wave oscillators (BWOs). Indeed, these two methods are based on the modulation of an electron beam by a periodic structure. A BWO has a metal grating, while a FEL consists of a magnetic array. On the other hand, in a BWO THz radiation can be generated by relativistic electrons: an electron beam interacts with a travelling electromagnetic wave in an electron vacuum tube [23].

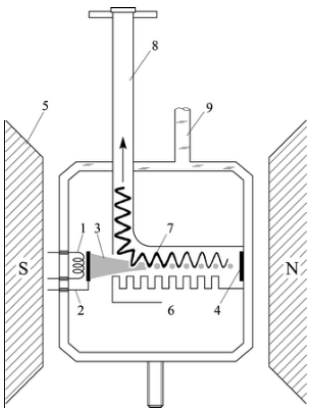

FIGURE 1.5: Schematic representation of the backward wave oscillator. Figure is reprinted from Ref. [24].

More specifically, in a BWO a heated cathode emits electrons that are accelerated by a DC electric field applied between the cathode and the anode. In the tube a grating, with a periodic structure, modulates the energy of the electron beam inducing a spatial modulation of the longitudinal electric field. In this way, bunched perturbation of the electrons excites surface waves on the periodic structure (Fig.1.5).

When the electron beam velocity matches the phase velocity of the surface wave, the kinetic energy of the electrons is transferred coherently to the electromagnetic wave. Consequently, the frequency of the electromagnetic wave is determined by the electron velocity and can be tuned by adjusting the bias voltage. Since the group velocity of the surface wave moves opposite to the phase velocity, the energy transferred to the field is transported and amplified in the backward direction. A cavity coupled to the waveguide is used to extract the radiation.
BWOs can operate in the THz region at moderate power levels (1 - 100 mW), with an accelerating potential in the range 1 to 10 kV and axial magnetic field of about 1 T. They can be tuned over tens of GHz by varying the accelerating potential. Several BWOs can be implemented in an integrated system to cover a wide frequency range extending from 30 GHz to 1.2 THz and used in spectroscopy [25].

1.3 THz Quantum Cascade Laser

Availability of a new generation of compact, reliable THz sources is the key for the development of the underdeveloped THz range. In this context, THz emitting Quantum Cascade Lasers are proving to be good candidates to fill this gap.
As previously said, QCL emission is based on transitions inside its conduction band. The use of intersubband transitions for radiation amplification was first proposed in 1971 by Kazarinov and Suris in a superlattice structure [26]. First described by Esaki and Tsu in 1970, a superlattice is a periodic repetition of two semiconductor material layers of different composition, i.e. a sequence of quantum wells and barriers.
The first demonstration of a QCL technology at infrared light and cryogenic temperatures was done in 1994 by Capasso's group at Bell Laboratories [27]. The manufacture of superlattice and quantum well semiconductor structures was made possible thanks to molecular beam epitaxy technology, allowing to grow layers as thin as several monolayers with atomic precision.
Some years later, in 2001 Kohler et al., from Alessandro Tredicucci's group in Pisa [28], demonstrated the first terahertz quantum cascade laser operating at 4.4 THz ($\lambda = 68\mu m$). Lasing was observed up to 40 K, with a maximum duty cycle of 10%, while a peak power of 2.5 mW was observed in pulsed mode at 8 K. The structure was composed of a new chirped superlattice active region placed in a new type of a low-loss waveguide.
Since their first demonstration, the performance of THz quantum cascade lasers improved dramatically. Indeed, a huge progress concerns the output power (>100 mW), operation temperature, spectral purity, frequency tunability, stability, compactness and reliability, making QCL technology the more attractive choice across the far infrared.
Whilst the band gap of many semiconductors is appropriate for mid and long-wave emitters, solid-state physics does not allow these materials to be very optically active as emitters. The reason is that, at longer wavelengths,

this energy is often re-absorbed by another charge carrier and eventually transferred to heat. Differently, for near-infrared lasers, when electrons from the conduction band relax to the valence band (across the band gap) the energy is typically transferred to a photon. On the contrary, in QCLs, unlike in a laser diode, an electron remains in the conduction band after emitting a laser photon. The electron can therefore easily be recycled by being injected into an adjacent identical active region, where it emits another photon, and so forth. This quantum-based transport, combined with the cascaded emitter design, is responsible for the name of this laser.
For this type of laser, the material composition mainly controls the emission energy. In an intersubband emitter, a new "band gap" between quantum well subbands defines the emission energy. Since the spacing between subbands is controlled by the quantum well thickness, the emission energy or wavelength can be tuned over a very wide range without changing the material composition.
This technology can also access terahertz spectral regions (30 to 300 μm wavelengths) by making the subband spacing extremely small (< 40 meV); however, it requires cryogenic cooling to operate (T< 178 K).
The only exception, so far, is a device that uses non-linear conversion of two mid-wave QCLs to achieve operation at room temperature, as will be described with more details in Chapter 4. Unfortunately, the power output is still many orders of magnitude lower than stand-alone midwave QCLs. Still, as midwave QCL performance increases, this translates into an improvement of this non-linear technique as well.

1.3.1 Active region design

In a QCL with a superlattice structure, a single period is composed of an injector, an injection barrier, and an active region. The latter, comprising multiple QWs, is the fundamental part where intersubband transitions give rise to radiative emission.

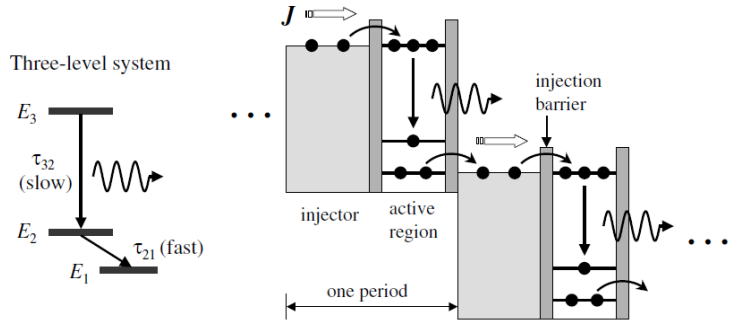

FIGURE 1.6: On the left: a three-level system is shown. On the right: schematic representation of the QCL period made of an injector and an active region. The cascade effect is highlighted. Figure is reprinted from Ref. [22].

Laser action in typical QCLs is based on a three-level system (Fig.1.6) where a population inversion is created between levels 3 and 2. The laser photon is emitted in the transition between states 3 and 2, which is controlled primarily by the two wider wells thickness.
Moreover, the lifetime of level 3 is designed to be much longer than that of state 2, the reason is to achieve a large population inversion between states 3 and 2.
A static electric field biases the superlattice structure. The electric field is adjusted so that level 1 of an active region is aligned with level 3 of the next period. Then, the electrons used in one active region are injected into and recycled in the next period. This end state 1 is positioned approximately an optical phonon energy ($\sim$ 34 meV in InGaAs/AlInAs materials) below level 2. Consequently, electrons in this level resonantly scatter to energy level 1 by emitting an optical phonon, an extremely fast process characterized by a relaxation time of the order of 0.1-0.2 ps.

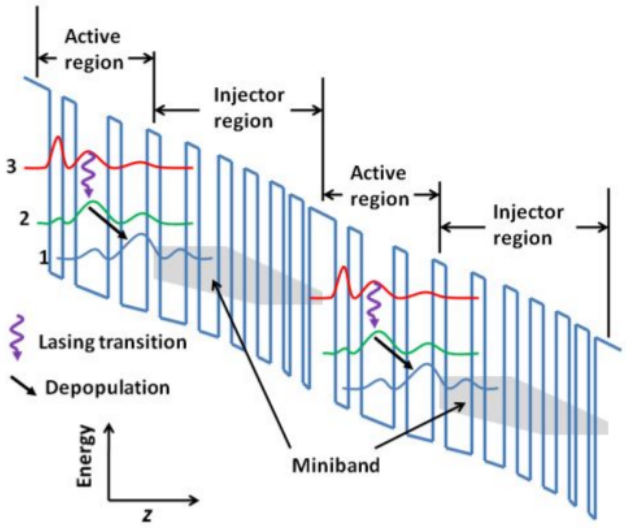

FIGURE 1.7: Schematic representation of the superlattice potential and of miniband.

To ensure lasing however, electrons must not escape by tunneling from the upper laser state (E_3) to the quasi-continuum, which would reduce its population. For this reason, the injector stage is designed as a superlattice with an energy gap (minigap) in correspondence of the upper energy level E_3. The miniband, designed to face E_2 and E_1, instead facilitates electron escape from the active region by preventing their accumulation in those states. More specifically, the sequentially thin ($\sim$ hundreds of Angstroms) semiconductor layers introduce discontinuities in the band edges, leading to the quantum confinement of carriers in the growth direction. As a result, the band breaks up into "subbands", where the energy is quantized in the growth direction. In fact, in a superlattice the single well states couple together to form "minibands" separated by a "minigap" (Fig.1.7). To first order, the minigap is determined by the well width and the miniband width is determined

by the barrier thickness.
Beyond this basic design principle, the full laser design must consider the actual emitting wavelength, operating conditions and operating temperature. Like many devices, the QCL will experience some performance degradation with temperature. In addition, QCL also requires detailed optimization for high-temperature operation such as the introduction of strategic energy barriers to minimize thermal leakage.
At this time, three main active region types have been successfully used in terahertz QCLs: chirped superlattice, bound-to-continuum, and resonant phonon.

Chirped superlattice

Historically, the first THz QCL was based on a chirped superlattice active region design, previously used for mid-infrared QCLs. This design consists of quantum well states forming minibands separated by minigap. The minigap is determined by the well width and the miniband by the barrier thickness.

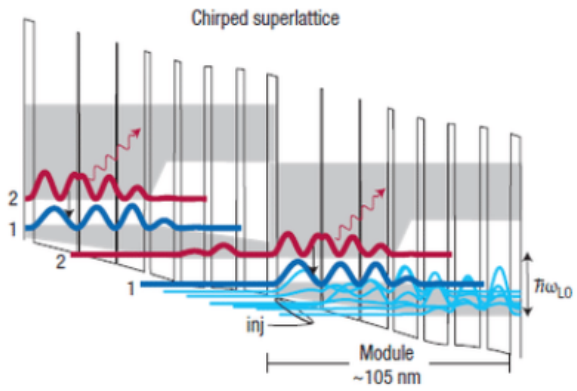

FIGURE 1.8: Schematic diagram of a chirped superlattice active region design. Figure is reprinted from Ref. [29].

With this design the radiation emitting transition takes place between the bottom state of the upper miniband and the top state of the lower miniband (Fig.1.8). THz photons are emitted because of the electron scattering from the upper to the lower miniband. In fact, population inversion occurs for the intraminiband scattering of electrons, which is a process much faster than inter-miniband scattering.

Bound-to-continuum

After many advances in QCL design, the chirped superlattice has led to a new design: the bound-to-continuum active region. In that case, the upper radiative state is designed to be an isolated state differently from the previous case in which it was a miniband. In this way, a more diagonal radiative transition and a reduced oscillator strength are achieved.

Moreover, the injection states couple more strongly with the upper state with respect to the miniband configuration and the injection process results

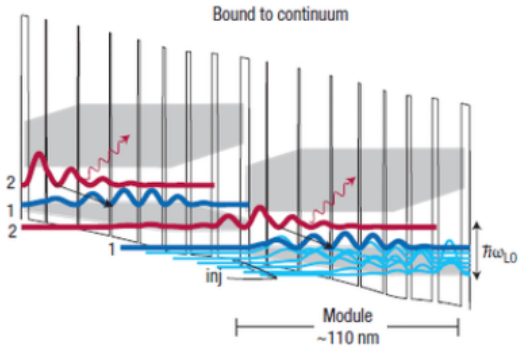

FIGURE 1.9: Schematic diagram of a bound to continuum active region design. Figure is reprinted from Ref. [29].

more efficient (Fig.1.9). It follows that the temperature and power performance are improved.

Resonant phonon

The resonant phonon design is based on a combination of resonant tunneling and direct electron longitudinal optical phonon scattering. This structure allows the depopulation of the lower radiative states rather than the upper one, because of the close subband energy spacing.

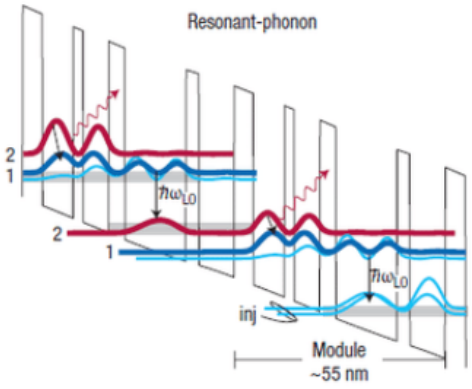

FIGURE 1.10: Schematic diagram of a resonant phonon active region design. Figure is reprinted from Ref. [29].

This design is characterized by a strong overlap between the lower radiative states and the injector states differently from the upper states, which have a little overlap with the injector states (Fig.1.10). Therefore, the lower and injector states have a large energy separation, providing intrinsic protection against thermal backfilling of the lower radiative states. Moreover, the design allows higher temperature operation of laser at longer wavelengths.

1.3.2 Waveguide design and beam quality

One of the critical components (beside the gain medium) of a laser is the waveguide used to confine the radiation and to provide optical feedback.
As such, the full structure often has a mean thickness in the range 4-10 μm, depending on the emission wavelength. After standard photolithography, etching and metallization to define the overall device dimensions and current injection path, the full device is only about 100 μm thick (including substrate) and takes up an area lower than 0.001 cm^2.
Generally, for a waveguide the threshold condition is expressed as follows:

$$\Gamma g_{th} = \alpha_\omega + \alpha_m \tag{1.1}$$

where Γ is the confinement factor of the mode in the active region, g_{th} is the threshold bulk gain of the active region α_ω is the waveguide absorption loss and α_m is the mirror loss. The latter is due to the reflectivities (R_1, R_2) of the mirrors that define the waveguide cavity (with length L) and is expressed as:

$$\alpha_m = -\frac{ln(R_1 R_2)}{2L} \tag{1.2}$$

The most used designs are the metal-metal waveguide, the semi-insulating surface plasmon and the distributed feedback (DFB) (see Fig.1.11).

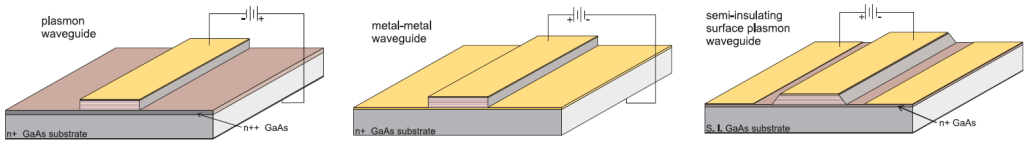

FIGURE 1.11: Schematic diagram of the most used waveguide designs. Figure is reprinted from Ref. [30].

The semi-insulating surface plasmon waveguide generates a far field beam pattern with a more directional beam due to the large emitting area. Furthermore, the output power results high for the wide ridge, which minimum dimensions must be carefully chosen to avoid the modes to be squeezed into the substrate. This condition sets a limit in the device size and high temperature performance.
The metal-metal waveguide is based on a couple of metal layers for mode confinement commonly used at microwave frequencies. The structure causes highly divergent far-field beam for the larger free space waveguide with respect to the waveguide dimension. Because of the interference of the coherent radiation emitted from the laser bar, the far-field beam shows ringlike interference patterns. In this way, low power coupling efficiency is achieved through guiding THz QCL radiation to a Gaussian beam and phase sensitive detection, like a superconducting HEB mixer.
Finally, the DFB lasers provide a feedback mechanism based on backward

Bragg scattering from periodic perturbations of the refractive index or the laser gain medium. The main advantage is the strong spectral selection useful for a single-mode operation.

1.3.3 New frontiers of THz QCLs

After two decades from their invention, quantum cascade lasers have reached impressive performance levels in the terahertz (0.3-10 THz) spectral region. Different works on the QCL design have reached high performance in each one of their characteristics.

CW THz QCLs have established themselves as versatile narrow-linewidth (LW) sources with applications in high-resolution spectroscopy, gas sensing, and heterodyne detection.
To date, cryogenically-cooled THz QCLs have shown high spectral purity with intrinsic LWs as low as 100 Hz.
The knowledge of the intrinsic linewidth, which is related to the uncertainty principle of quantum mechanics, is the main aspect for the determination of the maximum achievable spectral resolution and coherent length in a free-running laser. Recently, an experimental evaluation of the intrinsic linewidth has been performed with the measurement of its frequency-noise power spectral density (FNPSD) exploring the spectral purity of a THz QCL. Details in the frequency domain are retrieved by means of intensity measurements: detectable variations are revealed, corresponding to the laser frequency fluctuations. These measurements led to a full-width half-maximum (FWHM) $\delta\nu = 90 \pm 30$ Hz [31].
THz QCLs typical free-running LWs are dominated by excess frequency noise, leading to broadening up to several hundred kHz. If frequency or phase are stabilized, these sources have achieved fast LWs of 30-60 kHz, 20 kHz and 6.3 kHz, depending on the quality of the reference and of the locking setup. Narrow LW THz QCL sources are highly desired for a number of applications, including heterodyne detection for far-infrared astronomy, molecular frequency metrology, high-resolution coherent imaging and telecommunications, where they can provide the carrier wave for broadband wireless links.

Right from the beginning, experiments on frequency and phase stabilization of THz QCLs have involved some secondary frequency standards.
In 2005, phase-lock of a 3 THz QCL to the 3.1059368 THz line of a methanol gas laser was proven [32] and, in 2009, frequency stabilization of a single-mode THz QCL against the 2.409293 THz line of a CH_2DOH gas laser was demonstrated [33]. In both cases, a narrowing of the beat signal was observed (65 and 3 kHz, respectively).
The first THz QCLs locked to microwave-driven harmonically generated THz sources were demonstrated at 1.5 [34], 2.7 (phase locks) [35] and 2.3 THz (frequency lock) [36]. Despite the high complexity, the high electrical power consumption and the very low efficiency with a few pW radiation power, the advantage of using these kinds of sources concerns the fact that they provide

very narrow and absolute-frequency reference. This peculiarity makes these sources suitable for mixing with the THz QCL in a sensitive detector, such as a hot-electron bolometer.
Frequency-locking of a THz QCL to a molecular reference was demonstrated in a first-derivative, direct-absorption spectroscopy configuration, without any significant narrowing of the QCL emission [37].
Recently, phase-locking to an OFCS was achieved by locking a 2.5 THz QCL to the n-th harmonic of the repetition rate of a mode-locked erbium-doped fiber laser (described with more details in Chapter 3).
By implementing a technique first reported by Loffler et al. [38], the comb generated by the mode-locked laser was mixed in a non-linear crystal with a CW THz QCL, thus generating THz sidebands around the near-IR carrier. The beating between the original comb and its shifted replicas provides the signal for closing the phase-lock loop, which is the one used in this thesis. A similar method, but using a photoconductive antenna instead of electro-optic detection, was presented one year later [39].

Despite the tremendous progress, THz QCLs operation is still limited to temperatures of 200 K in pulsed mode and slightly below 130 K in CW operation. Room-temperature (RT) operation is, however, highly desired for applications and largely simplifies any experimental setup.
To address the need for RT-THz sources, an alternative approach has been implemented based on intra-cavity difference-frequency generation (DFG) in mid-IR QCLs. With the introduction of a Cherenkov-effect scheme for THz extraction, THz DFG-QCLs have made dramatic progress in the last five years. This foundational approach has several appealing aspects: since the intersubband transitions within the QCL material itself provide the second-order non-linearity ($\chi^{(2)}$), the sources can be operated at RT, similarly to other mid-IR QCLs. Additionally, wide THz tunability can be obtained with only modest tuning of the mid-IR modes. Depending on the mid-IR pump spacing, THz emission can be varied in the entire 1.6 THz range and beyond, with limitations set only by the material losses and reduction of THz DFG efficiency.
Wide-range frequency tuning, spanning several THz at room temperature based, on composite DFB QCL arrays, or external cavity technique, has been demonstrated.
A careful characterization of these devices, regarding both their tunability characteristics and their spectral purity, has been very recently performed [40], showing that not only these devices are able to work at room temperature, but that they are also suitable for metrological grade applications. More details about these measurements can be retrieved in Chapter 4.

Single mode THz QCLs have already shown their huge potential for metrological grade THz spectroscopy. Furthermore, a new interesting and promising technology for THz high precision spectroscopy is the continuous-wave multimode broadband QCL, the operation of which has only recently been demonstrated.

Particular design of THz QCLs can define gain spectrum to be broadband over a range even larger than 1 THz or to be electrically tunable over a 240 GHz bandwidth.
A broadband gain medium is desirable for a wide range of applications. To this purpose, recent kinds of QCL have a comb-like structure driven by ultrafast non-linearities (four-wave mixing) in the active region itself.
At terahertz frequencies, comb operation is also favoured by the longer lifetimes of the upper state of the optical transition at those frequencies. The ultrabroad gain bandwidth is achieved by fully exploiting the quantum engineering of intersubband transitions, integrating in the same laser ridge (resonator) different designs of a quantum cascade structure, tailored for different frequencies.
First demonstrated in mid-IR QCLs, this heterogeneous cascade concept has also been successfully implemented in terahertz QCLs. These sources show a comb emission regime with hundreds GHz spectral coverage and their comb-like features and controllability have been characterized during the work of this thesis and widely described in Chapter 4.

1.4 Detection of THz light

Historically, chemists and astronomers made greater use of the THz detectors for the spectral characterization of the rotational and vibrational resonances and thermal emission lines of simple molecules. In fact, THz receivers are employed to study the trace gases in the upper atmosphere, as ozone and many gases (chloride monoxide) involved in ozone depletion cycles. Up to date terahertz receivers are used in many fields. In this section, a description of the detectors used in this thesis is given.

In this work, pyroelectric detectors have been largely used to collect THz light. These are thermal detectors, based on a temperature change due to the incident optical power that leads to a variation of the detector properties. More specifically, the variation concerns the polarization of the pyroelectric-material and consequently a voltage is detected.
In other words, the pyroelectric detector can be described as a small capacitor with two conducting electrodes mounted perpendicularly to the direction of spontaneous polarization. When the radiation hits the detector, the change in polarization appears as a charge on the capacitor and a current is generated. The magnitude of this effect depends on the temperature rise and on the pyroelectric coefficient of the material.
Despite this detector operates at room temperature, its response time is slow so light has to be modulated, and the detector sensitivity is limited by amplifier noise. Response speed can be engineered making pyroelectric detectors useful for fast laser pulse detection; however, this comes with a proportional decrease in sensitivity.

The second kinds of detectors used in this thesis are bolometers.
The sensible element of a bolometer is a resistive element manufactured from a material with a very small thermal capacity and large temperature coefficient, so that the absorbed radiation produces a substantial change in resistance. In other words, radiant power produces heat within the material, which in turn produces the resistance change and there is no direct photon electron interaction. Most bolometers in use today are of the thermistor type, made from oxides of manganese, cobalt, or nickel.
For istance, one type of bolometers used in the thesis is a THz-camera, composed of uncooled microbolometer placed in a matrix array. This type of detector has a sensitivity over a wide spectral range, providing live video images.

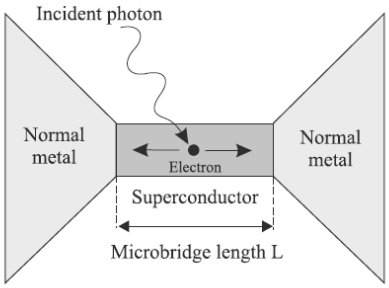

FIGURE 1.12: Schematic representation of the hot electron beam bolometer sensor.

However, special kinds of bolometers operate at cryogenic temperatures, enabling significantly greater sensitivity.
In the case of super-conducting bolometers, the detector is cooled down in order to reach the superconductive transition. Small temperature changes, caused by the absorption of incident radiation, strongly influences the resistance of the biased sensor near its superconducting transition.
In this type of device, hot electrons transfer their energy to the phonons. More specifically, after photon absorption, a single electron initially receives the photon energy $h\nu$. The latter is rapidly shared with other electron, producing a slight increase in the electron temperature. Then, the electron temperature subsequently relaxes to the bath temperature through emission of phonons. The result is that the detector time constant is related to electron relaxation time, resulting in a faster detector with respect to the ordinary bolometers (Fig 1.12) but requiring cooling to liquid helium temperatures.
These kinds of bolometer, called Hot Electron Bolometers (HEB), belong to the group of square-law mixers.
Typically, HEB sensor is much smaller than the received wavelength. Therefore, an antenna and associated coupling circuit are needed to bring the radiation to the detector, coupling power to a small thermally absorbing region.
Generally, the HEB is used for its smaller Noise Equivalent Power (NEP) since for uncooled detectors is typically from 10^{-10} to $10^{-9}W/Hz^{1/2}$.

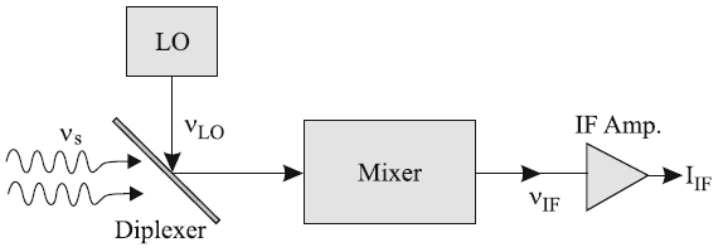

FIGURE 1.13: Heterodyne detector. The signal, with a frequency of ν_s, and the local oscillator, with a frequency of ν_{LO}, are mixed on the detector. The latter generates a displaced a signal with a frequency of ν_{IF} thanks to a beam splitter or a diplexer. Figure is reprinted from Ref. [41].

HEBs can be used as heterodyne detector, as done in this work. The signals with THz frequencies are down converted to intermediate frequency (IF), preserving the amplitude and phase information of the incoming radiation.
The basic element of mm or sub-mm heterodyne detector is a mixer, on which the signal, with a frequency ν_s, and the local oscillator, with a frequency ν_{LO}, are sent for generating a signal at the intermediate frequency $\nu_{IF} = |\nu_s - \nu_{LO}|$ (Fig.1.13). Its basic component is the non-linear mixing element (detector) where the signal and LO radiant powers are coupled, using some kind of diplexer or a beam splitter. The latter one is useful to spatially combine the signal beam and LO beam.
The primary advantage of heterodyne detection systems is that the frequency and phase information at the signal frequency ν_s is converted to the frequency ν_{IF}. The latter is in much lower frequency band ($\nu_{IF} \ll \nu_s$), appropriate to the time response of the electronics. This transformation ($\nu_s \rightarrow \nu_{IF}$) is called heterodyne conversion. Differently, if the signal and LO frequencies are identical, then $\nu_{IF} = 0$ and the obtained signal degenerates to DC. This type of detection process is called homodyne conversion.

Chapter 2

Spectroscopic tools: cavities for THz light

Since their invention, optical resonators have represented an important optical tool for their role as the basic element for laser action, for the investigation of coherent radiation properties and for all purposes that require control and enhancement of laser beams. To this purpose, the requirement of high performance resonator is mandatory and consequently optical cavities are designed to have a large Q-factor and finesse. These are the two physical quantities that better describe how a cavity works, i.e. the quality of a cavity. In the actual state-of-the-art, the physics of resonators and their experimental realization have been well investigated almost all the electromagnetic spectrum. Indeed, optical resonators are well established tools commonly used in spectroscopy [42], [43]. They have widespread applications over the whole electromagnetic spectrum, from MW [44] to UV [45], while record level optical finesses were achieved in the visible/near IR, especially thanks to the advent of whispering gallery mode resonators [46]. Despite their widespread use, in the terahertz portion of the electromagnetic spectrum ranging from 0.1 to 10 THz there is still a lack of such tools. In fact, cavities for terahertz light have been only developed in the last few years, with the achievement of very low finesses. This has to be related to the fact that, for many years, the THz range has been a largely unexploited spectral region: technological advances in the exploitation of this range are not comparable to those achieved in other spectral regions.
In this chapter, the fabrication of wire grid polarizer based THz resonators is reported. These cavities have been successfully coupled with the radiation of a QCL working around 2.5 THz. Three different cavity configurations are proposed and experimentally demonstrated: a V, a ring and a bow-tie geometry. In the first section of this chapter, a theoretical dissertation about Gaussian beams and optical cavities, and an analysis of the cavity losses and parameters is presented. Each cavity has been characterized, and its relevant parameters (Q factor, enhancement factor, optical coupling) have been compared to the one obtained by simulations. Furthermore, by simultaneously coupling the QCL to V and ring cavities, the effect of the optical feedback from the V-shaped cavity to the laser is investigated. This gives a preliminary evidence of the possibility of optically locking the QCL to a cavity, with considerable benefits in terms of frequency stability and emission narrowing. In the second section, a new configuration is proposed, merging the best

properties and overcoming the limitations of the previous geometries in the perspective of obtaining a higher finesse. In this perspective, the use of a ring geometry can minimize the effect of the optical feedback. Indeed, the use of optical elements that work at very small angle, such as spherical mirrors, reduces the dimension of the cavity. Immediately, the solution is a bow-tie configuration which is the most common configuration in the other spectral windows.

2.1 Theory of Gaussian beams

Laser beams are often described as Gaussian beams, a formalism that describes the intensity profile with a Gaussian function.
For the sake of clarity, in this thesis the z-axis is taken as the direction of the optical axis, which is the propagation axis of the beam.
A detailed description of the Gaussian beam comes from the propagation of its electric field. Analysing a monochromatic beam (with $k = 2\pi/\lambda$), the complex amplitude of the electric field is given by:

$$E(r,z) = E_0 \frac{w_0}{w(z)} exp\left(-\frac{r^2}{w(z)^2}\right) exp\left(-jkz - jarctan\left(\frac{z}{z_R}\right) + \frac{kr^2}{2R(z)}\right) \tag{2.1}$$

where E_0 is the peak amplitude and $w(z)$ is the beam radius. The latter corresponds to the distance from the beam axis where the intensity drops to $1/e^2$ of the maximum value, defined as follows:

$$w(z) = w_0\sqrt{1 + (z/z_R)^2} \tag{2.2}$$

where w_0 is the minimum spot size, expressed as:

$$w_{0i}^2 = \frac{\lambda z_{Ri}}{\pi} = \left(\frac{\lambda}{\pi\theta_i}\right)^2 \quad (i = x, y). \tag{2.3}$$

In the previous equation, z_R is the Rayleigh length that determines the length over which the beam can propagate without diverging significantly.
Referring to eq.2.1, $R(z)$ is the curvature radius of the wavefront that evolves according to:

$$R(z) = z\left(1 + \left(\frac{z}{z_R}\right)^2\right) \tag{2.4}$$

while the term:

$$\Delta\psi(z) = arctan\left(\frac{z}{z_R}\right) \tag{2.5}$$

is also called Gouy phase shift. It describes the phase shift experienced by the Gaussian beam with respect to that of a plane wave with the same optical frequency.

Another important parameter for a Gaussian beam is its divergence, defined in the far field (i.e., for z values much larger than z_R) by the relation:

$$\theta = \frac{\lambda}{\pi w_0} \tag{2.6}$$

The smaller is the waist radius and the longer is the wavelength, the larger will be the divergence of the beam far from the waist.
By considering the beam power P across an arbitary plane at z, the intensity of the electric field, in spherical coordinates ($r = \sqrt{x^2 + y^2}, z$), is written as:

$$I(r, z) = \frac{2P}{\pi w^2(z)} exp\left(-2\frac{r^2}{w^2(z)}\right) \tag{2.7}$$

However, in this experiment, the beam emitted by a QCL is approximated an elliptical Gaussian beam with different propagation parameters in the (x, z) plane. The latter is defined as the plane containing the growth axis x of the laser gain medium, and in the (y, z) plane orthogonal to it. Consequently, the focus positions for both directions are not equal and the beam is called astigmatic. In this case, eq.2.7 is changed in:

$$I(x, y, z) = \frac{2P}{\pi w_x(z) w_y(z)} exp\left(-2\left[\frac{x^2}{w_x(z)^2} + \frac{y^2}{w_y(z)^2}\right]\right) \tag{2.8}$$

and equations similar to those above can be used for describing the evolution of beam radius along both directions.
The Gaussian beam is an idealization that is quite difficult to achieve, even in well-designed laser systems. Typically, the output beam from real lasers is not truly Gaussian (although the output of a single mode fiber is a very close approximation). To this purpose, the quantity M^2-factor is useful to describe the deviation of the laser beam from an ideal Gaussian beam.
The M^2-factor is defined as the ratio between the product of beam waist and divergence for the measured value ($i = m$) and the same expected for a Gaussian beam ($i = o$):

$$M^2 = \frac{\omega_m * \theta_m}{\omega_o * \theta_o} = \frac{\omega_m * \theta_m}{\lambda/\pi} \tag{2.9}$$

For an ideal Gaussian beam, $M^2 = 1$ while for a real laser beam, $M^2 > 1$. In this way, M^2 is actually a measure of the quality of an optical beam given as its deviation from the Gaussian profile.
Within this definition, the equations 2.2 and 2.4 for the Gaussian parameters of a realistic beam are corrected with M^2 in the following way:

$$w(z) = w_{0R}\sqrt{1 + \left(\frac{z\lambda M^2}{\pi w_{0R}}\right)^2} \tag{2.10}$$

$$R(z) = z\left(1 + \left(\frac{\pi w_{OR}^2}{z\lambda M^2}\right)^2\right) \tag{2.11}$$

2.2 Theory of optical cavity modes

An optical cavity is composed of at least two mirrors placed to force an injected radiation in a closed optical path. The length of the cavity determines the allowed frequencies of the circulating wave, called *resonant frequencies*.
In addition, when a beam impinges on a cavity, a good coupling condition has to be ensured by taking into account the matching of the curvature radius of the wavefront (R) with the curvature radius of the cavity mirrors. This is the so-called *mode-matching condition*: the beam waist impinging on the input coupler must be equal to the calculated waist of the cavity mode.
In a spherical-mirror resonator a Gaussian beam is a solution of the Maxwell equation. In this case, the wavefronts propagate along the optical axis and are reflected by spherical-mirrors. In this way, in order to satisfy the resonance condition, the beam has to retrace itself: as a consequence, the round-trip phase change ($\Delta\psi_{tot}$) has to be zero or a multiple of $\pm 2\pi$. This implies that:

$$\Delta\psi_{tot} = 2kd - 2\Delta\psi(d) = 2\pi q \qquad where \qquad q = 0, \pm 1, \pm 2, ... \tag{2.12}$$

where d is the cavity length. Assuming $k = 2\pi\nu/c$ and $\nu_F = c/2d$, the frequencies (ν_q) that satisfy the previous condition are:

$$\nu_q = q\nu_F + \frac{\Delta\psi(d)}{\pi}\nu_F \tag{2.13}$$

Clearly this equation shown that the frequency spacing of adjacent modes is $\nu_F = c/2d$, as obtained for the planar-mirror resonator. The term $\frac{\Delta\psi(d)}{\pi}\nu_F$ does not depend on the mirror curvatures and simply represents the displacement of all the resonant frequencies.
The condition for resonant frequencies (eq. 2.13) needs to be changed if the Gaussian beam has a transverse phase profile. This can be described by means of a polynomial expression of at least second order and the transverse profiles are called Transverse Electro-Magnetic Modes (TEMs). These modes describe the energy distribution in the beam cross section. Each transverse mode is marked as: TEM_{mn}, where m and n are integer numbers. Assuming a propagation of the along the z direction, m represents the number of points of zero illumination (between illuminated regions) along the x axis, while n the number of points of zero illumination (between illuminated regions) along the y axis.
The lowest order (TEM_{00}) is a Gaussian mode. This kind of mode, characterized by a high spatial coherence, can be focused to the smallest spot.
However, the Gaussian beam is not the only beam-like solution of the paraxial Helmholtz equation: other solutions are provided by the Hermite-Gaussian beams. As a consequence, the design of a resonator that "matches" a given beam (or the design of a beam that "fits" a given resonator) is the same as for the Gaussian beam, whatever the values of (m, n). In this way, all the members of the family of Hermite-Gaussian beams represent modes of the spherical-mirror resonator.
Looking at the resonance frequencies of the (m, n) mode, these depend on

the indexes (m, n) because of the dependence of the Gouy phase shift on the same m and n. Also in this case, the phase shift has to retrieve the same value after a round trip in a resonator of length d. As for the simple Gaussian mode, the phase shift must be zero or an integer multiple of $\pm 2\pi$, yielding the resonance frequencies:

$$\nu_q = q\nu_F + (m + n + 1)\frac{\Delta\psi(d)}{\pi}\nu_F \tag{2.14}$$

When modes with different q, but with the same (m, n), have the same intensity distribution, the modes are called longitudinal or axial modes. Differently, the indexes (m, n) label different spatial dependences on the transverse coordinates (x, y) and therefore represent different transverse modes.
For a given transverse mode, the resonance frequencies of longitudinal modes are spaced by $\nu_F = c/2d$ since $\nu_{m,n,q+1} - \nu_{m,n,q} = \nu_F$.
In addition, all transverse modes for which the sum of the indexes $m+n$ is the same have the same resonance frequencies. If one consider two transverse modes, (m, n) and (m', n'), corresponding to the same longitudinal mode q, the resonance frequencies are spaced by:

$$\nu_{m,n,q} - \nu_{m',n',q} = ((m + n) - (m' + n'))\nu_F\frac{\Delta\psi(d)}{\pi} \tag{2.15}$$

that determines the frequency shift between the sets of longitudinal modes of indexes (m, n) and (m', n').
Nevertheless, the presence of losses in a resonator relax the strict resonance condition on the frequencies of optical waves that are permitted to exist inside a resonator. Moreover, when a beam satisfies the mode-matching condition, the light is confined in the cavity and reflected multiple times producing standing waves. It can be demonstrated [47] that the finesse ($\mathcal{F}$) is the parameter that measures the capability of a cavity to enhance the radiation trapped inside and is strictly connected to the losses. This quantity is defined as:

$$\mathcal{F} = \frac{FSR}{\delta\nu} \tag{2.16}$$

where FSR is the free spectral range (the spacing between two resonances) and $\delta\nu$ is the full width at half maximum (FWHM) of each resonance peak. A second parameter related to the finesse $\mathcal{F}$ is the Q-factor, that describes the cavity performance. This one represents the ratio of the energy stored in the oscillating resonator to the energy dissipated per cycle. For an optical cavity, the Q-factor is defined by the relation:

$$Q = \frac{\nu}{\delta\nu} = \frac{\nu}{FSR}\mathcal{F} \tag{2.17}$$

2.2.1 Design of THz cavities

Resonant cavities represent important spectroscopic tools for their capability to confine and enhance light inside a cell. For example, if a molecular gas is contained in a resonant cavity, spectroscopic phenomena are amplified. The

enhancement capability depends on the finesse: a high finesse is the key aspect to develop the most advanced cavity enhanced techniques, such as the cavity-ring-down spectroscopy [48], [49], [50], [51].
Moreover, the high finesse and the consequent narrow width of the resonant peak is useful to provide a narrow reference for a laser, allowing a reduction of its emission linewidth [31].
At THz frequencies, design and fabrication of cavities is challenging, due to the technological gap of THz materials and optical components with respect to other spectral regions. More specifically, highly reflective dielectric coatings are scarcely developed at THz frequencies, and up to now only metallic coatings can be used, with maximum reflectivity limited to 99.6% for gold. In addition, metallic mirrors are not suitable as input/output couplers, and the solutions commonly adopted at microwave frequencies (hole output coupling) have proven to be quite unsuitable for THz [52].
An alternative approach consists in using a wire grid polarizer (WGP) as input/output coupler: if the electric field component is parallel to the metal wires, electrons are free to flow along them, and the incoming field experiences an almost complete reflection. However, a small amount of radiation leaks through the grid, allowing for the coupling of light in and out of the cavity. This approach has been adopted in a few early experiments in FIR spectroscopy, where finesses of about 14 and 3 [53], [54] were achieved at 690 GHz and 1.5 THz frequencies, respectively (corresponding to Q factors of about 7000 and 1500, in the two cases).
More recently, Braakman et al. [55] demonstrated that, in the sub-THz range (around 300 GHz), resonant cavities based on WGPs can achieve Q-factors as large as 10^5, sufficient for a relevant enhancement.
In this work, the first two cavities (V and ring) for THz light and injected with a QCL are proposed and experimentally demonstrated [56]. Despite the low finesse, these results constitute a first step towards the realization of a more efficient tool by planning a new geometrical configuration that minimizes losses and overcome limitations. Indeed, taking into account the key aspects of the two cavities, a new configuration is proposed and tested, and a higher finesse is reached.

Cavity parameters

In this section, the main parameters describing an optical cavity are briefly discussed.
For the sake of clarity, a linear optical cavity, composed of two mirrors, is taken into account. Each optical element is characterized by its reflectance, transmittance and absorption/scattering losses, indicated as R, T and A respectively (with $R + T + A = 1$). Furthermore, the input and output mirrors have losses (l) per round trip (due to absorption from air, additional mirrors, etc.) that affects the coupling efficiency and the power enhancement factor.
When the light is injected inside the cavity, the circulating fraction power after one round trip is written as:

$$\rho = R_1 R_2 (1 - l) \tag{2.18}$$

where R_i (with $i = 1, 2$) is the reflectivity of the two mirrors that form the cavity. Using eq.2.16, the finesse takes the form:

$$\mathcal{F} = \frac{\pi}{2arcsin\left(\frac{1-\sqrt{\rho}}{2\sqrt[4]{\rho}}\right)} \approx \frac{2\pi}{1-\rho} \tag{2.19}$$

where the approximation only holds for $1 - \rho \ll 1$. Similarly, the Q-factor, referring to eq. 2.17, can be expressed as:

$$Q = \frac{L}{\lambda}\mathcal{F} \tag{2.20}$$

where L is the round-trip length.
From the previous equations, it is clear that the finesse is strictly defined by the reflectivity of the mirrors that form the cavity and by the losses for round trip. Nevertheless, this description concerns a simple linear cavity composed of two mirrors which are respectively the input and the output coupler. If the cavity under analysis is composed of more than two elements, the previous description becomes more elaborated. Indeed, the contribution to the losses can be a complicated function.
To this purpose, it is worth to discuss about the possible loss mechanisms that governs the reflection of beam from an off-axis metal mirror. It can be demonstrated [57] that the reflected beam can lose power through resistive absorption on the metal surface:

$$L_c = \frac{4}{\cos\theta_i}\left(\frac{R_s}{Z_0}\right). \tag{2.21}$$

but also, because off-axis reflection the reflected beam alters both the shape:

$$L_{bd} = \frac{w_m^2 \tan\theta_i}{8 f_{mR}^2} \tag{2.22}$$

and the polarization of the beam:

$$L_{cp} = \frac{w_m^2 \tan\theta_i}{4 f_{mR}^2}. \tag{2.23}$$

Thus, the total mirror loss is expressed as the sum of these contributions:

$$A_{mR} = L_c + L_{bd} + L_{cp} = \frac{4}{\cos\theta_i}\left(\frac{R_s}{Z_0}\right) + \frac{\lambda}{2\pi f_{mR}}\left(\frac{\tan\theta_i}{2} + \tan^2\theta_i\right) \tag{2.24}$$

Taking into account the case under analysis in this thesis, the input/output coupler is a wire grid polarizer. In this case, the absorption losses due to the metal resistivity and the transmittance are expected to have the same value, given by:

$$A_{wg} = T_{wg} = 4\sqrt{\frac{2\rho g}{\pi\mu_0 c\lambda d}} \tag{2.25}$$

where g, d, ρ are the wires spacing, diameter and resistivity, respectively. For example, considering the values specified by the manufacturers of the WGP used in this thesis ($g = 20\ \mu m$, $d = 10\ \mu m$, $\rho = 52.8\ n\Omega$, $\lambda = 117.4\ \mu m$), the absorption losses and trasmittance are $A_p = T_p = 0.49\%$.
In conclusion, the theoretical finesse can be easily calculated according to the elements that compose the cavity, as will be shown in the following paragraphs.
However, in THz range an additional loss has to be taken into account. This is the absorption coefficient from air, related to THz transitions in ambient water vapour which have been experimentally measured to be at about 0.0038 cm^{-1} [58]. As will be described in the following, in order to reduce these additional losses, the cavities are enclosed in boxes purged with nitrogen gas.

2.3 Experimental realization: V-shaped and ring-shaped cavities

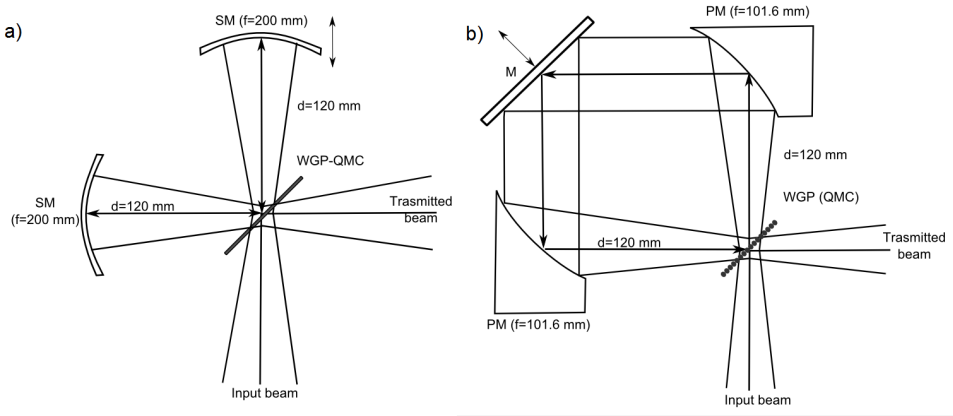

FIGURE 2.1: The two cavity configurations adopted in the present work. (a) The V-shaped cavity consists of two Au-coated spherical mirrors (SM) and one wire-grid polarizer (WGP) acting as planar input/output coupler. (b) The ring-shaped cavity consists of two parabolic mirrors (PM), one plane mirror (M), and one WPG, placed at the vertices of a square. The two-sided arrows indicate the translating mirrors. The chosen lengths ensure, in both cases, an operation close to the confocal condition, while avoiding the degeneracy of transverse modes with longitudinal ones.

The sketch of the first two cavities, with V-shaped (on the left) and ring-shaped (on the right) configurations, is shown in Fig.2.1.
The V-shaped cavity is composed of a WGP and two gold coated spherical mirrors with the same effective focal length $f_{mV} = 200$ mm, protected by a 150 nm thick SiO_2 layer. Its round-trip length is $l_V = 480$ mm.
The reflectance of these mirrors has been measured at $\lambda = 117.4\mu$m and the

obtained value was $R_{mV} = (97.0 \pm 0.3)\%$. Other measurements aimed at estimating R_p, T_p and A_p for the WGP have been performed. The resulting values are (R_p,T_p,A_p) $\approx$ (99.2%,0.4%,0.4%), which are very similar to the one theoretically retrieved in the previous section.
Using these values and in absence of absorption from air, the finesse for this cavity geometry can be estimated as:

$$\mathcal{F}_V \approx \frac{\pi}{1 - R_p R_{mV}} \approx 83 \tag{2.26}$$

However, due to its geometrical configuration, the V-shaped cavity (when in resonance condition) will generate optical feedback on the source.
For this reason, the ring-shaped configuration, shown on the right of the same figure, has been designed in order to obtain a cavity without optical feedback (OF). Indeed, the beam travels on a square optical path, with round-trip length $l_R = 480$ mm defined by the polarizer, a plane mirror and two off-axis parabolic mirrors with the same effective focal length $f_{mR} = 101.6$ mm. As required, the light travels only in one direction and no OF is expected on the laser.
The mirrors used in the ring-cavity are the same as those used for the V-shaped cavity. The mirrors are protected by a 150-nm-thick SiO_2 layer, and therefore their reflectance is $R_{mR} = (97.0 \pm 0.3)\%$. In absence of absorption from air, the finesse for this cavity geometry is expressed as:

$$\mathcal{F}_R \approx \frac{\pi}{1 - \sqrt{R_p R_{mR}^3}} \approx 65 \tag{2.27}$$

A summary of the main parameters of the two cavities is reported in the following table (2.1).

TABLE 2.1: Main parameters calculated for V-shaped and ring cavities. All parameters are calculated in vacuum (without absorption from air). The column $\mathcal{F}_{air}$ reports the finesse values calculated by taking into account a water vapour absorption coefficient of 0.0038 cm^{-1}.

Cavity	l (mm)	FSR (MHz)	$\mathcal{F}_{air}$	$\mathcal{F}$	$\delta\nu$ (MHz)	Q	Enhancement
V-shaped	480	625	24	83	7.5	3.4×10^5	2.8
Ring	480	625	22	65	9.6	2.7×10^5	1.7

However, these two cavity configurations represent a first step to open the way to the improvement of cavities in THz range. Their experimental realization is illustrated in the following sections.

2.3.1 Experimental test of the cavities

The experimental setup used to test both the cavities is shown in Fig. 2.2.
The QCL used in this work, fabricated in the CNR-NEST laboratories, is based on a bound-to-continuum design. The emission frequency is close to 2.55 THz, and the QCL is mounted on the cold finger of a liquid helium cryostat. It is driven in continuous-wave mode at a fixed heat sink temperature

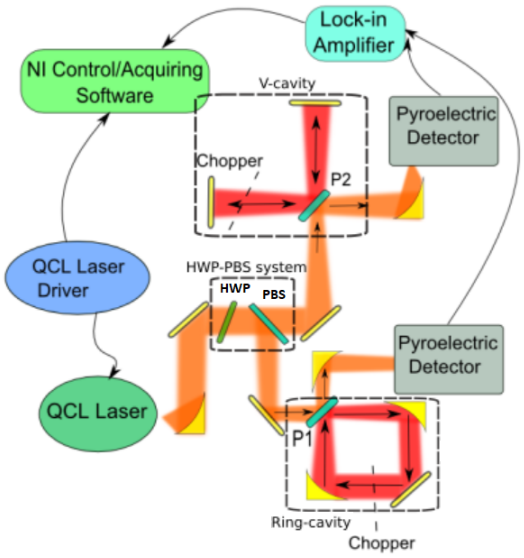

FIGURE 2.2: The experimental setup includes both the developed cavities. The half-wave plate (HWP) and the polarizing beam-splitter (PBS) allow to choose the fraction of the QCL light to be sent to each cavity. In this way it is possible to use one cavity at time or both simultaneously. The mirrors placed after the PBS allow for an independent alignment of each cavity.

T $\approx$ 20.0 K. Under these experimental conditions the QCL threshold current is I_{th} =340 mA, and the operating current is around 380 mA, supplied by a home-made low noise current driver (< 1 nA/Hz$^{1/2}$).
The output window of the cryostat for the QCL radiation is tilted with respect to the optical axis in order to avoid standing waves and to minimize etalon effects in the measurement and back reflections into the laser.
The emitted beam is divergent and an off-axis parabolic gold coated mirror (with an effective focal length of 25.4 mm) is used to collect and collimate the beam. A couple of planar mirrors are used to guide the beam through a half waveplate (HWP, realized at the CNR-INO optics workshop from a quartz substrate) and a polarizing beamsplitter (PBS, QMC Instruments, mod. P10). The latter is a photolithographic polarizer, placed at 45^o angle of incidence and its wires are vertically oriented according to the QCL polarization. Indeed, it is considered that the native QCL polarization is linear and orthogonal to the epitaxial growth axis. Therefore, the emitted polarization is in the vertical plane with respect to the optical breadboard.
The HWP-PBS system is used to divide the beam power into two parts, for the two cavities. In particular, the HWP allows to rotate the linear QCL polarization of the desired amount, while the PBS splits the beam in two parts, with horizontal and vertical polarizations, and complementary powers.
The distance between the input couplers of both the cavities and the QCL is about 500 mm. The orientation of the wires of the two WGPs are chosen parallel to the polarization of the incoming beams. More specifically, the wire orientation is horizontal for the V-shaped cavity and vertical for the ring-shaped cavity.
In both the cavities one of the mirrors is mounted on a motorized translation

stage (ThorLabs, mod. MTS25) controlled by a LabVIEW program. The QCL wavelength is fixed by keeping both the heat sink temperature and the driving current constant, while the resonance frequency of both cavities is tuned by changing their lengths.
The LabVIEW program allows to select the scanning speed (typical value 1.5 $\mu m/s$), the total scan length (typically 200 μm), the total scan time and the acquisition rate.
The detection is performed using an optical chopper on the beam and a lock-in acquisition. The signal is acquired with a pyroelectric detector (Gentec EO, mod.SPH 62 THZ) which is aligned on the beam reflected by the input coupler. If the chopper is placed outside the cavity, the detected power P_r is equal to the total incoming power P_0 when off resonance, whereas a power dip is expected in resonance condition, since a fraction of the incoming light is coupled to the cavity.
In order to make a zero-offset acquisition, the beam chopper (driven at 172 Hz) is placed inside the cavities, and the lock-in detection is implemented. In fact, by placing the chopper wheel inside the cavities it is possible to detect the amount of coupled radiation as a peak occurring at resonance.

2.3.2 Coupling to cavities

A beam emitted by a continuum wave QCL is an elliptic mode, with very large M_x^2 and M_y^2 values. For this reason, the first step for the correct characterization of a cavity is the achievement of a mode-matching in both x and y directions.
In order to satisfy this condition, the parabolic mirror, that collects the emitted beam, is not placed at the perfect collimation distance but it is moved slightly away. In this way, the beam is focused avoiding the use of lenses that absorb high fractions of the beam power. To this purpose, an iterative procedure is implemented in order to place the parabolic mirror in the best position to obtain the required beam waist.
The procedure consists in the acquisition of the beam sections at different propagating distances along the optical path. A LabVIEW program, connected with a THz camera (INO IRXCAM), is used to acquire the image of the beam section. A Matlab program is used to extract the beam waist value in both x and y directions by fitting the profile in the two directions with a Gaussian function (eq.2.8). In this way, for each position of the parabolic mirror, the beam waist is measured. If it is far from the theoretical value, the parabolic mirror is moved and the beam waist is measured again until it reaches the required value.

The acquisition of the beam section and the measurement of the beam waist are shown in Fig.2.3. These data are taken at the condition in which the beam waist is quite similar to the theoretical value in both the two directions. In the graph, the minimum value (z_o) of the parabola corresponds to the position in which the beam waist is achieved. In this way, the input coupler can be correctly located at a distance of z_o from the source.

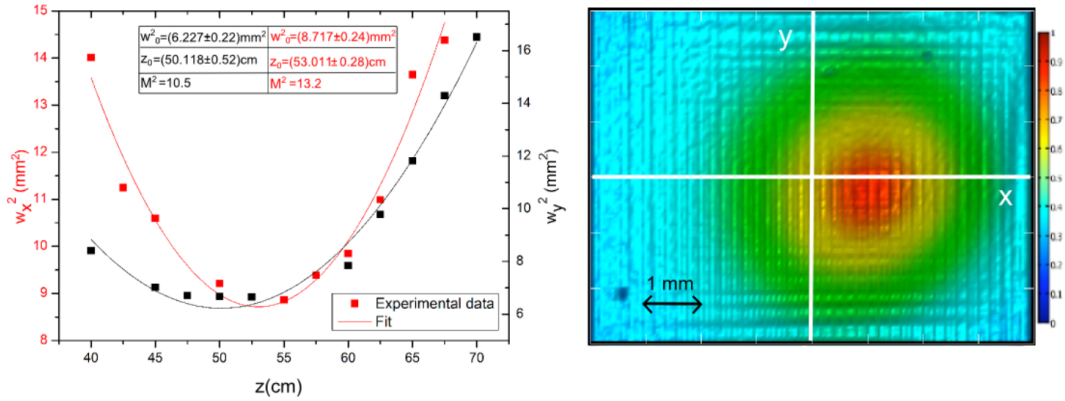

FIGURE 2.3: On the left picture: The measurement of the beam waist dimensions and position is carried out by taking several images of the beam section (on the right picture, example) at different propagation distances, and by fitting them with Eq.2.2. The laser collimation is adjusted in order to optimize the mode matching with the cavities modes.

Furthermore, the fit gives the M^2-factor in both the directions. However, the values of $M_x^2 = 13.2$ and $M_y^2 = 10.5$ are far from unity, confirming that the beam is not Gaussian. Therefore, in the cavity characterization, the high deviation from the Gaussian beam is expected to significantly affect the laser coupling to the cavities.
After retrieving the fundamental condition (mode matching), the acquisitions of the spectrum can be performed. The cavities can be singularly injected, and their resonance signals can be maximized by fine adjustments in the alignment. During the fine optimization, an oscilloscope allows to check the spectrum obtained by scanning the cavity length.

2.3.3 V-cavity characterization

At first, the V-cavity is singularly injected, and its spectrum is analysed.

The optimized resonance spectrum is reported in Fig.2.4 where the scan of the cavity length is set in order to acquire two or more resonance peaks.
In the first acquisition (black line) the cavity was in air. In this case, the measured finesse value of 16 is far away from the theoretical one. As already said, this can be explained by the absorption from the water vapour contained in the air filling the cavity. This is confirmed by the good agreement with the cavity finesse value calculated in presence of absorption from air and presented in Table 2.1.
In order to overcome this limitation, the cavity has been placed in a close box, purged with nitrogen gas.
As expected the nitrogen atmosphere strongly suppresses water vapour inside the cavity, reducing the absorption. The resulting cavity spectrum is shown as a red plot in Fig. 2.4. Under N_2 purging, the finesse raises by a factor two, up to a value of 25, leading to an increase of the intensity of the modes by a factor of three.

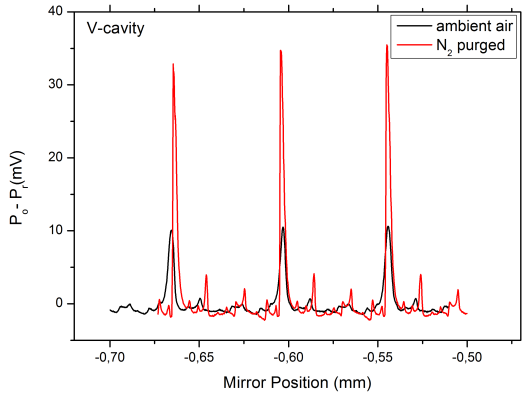

FIGURE 2.4: Effect of the absorption from air on the V-shaped cavity spectrum, as evidenced by comparing two spectra acquired with the cavity either in ambient air (black) or under N_2 purging (red). In this latter case, the lower losses determine narrower and higher resonance peaks, due to the expected increase of the cavity finesse.

This value is far from the theoretical one. This apparent difference of the finesse with respect to the expected value, is due to optical feedback as just expected for the cavity geometry. According to the V-shaped geometrical configuration, when this cavity is resonant a small fraction of the incoming radiation leaks back towards the laser. The back radiation on QCL perturbs the laser emission and, in particular, the laser frequency, that is expected to follow the cavity resonance within a given range.
Clearly this phenomenon is shown in Fig.2.5, as it can be studied by varying the amount of radiation feeding back to the laser. This is achieved by means of the HWP-PBS system (see Fig.2.2) simply rotating the HWP, i.e. controlling the power of the beam injected in the V-shaped cavity. In Fig.2.5 (a) the comparison among several acquisitions of the cavity resonance peak, taken at different feedback levels, is reported. It is clear that the higher the beam power is, the larger the peak resonance becomes, and the apparent cavity finesse will change accordingly, as shown in Fig.2.5 (b). Clearly the plot shows that the presence of OF results in a lower measured finesse value, suggesting that the QCL frequency is perturbed by OF and follows the cavity mode frequency. Therefore, a realistic measurement of the V-shaped cavity finesse can be performed only at very low beam intensity.

Finally, the typical spectrum obtained by the V-shaped cavity (at low laser power) is reported in Fig.2.6. The presence of a transverse mode reveals that the mode matching between the laser beam and the longitudinal cavity mode is not perfect.
The achieved finesse is $\mathcal{F}_V = 58$ and corresponds to $Q = 2.4x10^5$. This value is significantly lower than the expected one (83) as even a small amount of OF to the laser will strongly affect the experimentally measured finesse (see Fig. 2.5).

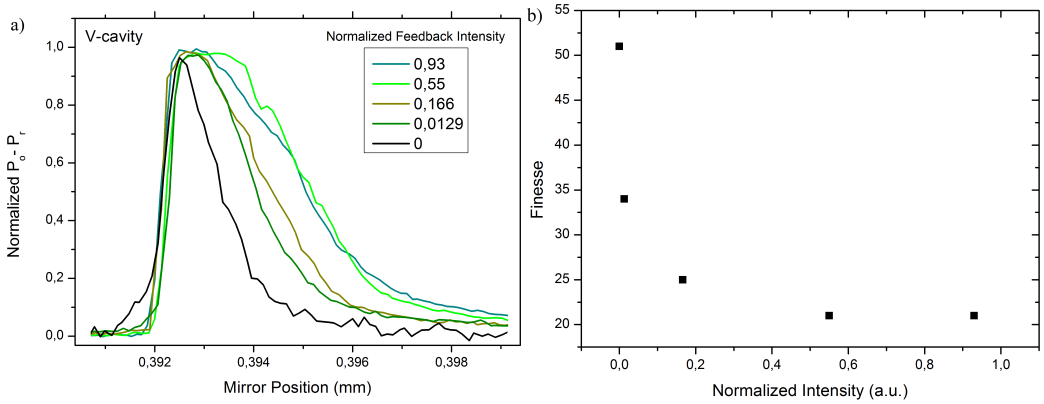

FIGURE 2.5: The effect of OF from the V-shaped cavity to the QCL is quantitatively studied by analysing the width of the cavity peak as a function of the incoming power (a), and thus of the feedback level (normalized to its maximum value). From the peak width it is possible to retrieve the dependence of the apparent cavity finesse on the feedback level (b).

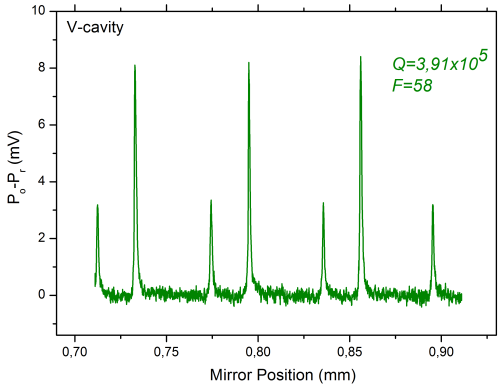

FIGURE 2.6: Optimized spectrum of the V-shaped cavity in N_2 purged atmosphere. The suppression of OF is obtained by attenuating the incoming beam and, consequently, the back-reflected beam.

2.3.4 Ring cavity characterization

As for the V-cavity, the first spectrum has been acquired in ambient air and compared to the same in nitrogen purged air to confirm that the absorption by water vapour degrades the finesse.

The typical ring cavity spectrum acquired in nitrogen purged atmosphere is shown in Fig.2.7.

The ring configuration should ensure the absence of OF as verified with the same analysis done for the V-cavity (Fig.2.5). In fact, no changes can be noted while measuring the finesse at different laser powers, thus confirming that the ring-shape configuration is free from OF. For this reason, the optimization can be carried out at the maximum available power. This explains the high signal-to-noise ratio of the acquired trace. The achieved finesse is $\mathcal{F}_R = 63$, corresponding to $Q = 2.6x10^5$.

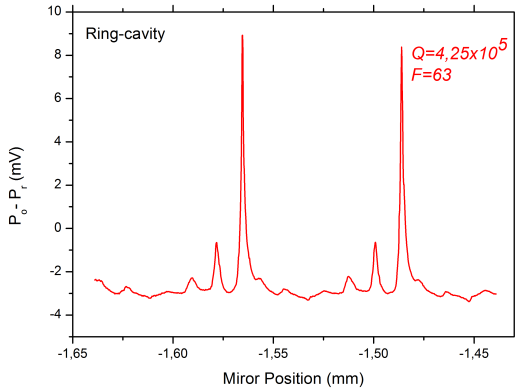

FIGURE 2.7: Optimized spectrum of the ring cavity in N_2 purged atmosphere.

For the ring cavity, the achieved finesse reaches the theoretical value calculated in the previous section and shown in table 2.1. The more complex cavity geometry and mirror shape result in a larger number of transverse modes, that are partially populated due to the non-perfect mode-matching between the laser beam and the longitudinal cavity mode.

2.3.5 Optical feedback from V cavity

The characterization of the two cavities has led to the possibility to inject them at the same time and to take advantage of their properties. The OF that affects the V-cavity can be a disadvantage if one is interested in the performance of the cavity, which results degraded. Otherwise, the OF can be an advantage if one think to the possibility of optically locking the QCL frequency to the V-shaped cavity resonance.
As demonstrated in Fig.2.5, the laser frequency follows the resonance as an optical locking. The effect of V-shaped cavity OF on the QCL can be studied by using the ring cavity as a monitor of the laser frequency fluctuations. The ring cavity is tuned at resonance half-height, so that the peak slope converts any frequency drift in a detectable amplitude variation. The V-shaped cavity is then scanned, and the signals from both cavities are simultaneously acquired. At this regard, the spectrum of the ring cavity is expected to be a flat signal if the laser power is not affected by perturbations: in this way, the cavity is used to check changes in laser power. This effect is demonstrated by injecting both resonators at the same time.

The V-shaped cavity is swept across its resonances, while the ring cavity is kept fixed at a resonance half-height. In these conditions any shift on the laser frequency will result in a variation of the signal retrieved from the ring cavity.
Two V-shaped cavity scans (black lines), and the ring-cavity signals (red lines), are shown in two opposite situations in Fig.2.8:

- with strong OF to the QCL laser ($\simeq 1\%$ of the V-shaped cavity incoming radiation) Fig.2.8 (a);

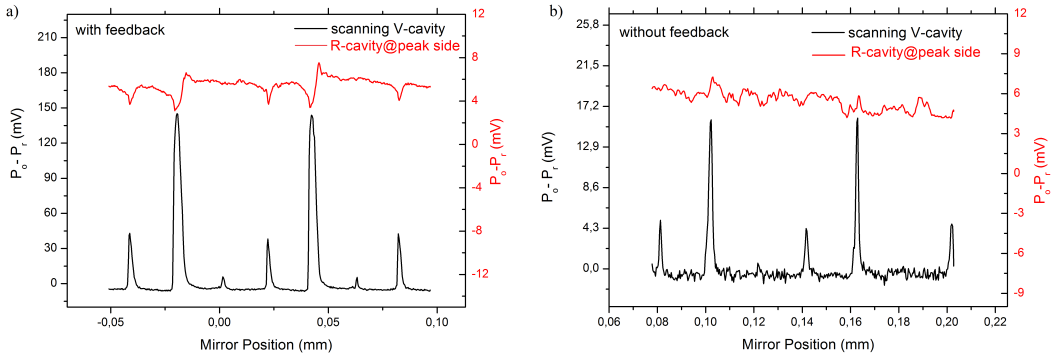

FIGURE 2.8: The measurement is performed in presence (a) and in absence (b) of OF to the QCL. Slow changes in the red signal are due to QCL laser temperature drifts, amplified by the signal slope

- with almost no OF to the laser, i.e. obtained by strongly attenuating the beam that feeds the V-shaped cavity ($\simeq 0.001\%$ of the V-shaped cavity incoming radiation) Fig.2.8 (b).

The signal of the ring cavity (red, a) explains the reason of the apparent V-shaped cavity finesse degradation and peaks widening in presence of OF (black, a). In OF condition, as the V-shaped cavity gets closer to the resonance with the QCL, the QCL frequency is first pulled towards the cavity resonance, and then sticks to it for a while, until it is released again and restores to its original value.
On the contrary, when the OF from the V-shaped cavity is suppressed, no effect on the QCL frequency is detected by the ring cavity signal (red, b) and the V-shaped cavity spectrum shows a higher finesse and sharper peaks (black, b).
When present, the frequency pulling effect is still quite small, in the range of 1 MHz or less, and this is probably due to two different reasons. First, the OF level to the QCL, in these experimental conditions, is estimated to be around 1%, and even less if a small misalignment of the optical paths is taken into account; this feedback level may not be enough to ensure a large optical locking bandwidth. Second, no control of the phase of the OF is implemented at present, and this can explain a non-optimized efficiency of the optical locking mechanism. Nevertheless, the presented results are a straightforward evidence that an external high-Q THz cavity can have an influence on the frequency of a QCL.

2.4 Bow tie cavity

An optical cavity with a ring path is a design that minimizes the OF avoiding back reflection on the source. On the other hand, a ring-cavity requires off-axis mirrors, that can introduce distortions in the beam shape and in the polarization of the electric field involving additional losses. A compromise between small incident angles and a ring path is given by a bow-tie configuration.

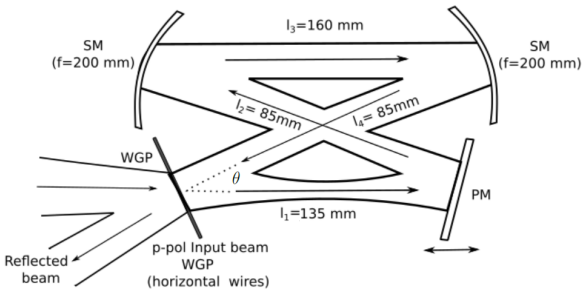

FIGURE 2.9: Configuration of the bow-tie cavity that consists in a planar and in two gold spherical mirrors (SM), a wire grid polarizer (WGP) as input/output coupler. The two-sided arrow indicates the translating mirror.

The bow-tie cavity (BTC), as its name suggests, is designed such as the light performs a crossed circular path, as shown in Fig.2.9. The light is injected by the wire grid polarizer, tilted at a small angle with respect to the direction of the beam propagation. A planar mirror (PM) is placed to reflect the beam, at an angle of θ, towards a couple of identical spherical mirrors (SM), with the same effective focal length and placed to close the path of the beam on the WGP.
The round-trip path-length is 493 mm, while the two concave golden spherical mirrors have an effective focal length of $f_{mV} = 200$ mm. The spherical mirrors have a gold coating made by chemical deposition (electroplating), with a thickness of about 500nm and without a protective dielectric layer. The planar mirror has the same coating of the spherical ones. However, the small incidence angle minimizes the effect of elliptical eigenmodes and preserves the reflectivity of the mirrors, which were manufactured for normal reflection.
The WGP (QMC-Instruments, mod. QWG/RT) is composed of tungsten wires, with a diameter of 10 μm, separated by 20 μm.
This type of cavity requires a beam waist of 1.8mm in the middle of the path, labelled with l_1 (see Fig.2.9). However, its finesse is expressed as for the ring cavity (eq. 2.27) since the two cavities are both composed of four optical elements that force the light in a ring path. According to the theoretical digression of the previous section, in absence of absorption from air, the finesse is given by:

$$\mathcal{F} \approx \frac{1}{1 - \sqrt{(R_p R_{mB}^3)}} \approx 110 \tag{2.28}$$

where R_p is the reflectivity of the WGP and R_{mB} is the reflectivity of the mirrors.
This value has been compared to the one simulated by a software *Finesse*.
Finesse [59] is an interferometer simulation tool designed to model the types of interferometers used in gravitational wave detectors. The scripting language is quite simple: each line in the script describes either an optical component, a detector to output some data, or a command.

In order to simulate an optical cavity, its geometry is defined as well as the physical properties of each component. Moreover, the input beam can be simulated defining the beam waist in the two directions, of $TEM_{m,n}$, of input power and so on. *Finesse* generates a layout of the system and the simulated spectra with the relative parameters such as the finesse, the FRS and the FWHM of the resonant peak.
Concerning the BTC, the QCL real beam shape has to be taken into account in the simulations. To this purpose, the beam is described by a superposition of an ideal Gaussian beam ($TEM_{0,0}$) and transverse modes ($TEM_{m,n}$). The power of the transverse modes is a small fraction of the total one and contributes to the non-symmetrical shape with resulting in a broadening of the beam waist from 1.8mm (for $TEM_{0,0}$) to 3.5mm.

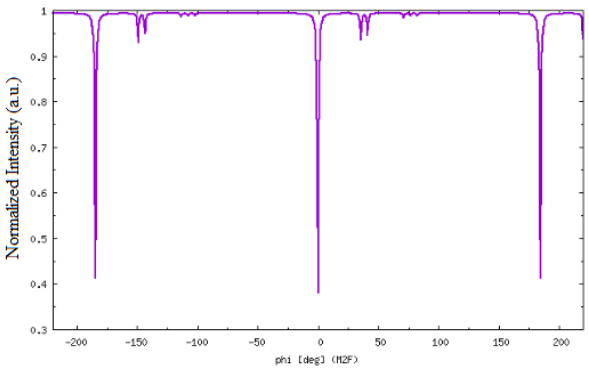

FIGURE 2.10: Simulated spectrum of the BTC in the optimal condition ($R_m = R_{WGP}$ =99.9%, T_{WGP}=0.1%). The finesse value is 110.

In the simulations, the reflectivity of mirrors (R_m) is 99.9%, while the WGP has a reflectivity of 99.9% and a transmission of 0.1%. With these hypotheses, a finesse is 110 is confirmed and the simulated spectrum is shown in Fig.2.10.

TABLE 2.2: Main parameters calculated for the bow-tie cavity. All parameters are calculated in vacuum (without absorption from air). The column $\mathcal{F}_{air}$ reports the finesse calculated by taking into account the water vapour absorption coefficient of 0.0038cm^{-1}.

Cavity	l (mm)	FSR (MHz)	$\mathcal{F}_{air}$	$\mathcal{F}$	$\delta\nu$ (MHz)	Q	Enhancement
BTC	493	608	32	110	2.9	8.1×10^6	16

The simulated output data, which are the main parameters of the cavity, are reported in table 2.2. Looking at the finesse and the enhancement factor, the performance of the BTC are evident. An enhancement factor of 16 means that the light is amplified of an order of magnitude with respect to the input value inside the cavity. In the actual-state-of-the-art, this result represents a milestone, opening the way to possible spectroscopic and metrological applications.

2.4.1 Experimental setup

In the experimental setup described in section 2.3.1, the V-cavity can be replaced by the BTC.

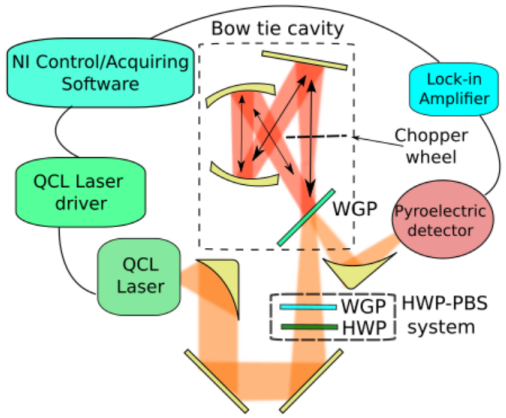

FIGURE 2.11: Experimental setup. WGP: wire grid-polarizer; HWP: half-wave plate.

A sketch of the experimental setup is shown in Fig.2.11.
The laser source is the same quantum cascade laser used for the previous cavities, emitting at 2.55 THz and mounted on the cold finger of a liquid helium cryostat.
The QCL is driven in CW mode by a low-noise current source at 370 mA with a fixed heat sink temperature $T = 25$ K at which the QCL threshold current is $I_{th} = 340$ mA.
The optical setup is adjusted for the BTC by modifying the beam waist in both parallel and orthogonal planes with respect to the propagation axis of the QCL. The divergent QCL emission is collected by an off-axis parabolic golden mirror, with an effective focal length of 25.4 mm, and guided with two planar mirrors to inject the cavity. The parabolic mirror is moved slightly away from the perfect collimation distance in order to focus the beam in the cavity and to satisfy the mode-matching conditions.
Furthermore, the cavity is enclosed in nitrogen atmosphere to purge the water vapor responsible for the absorption in air.
In order to tune the cavity length, the planar mirror of the cavity is mounted on a motorized translation stage (ThorLabs, mod. MTS25) controlled by a LabVIEW program. This program allows to select the scanning speed (typical value 1.5μ m/s), the total scan length (typically 200μm), the total scan time and the acquisition rate.

2.4.2 Lock-in acquisition

A lock-in acquisition is performed and the transmitted spectrum from the cavity is detected by a pyroelectric detector aligned on the beam reflected by the wire grid-polarizer.
In order to perform a lock-in acquisition, the signal to be acquired is modulated on its amplitude or on its frequency.

In the first case, the modulation is performed with a mechanical chopper placed inside the cavity. In this way, the signal is proportional to the light coupled in cavity and the spectra will have a zero background and positive peaks.
On the contrary, as for the V-shaped and ring-shaped cavity, by placing the chopper wheels outside the cavities it is possible to detect the amount of coupled radiation as a dip in the power of the beam reflected by the input coupler, occurring at resonance.
Moreover, instead of an intensity modulation (chopper) a frequency modulation can be performed directly acting on the driving current. The acquisition is performed by modulating the QCL current with a sinusoidal wave superimposed on the continuous wave. In this case, the spectrum will be the derivative of the typical one obtained with a chopper modulation.
To retrieve the resonant condition of a cavity, it is mandatory to scan its length or, with the same purpose, the laser wavelength, that is strictly connected to the length of the cavity itself (which is a multiple of this length). For the sake of completeness, the comparison between these two kinds of acquisitions is performed.

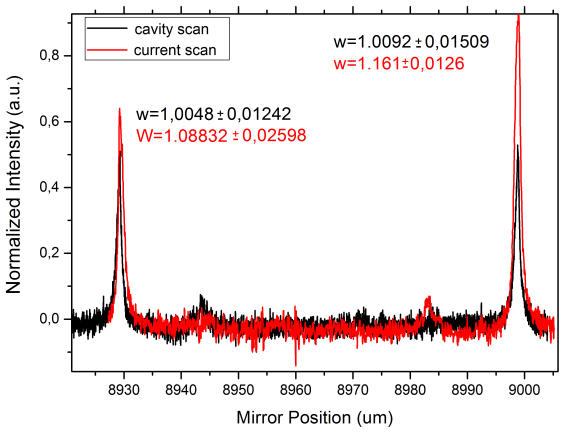

FIGURE 2.12: Comparison between two acquisitions made scanning the length of the cavity (black plot) and scanning the QCL driving current (red plot). In the latter, the x-axis is reported in micrometer to compare the two results.

The laser wavelength can be scanned through the driving current, which is strictly connected. In this condition, an acquisition of few volts covering two free spectral range can be performed and a positive ramp turns out to be equivalent to an increment of the cavity length.
The comparison, described above, is reported in Fig. 2.12. It is visible that, when the length of the cavity is scanned, the peak amplitude is the same for both the resonances and the peak width is narrower. On the contrary, for the acquisition obtained by changing the current, the peaks have different amplitudes and larger widths. The reason is that when the current is scanned both the intensity and the temperature change. As a consequence, both the laser power and the laser frequency change. In conclusion, the best spectra are obtained by scanning the cavity length.

2.4.3 Alignment, test and optimization

As done for the V-shaped and the ring cavity, the mode-matching condition is satisfied by measuring the beam waist at different distances from the cryostat. The procedure is the same explained in section 2.3.2.
Once provided the mode-matching condition, the alignment of the cavity is carefully performed. The procedure consists on the correction of the main contributors to the cavity losses and then with the elimination of each minor perturbation.
Each optical component is supported by a mirror mount with pitch and yaw adjusters, enabling very fine angular movements. In this way, a large number of possible adjustments can be performed and consequently this yields a more difficult alignment. Therefore, a theoretical comparison becomes necessary through the simulation of the experimental spectra by means of the software *Finesse*.
The advantage is that the comparison with the expected spectra allows to easily identify the degrading contribute to the finesse. Indeed, it is possible to reconstruct the effects on the cavity spectrum induced by each type of mismatch. The key aspect is that the simulated spectra can reproduce exactly the experimental one by choosing the input parameters the most realistic possible way.
In order to better explain the alignment procedure, some examples are briefly discussed.

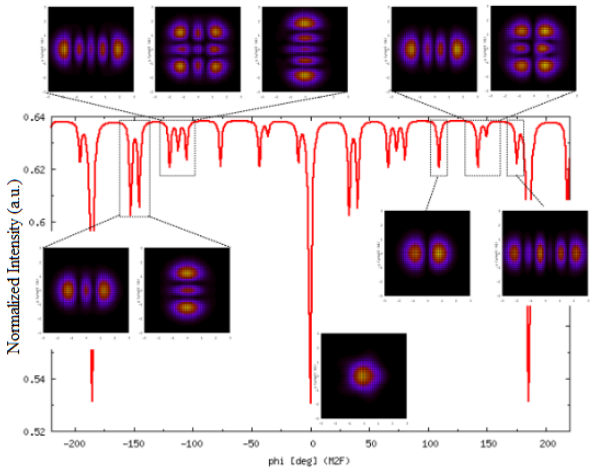

FIGURE 2.13: Simulated spectra for a beam whose beam waist is the theoretical one ($\omega_o = 3mm$). The beam is composed of $TEM_{0,0}$ and $TEM_{0,1}$, $TEM_{1,0}$.

The first check concerns the beam waist as required by the mode-matching condition. As an example, the beam can be simulated as composed of $TEM_{0,0}$, which is the main contribution, and of $TEM_{0,1}$ and $TEM_{1,0}$, which contribute least to the spectrum. In addition, the beam waist is taken far from the theoretical one.
The simulated spectrum and the beam profiles of the transverse modes are shown in Fig.2.13. This analysis is useful to recognize a spectrum obtained

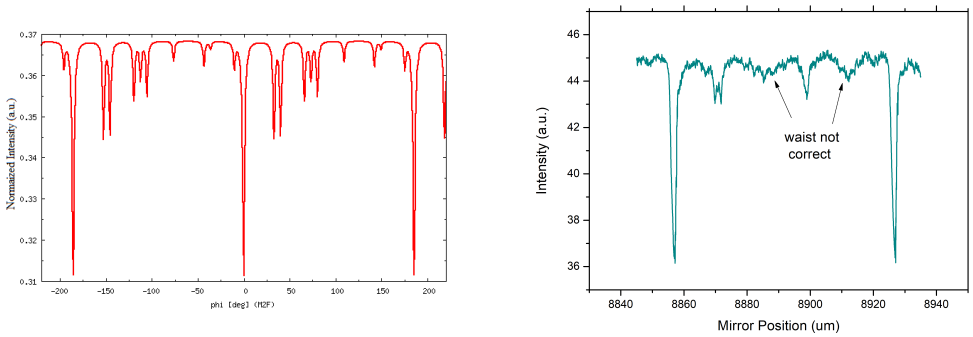

FIGURE 2.14: On the right: simulated spectra for a beam with a not-correct beam waist ($\omega_o = 3$ mm). The transmission and reflectivity are the same as for the previous simulation. On the left: experimental spectrum.

when the beam waist is far from the theoretical one looking at the transverse modes.

The early experimental spectrum (on the left) and the corresponding simulated one (on the right), shown in figure 2.14, are compared. As it can be easily seen, there is a great resemblance by the experimental spectrum and the simulated one.

More specifically, in order to simulate the experimental spectrum, the transmission and reflectivity of each optical component are respectively 1% and 98%. As already observed with the simulation shown in Fig.2.13, the presence of the transverse modes near the longitudinal modes indicates that the experimental beam waist is different from the value required by the mode-matching condition. In order to simulate this case, the beam waist has been defined as $\omega_o = 3$ mm in the input parameters.

Being well known that for a QCL it is very difficult to obtain a pure $TEM_{0,0}$ mode, because the transverse modes are always present at some extent, the simulated beam has to be composed by $TEM_{0,0}$ and $TEM_{0,1}$ (this one, as a small contribution) in order to reproduce correctly the spectral profile.

The information extracted from the previous analysis involves the adjustment of the beam waist. The spectrum (grey plot), obtained after this optimization process, is reported in Fig. 2.15, perfectly superimposed to the simulated spectrum (red plot). As shown, the transverse modes are reduced with respect to the previous graphs. The output parameters from the simulation give a free spectral range (FSR) of 624 MHz, a FWHM of 14 MHz and a finesse of 44.

More specifically, in order to simulate this experimental spectrum, the laser beam has been simulated considering almost all the total power in $TEM_{0,0}$ and a tenth in $TEM_{0,1}$. Moreover, the reflectivity of the mirrors has been reduced to 98%. However, this value is not realistic, thus suggests that other effects are responsible for the worse performance of the cavity.

A first hypothesis concerns the degradation due to air absorption. However, the cavity is free from water content because of it is enclosed in a box purged with nitrogen. Another possibility concerns the presence of optical feedback even if the cavity has been designed with a circular path to avoid OF.

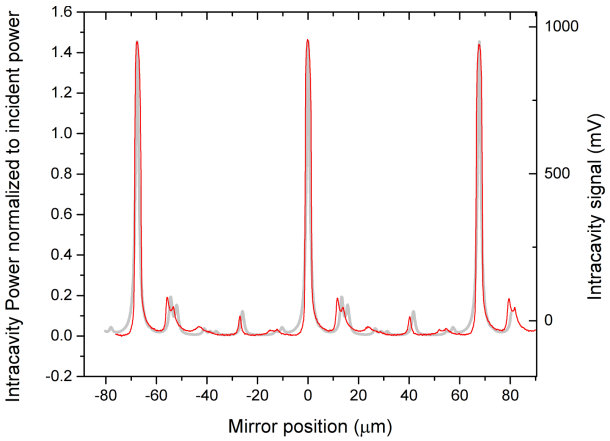

FIGURE 2.15: Comparison between an experimental spectrum (grey plot) and a simulated one (red plot). In the latter, the beam waist has not been simulated as the theoretical one ($\omega_o = 3$ mm) while the beam is composed of only $TEM_{0,0}$. The WGP transmission and reflectivity are 98% when the WGP acts as mirror, while the reflectivity is 92% when acts as beam-splitter and the transmissivity is 1%.

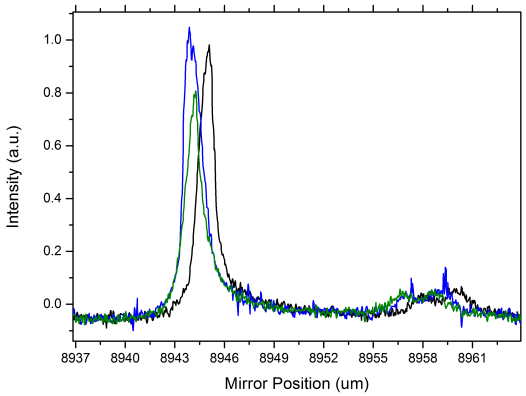

FIGURE 2.16: Transmitted spectrum obtained by scanning the cavity length and modulating the QCL current. The spectra have been acquired at different focal positions of the parabolic mirror.

To investigate about this hypothesis, it can be considered that a good evaluator of the absence of optical feedback is the symmetry of the peak shape. To this purpose, a scan around a longitudinal peak is performed in order to better observe its symmetry.
The idea is to slightly change the position of an optical element to induce a perturbation in the beam phase. This effect is observed by finely tuning the position of the focal plane of the parabolic mirror that collects the emitted beam.

As shown in Fig.2.16, the signal profile changes for two different positions, leading to a clear indication that OF effect is present and has to be investigated with major accuracy.

Therefore, the OF presence has been investigated as for the V-shaped and ring-shaped cavities. The peak width and its profile have been examined

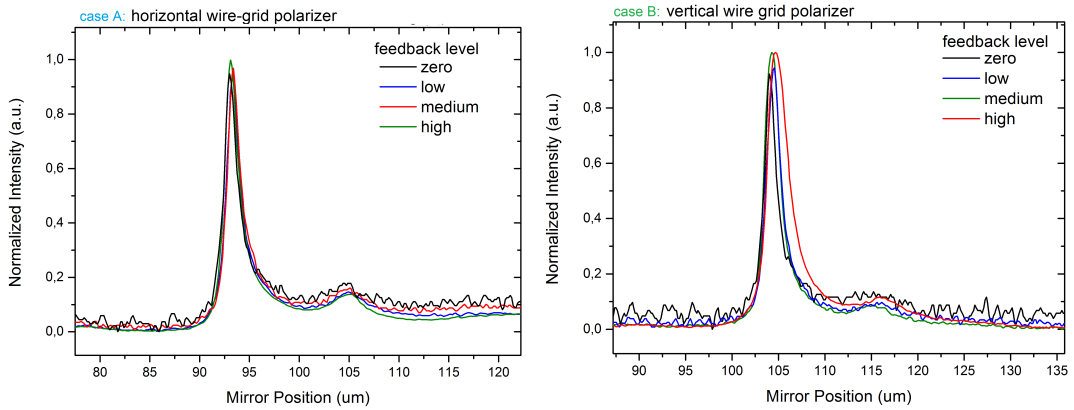

FIGURE 2.17: Analysis of the peak width for different feedback level when the wires of the WGP are horizontally oriented (on the left) or vertically oriented (on the right).

at different levels of feedback. In addition, the wires of the input/output coupler were oriented along the perpendicular direction, which is when the wires are horizontally oriented.
This measurement can be done by means of the HWP-PBS system that allows to change the polarization orientation of the injected field in the cavity. In this way, a systematic measurement of the peak width for different orientations of the beam polarization is a particularly challenging experimental task. The aim is to check a potential configuration useful to improve the cavity quality.

More specifically, the idea is that if the feedback is present, the peak resonance becomes larger, giving an apparently lower cavity finesse.
The results of this analysis are shown in Fig.2.17. The peak width taken at different feedback level is reported when the wires of the WGP are horizontally oriented (case A, on the left) or vertically oriented (case B, on the right). In the latter case, the width of the peak changes at different feedback levels, confirming that the OF is present clearly.
Differently, when the wires are horizontally oriented, the OF is absent. Nevertheless, at zero feedback level, the width of the peak is larger with respect to the case B. It seems that an additional effect is present, and its effect is maximum when the wires are horizontally oriented (0^o) and minimum in the opposite case (90^o).

For the sake of clarity, the two different orientations of the WGP are sketched in Fig.2.18. When the system is arranged to have a beam with a horizontally polarization (a), the wires and the polarization define an angle in the plane. The WGP reflects only a fraction of the total field implicating an increase of its losses. In this way, the peaks are slightly larger, as shown before.
If the wires of the WGP are vertically oriented (b), the previous effect is absent, but another effect arises: the diffraction. In order to better explain this effect, a detailed description is given in the following.
Generally, the diffraction effect is absent when the incident wavelength (λ_{in}) results smaller with respect to the wavelength linked to the distance (g) between the wires:

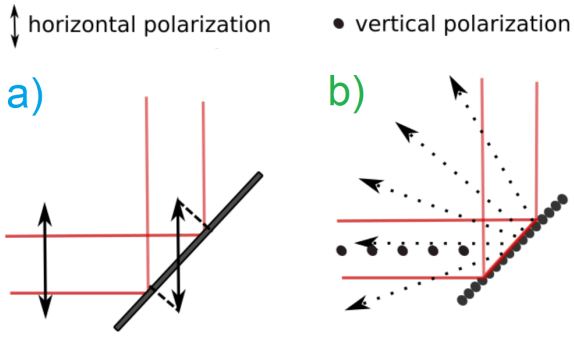

FIGURE 2.18: Wire grid polarizer in two different orientations. a) wires horizontally oriented. b) wires vertically oriented.

$$\lambda_{in} < \lambda_d = g(1 + sen(\theta)) \tag{2.29}$$

where the angle θ is taken with respect to the normal direction of the polarizer. Differently, in this case, the wires of the WGP act as a N-slits system that creates a diffraction pattern on the plane perpendicular.
The losses due to the OF-diffraction are expressed as the ratio between the wavelength diffracted from the N-slits and the wavelength (λ, k) at normal incident angle on the WGP, that is diffraction-free. These losses are defined by the relation:

$$\alpha_{OF} = \frac{\lambda_d}{\lambda_{in}} = \frac{Sin(kg/\lambda sin(\alpha))}{(kg/\lambda sin(\alpha)} \tag{2.30}$$

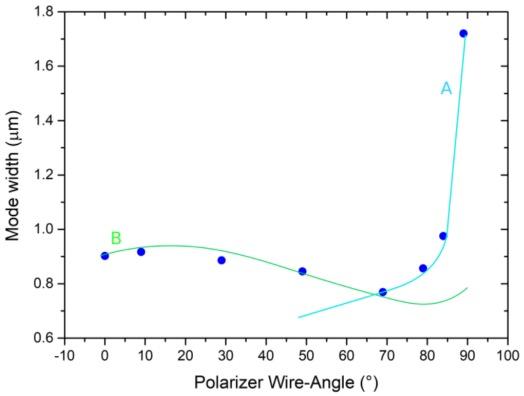

FIGURE 2.19: Systematic analysis of the peak width for different polarization orientation. The feedback is evident around 90^o with the increasing of the width.

By using the HWP-BPS system on rotation of the input-coupler, a complete systematic analysis has been performed in order to investigate the previous effects at the intermediate angles.
The results are shown in Fig.2.19. The effects due to the losses (case A) and to the diffraction (case B) are clearly visible as described before. In the graph the two effects are highlighted and it is clear that around 80^o the trade-off of the two effects is maximum.

From these results the condition at which the cavity can work in a way to enhance the finesse has been determined.

2.4.4 Best Results

The previous characterization has led to the exploration of the optimal working conditions, ensuring the best performance of the cavity. The best conditions are achieved under nitrogen purging and the WGP wires are oriented at 80^o.

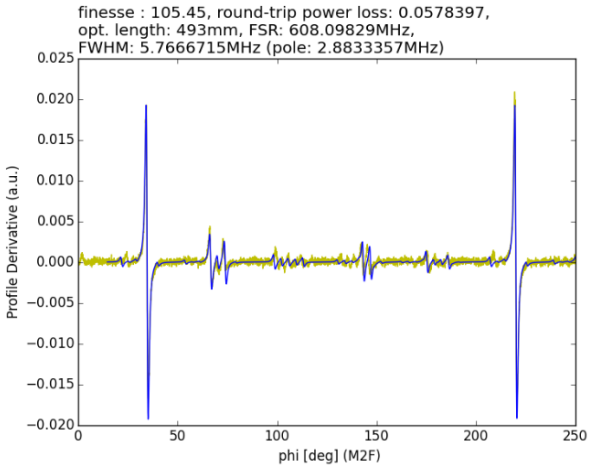

FIGURE 2.20: Comparison of the experimental (blue) and of the simulated spectrum (yellow) of the BTC in the experimental condition (Rm=99.9%, R_{WGP} =97.1%, T_{WGP}=1%). The finesse is 105.

In fact, in these conditions, the experimental spectrum gives a record finesse of 105.
This experimental spectrum is compared to the simulated spectrum as shown in Fig.2.20. The experimental spectrum has been acquired modulating the QCL current and scanning the cavity length. Furthermore, in order to simulate the experimental spectrum, the input parameters are the experimental ones ($R_m = 99.9\%$, $R_{WGP} = 97.1\%$, $T_{WGP} = 1\%$) and the beam shape is a Hermite-Gauss beam with $TEM_{0,1}$, $TEM_{1,0}$ and $TEM_{1,1}$. The simulated spectrum exactly reproduces the experimental one. In this optimal condition, further analyses have been performed.

Up to now, the transverse modes have been considered as the source of degradation for the cavity performance. Unexpectedly, the transverse modes are also optimal evaluator of the goodness of the finesse measured on longitudinal modes. The fundamental modes have more power so the more is their intensity, the more will be the intensity of the radiation that will come back on QLC and, as a consequence, the more will be the effect of the feedback on the real width of the peak.
The transverse modes are expected to be less affected by the feedback so their finesse is more reliable. The more similar are the finesses of longitudinal and transverse modes, the more the absence of feedback will be ensured, as shown in Fig.2.20 where the finesse reaches the record value of 105.

Chapter 3

Generation of terahertz comb by optical rectification based on Cherenkov effect

At the beginning of the long history of optics, all optical materials were considered linear. This assumption was a consequence of the observation that optical properties such as refractive index and absorption coefficient were independent from the light intensity. According to classical optics, the principle of superposition was applicable, and the light frequency remained unaltered after its passage in the medium. In addition, when two beams interacted in the same region of the medium they did not affect each other.
With the advent of the first lasers, higher intensities interacted with optical materials with the consequence that non-linear effects were observed. Detailed studies led researchers to observe that optical properties depended on the light intensity and the frequency of a beam was modified after its passage in a non-linear medium.
These fascinating phenomena led non-linear medium to many useful applications in the field of information technology, communications and sensors, for high precision spectroscopy and for the development of coherent light at different wavelengths.
In this thesis, non-linear optics is used to transfer the capabilities of Optical Frequency Comb Synthesizer, (OFCSs) to the terahertz region. The motivation is that THz FCSs have pushed the progress in THz metrology for their role as frequency rulers for any source in this spectral window. Thanks to this metrological tool, it is possible to determine the characteristics and the absolute frequency of a THz CW source (i.e. QCL) by detecting its beat-note with a tooth of a THz FCS. Moreover, in order to fully exploit the narrow intrinsic linewidth of QCL sources and to perform saturated absorption or cavity-enhanced spectroscopy setups, referencing the laser emission to a frequency standard such as THz FCS is required. In this way, in 2014, the line centre of a molecular transition was determined with an accuracy of $4.9\text{x}10^{-9}$ at $2.5THz$ by using a QCL metrologically referenced to a FCS [60]. The system consisted in a FCS generated by a non-linear crystal ($LiNbO_3$) by optical rectification of a Ti:Sapphire fs laser, emitting at 800 nm, and the generation was based on Cherenkov emission [61].
In this chapter, the improvement of the above mentioned metrological system is presented and discussed. Concerning the performance of the THz FCS, the

pump source has been changed. The latter has been upgraded to an Erbium fiber fs-laser, working at 1.5 μ wavelength, with 350 mW average power, 250 MHz of repetition rate and with $\sim 60 fs$ time width pulses.
The first part of this chapter concerns the theoretical aspect of the comb generation in a non-linear crystal. I will define a OFCS giving more details about the terahertz region. Then, I will discuss the relevant aspects of the theory of non-linear interactions and the non-linear optical methods to generate THz comb with an optical rectification process. The second part of this chapter deals with the experimental realization of the THz comb, the description of the non-linear crystal used for the generation of THz light, the characterization of the pump laser, the alignment step and the characterization of the THz comb.

3.1 Theory of frequency comb synthesizer

An optical frequency comb can be simply described as a pulsed source with specific properties that give it the fundamental metrological role [62]. Frequency combs act as rulers in the frequency domain and are generally realized starting from a short-pulse mode-locked laser [63]. Nevertheless, in this thesis, a non-linear process is used to generate the THz FCS, as will be described in the following section.
Before to describe a THz FCS, it is worth to discuss the mode-locking process in order to easily understand the nature of comb.
A laser is called "mode-locked" when produces pulses of light of extremely short duration, e.g. on the order of picoseconds or femtoseconds, by inducing a fixed-phase relationship between the longitudinal modes of the laser cavity. Interference between these modes forces laser light to be composed of a train of pulses.

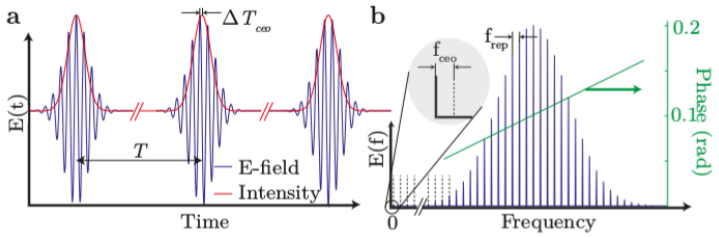

FIGURE 3.1: On the left: temporal view of electric field (blue curve) and of the intensity (red curve) of the frequency comb. The pulsed structure is equally spaced by the period (T) with a phase factor of ΔT_{ceo}. On the right: spectrum of the electric field. Each frequency is equally separated from the near one by f_{rep} and the spectrum is shifted of f_{ceo} from the origin. The dependence of the phase from the frequency is shown in green.

In the temporal domain (Fig.3.1), the structure of the mode-locked laser consists of pulses separated by the same period (T) and with a phase factor

(ΔT_{ceo}). Considering these series of pulses, with an amplitude of P, a repetition rate of $f_{rep} = 1/T$ and a temporal width of τ, the peak power is defined as:

$$P_{peak} = \frac{E_{peak}}{\tau} \tag{3.1}$$

where E_{peak} is the peak energy, and the average power is:

$$\bar{P} = E_{peak} * f_{rep}. \tag{3.2}$$

Differently, in the frequency domain, its spectrum is like a "comb", made by a set of modes equally spaced by the repetition rate (f_{rep}), i.e. the inverse of the period (T). Furthermore, this comb structure is shifted from the zero frequency by the so-called carrier-envelope offset frequency (f_{CEO}) which is the corresponding frequency of the temporal phase factor.
As a result, the ensemble of comb frequency lines at frequencies f_n is described by the following equation:

$$f_n = f_{off} + n f_{rep}. \tag{3.3}$$

In this way, the spectral coverage (S) consists of a series of N-delta with amplitude A ($\sim \bar{P}\tau f_{rep}$) and equally spaced by f_{rep}. In this description, the average power $\bar{P}$ can be expressed as:

$$\bar{P} = NA \tag{3.4}$$

since $N = S/f_{rep}$ and $S = 1/\tau$,

$$\bar{P} \sim \frac{SA}{f_{rep}} \sim \frac{A}{\tau f_{rep}}. \tag{3.5}$$

If the spectral coverage (S) has an octave-spanning emission, the mode-locked laser is called as *frequency comb*. The reason is that the octave-spanning emission allows the stabilization of the comb spectrum. Indeed, looking at eq.3.3, a comb line is identified by the comb parameters (f_{off}, f_{rep}) and by the order of the comb tooth (n). This implies that a comb line frequency can be stabilized through its two parameters. In other words, simultaneous control over the two degrees of freedom of such a comb (the repetition frequency, f_{rep}, and the carrier-envelope offset frequency, f_{off}) is essential for a full knowledge of the comb. For istance, a way to stabilize the repetition rate frequency (f_{rep}) deals with methods acting on the stabilization of the laser cavity. In this case, the metrological reference can be given, e.g., by a quartz rubidium Global Positioning System (GPS) chain reference.
Instead, the most used and the most efficient way to stabilize the offset frequency (f_{off}) consists on the self-referencing "*f-2f*" method [64]. This method requires octave-spanning laser emission and allows also the determination of the carrier-envelope offset frequency of the comb having a total control of the comb. Achieving an octave-spanning spectrum is therefore a milestone to use a broadband laser as a potential frequency comb.
Another important property of a comb is that, when its emission is stabilized

by phase locking the repetition rate and the offset to highly stable reference standard, the noise level is strongly reduced. For these properties and for its high stability, the frequency comb can be effectively used in metrology and high-precision spectroscopy as an absolute frequency reference.
In this way, frequency combs act as rulers in the frequency domain where the accuracy of the frequency measurement is only limited by that of the reference. This is the reason why femtosecond frequency combs have revolutionized optical frequency metrology.

3.1.1 Frequency comb synthesizers for terahertz frequencies

Optical frequency combs have been demonstrated in the visible and mid-infrared (mid-IR) region [65]. Recently, this technology has been transferred to the THz spectral region thanks to non-linear optics [66]. The resulting THz spectrum with comb-like structure can be used to calibrate THz radiation sources. An accurate phase-lock of THz CW sources to THz combs, can open the way to new possibilities for high-resolution THz spectroscopy.
In this thesis, the THz frequency comb has been generated in a MgO doped lithium niobate waveguide by optical rectification, based on the Cherenkov configuration. The pump is a femtosecond mode-locked fiber laser emitting around 1.5 μm at a repetition rate (f_{rep}) around 250 MHz.
The optical rectification process, described in the following section, produces a zero-offset free-space THz comb with a spectral content from 0 THz to 6 THz. In this case, the frequency (f_n) of each tooth of the THz FCS can be parameterized as:

$$f_n = n * f_{rep} \tag{3.6}$$

that it is precisely a free-standing THz comb with zero offset and same repetition rate (f_{rep}) of the pump femtosecond pulse laser.
For the sake of completeness, it is worth to discuss the expression of the average power both in the temporal and the frequency domain for the free-standing THz comb with zero offset.

The THz comb is generated for a second order non-linear process, therefore the expression for the peak power ($P_{peak,THz}$) depends on the square of the pump peak power ($P_{peak,pump}$):

$$P_{peak,THz} \prec P^2_{peak,pump} \tag{3.7}$$

and substituting the expression for the P_{peak} (eq. 3.1) into the previous equation, it follows that:

$$\frac{E_{peak,THz}}{\tau} \prec \frac{E^2_{peak,pump}}{\tau^2} \tag{3.8}$$

Then, considering that $1/\tau = f_{rep}$ and using the expression for the $\bar{P}$ (eq. 3.2), the relationship between the power of the THz comb and the pump laser is:

$$\bar{P}_{THz} \prec \frac{\bar{P}^2_{pump}}{f_{rep} * \tau}. \tag{3.9}$$

On the other hand, in the frequency domain the amplitude of the k-th tooth can be expressed as:

$$A_k^{THz} \sim \sum_{i,j}^{i-j=k} A_i A_j \sim A^2(N-k)$$

and, for eq.3.5, it follows that:

$$\bar{P}_{THz} \sim \sum_k^N A_k^{THz} \sim A^2 \sum_k^N (N-k) \sim A^2 N^2 \sim \frac{\bar{P}^2_{pump}}{(\tau f_{rep})} \tag{3.10}$$

that is exactly the result obtained in the temporal domain.

3.2 Theory of optical rectification

In the following section, optical rectification (OR) process is described. First, I will report the non-linear process theory, and then I will describe the details of the THz generation.

3.2.1 Non-linear optics

When an optical electromagnetic wave propagates in a non-linear medium, the relationship between the polarization (P) of the medium and the electric field ($\vec{E}$) is expressed in the following way:

$$P_{NL} = \epsilon_0(\chi^{(1)} : \vec{E} + \chi^{(2)} : \vec{E}\vec{E} + \chi^{(3)} : \vec{E}\vec{E}\vec{E} + ...) \tag{3.11}$$

where ϵ_o is the permittivity of free space, $\chi^{(1)}$ is the linear dielectric susceptibility of the medium, $\chi^{(i)}$ $(i = 2, ..)$ is the non-linear dielectric susceptibility coefficient that describes the strength of each order.
The tensor notation should be interpreted as follows by taking as an example the second-order term:

$$P_i^{(2)} = (\chi^{(2)} : \vec{E}\vec{E})_i = \sum_{j,k=1}^{3} \chi_{ijk}^{(2)} E_j E_k \tag{3.12}$$

More specifically, concerning the susceptibility, its first order, $\chi^{(1)}$ describes linear optics, e.g. as lenses work. Instead, $\chi^{(2)}$ describes second-order effects (e.g., second harmonic generation, optical rectification) that vanishes if the material possesses an inversion symmetry (a centro-symmetric medium) and so on for the following orders.
When a light beam propagates in a non-linear medium, its propagation is described by the wave equation, derived from Maxwell's equations for an arbitrary homogeneous, isotropic dielectric medium. The wave equation that

governs the generation of light at frequencies of the exciting fields or lower is given by:

$$\nabla^2 \vec{E} - \frac{1}{c_0^2}\frac{\partial^2 \vec{E}}{\partial t^2} - \mu_o \frac{\partial^2 P_{NL}}{\partial t^2} = 0 \tag{3.13}$$

where the non-linear polarization (P_{NL}) contains frequency components which are not present in the exciting beam(s) and light with such frequencies can be generated in the medium. The electric field($\vec{E}$) in the previous equation concerns all the waves that can be a solution to the Maxwell equation. For each interacting field, from eq.3.13, n-equations are obtained and form a set of $(n+1)$ coupled equations. More specifically, the non-linear wave equation can be solved using the theory of perturbations and applying some approximations such as the slow varying envelope approximation[1].
In order to better explain the non-linear process, it can be considered an interacting electric field (a planar wave) composed of two frequencies:

$$\vec{E}(\vec{r},t) = \vec{E}_{01}(\vec{r},t)\exp i(\vec{k_1}\cdot\vec{r} - \omega_1 t) + \vec{E}_{02}(\vec{r},t)\exp i(\vec{k_2}\cdot\vec{r} - \omega_2 t) \tag{3.14}$$

Within the instantaneous response approximation, the polarization at the first order induced by this incident field is:

$$\vec{P}^{(1)}(\vec{r},t) = \epsilon_0\chi^{(1)}(\omega_1)\vec{E}_{01}(\vec{r},t)e^{i(\vec{k_1}\cdot\vec{r}-\omega_1 t)} + \epsilon_0\chi^{(1)}(\omega_2)\vec{E}_{02}(\vec{r},t)e^{i(\vec{k_2}\cdot\vec{r}-\omega_2 t)} \tag{3.15}$$

In order to simplify this expression, one can consider that $\vec{k_1}, \vec{k_2} \parallel \vec{i}$, $\vec{E}_{02} \parallel \vec{k}$ and that the medium is uniform and isotropic. By placing the obtained expression in the wave equation and after decoupling the equations for $i = 1, 2$, at the first order, it can be demonstrated that the following system hold:

$$\begin{aligned} \vec{\nabla}\wedge(\vec{\nabla}\wedge\vec{E}_1) + \frac{1}{c^2}\left(1+\chi^{(1)}(\omega_1)\right)\frac{\partial^2\vec{E}_1}{\partial t^2} = 0 \\ \vec{\nabla}\wedge(\vec{\nabla}\wedge\vec{E}_2) + \frac{1}{c^2}\left(1+\chi^{(1)}(\omega_2)\right)\frac{\partial^2\vec{E}_2}{\partial t^2} = 0 \end{aligned} \tag{3.16}$$

This means that, in the linear approximation, the medium emits waves at the same frequency of the input beam, but the waves move with different velocity with respect to the one of the incident wave.
However, in a more general case, the electric field can be expressed as a combination of n-planar waves which are functions of $\vec{k_l}$ and ω_l:

$$\vec{E}(\vec{r},t) = \sum_{l=0}^{n}\vec{E}_l(\vec{k_l},\omega_l) = \sum_{l=0}^{n}\vec{E}_{0l}\exp i(\vec{k_l}\cdot\vec{r} - \omega_l t) \tag{3.17}$$

[1]The slow varying envelope approximation is the assumption that the envelope of a forward-travelling wave pulse varies slowly in time and space compared to a period or wavelength.

where the amplitude $\vec{E}_{0l}$ is considered independent from time and stands for the coefficient that describes the strength of each harmonic. In this case, the total polarization for the medium can be written as:

$$\vec{P}(\vec{r},t) = \vec{P}^{(1)}(\vec{r},t) + \vec{P}^{(NL)}(\vec{r},t) \tag{3.18}$$

with

$$\begin{aligned}\vec{P}^{(1)}(\vec{r},t) &= \sum_l \vec{P}_l^{(1)}(\vec{k}_l,\omega_l) = \sum_l \chi^{(1)}\vec{E}_{0l}\exp i(\vec{k}_l\cdot\vec{r}-\omega_l t)\\ \vec{P}^{(NL)}(\vec{r},t) &= \sum_{n\geq 2}\vec{P}^{n}(\vec{r},t) = \sum_m \vec{P}^{NL}(\vec{k}_m,\omega_m) = \sum_m \vec{P}_{0m}^{NL}\exp i(\vec{k}_m\cdot\vec{r}-\omega_m t)\end{aligned} \tag{3.19}$$

Then, considering eq.3.13, the wave propagation and generation inside the crystal is governed by the wave equation written in the following way:

$$(\vec{\nabla}\wedge(\vec{\nabla}\wedge) - \frac{\omega^2}{c^2}\left(1+\chi^{(1)}(\omega_l)\right))\,\vec{E}(\vec{k},\omega) = \frac{\omega^2}{c^2}\vec{P}^{NL}(\vec{k}_m,\omega_m=\omega) \tag{3.20}$$

which is the equation that describes the propagation of n-fields ($E_l(k_m,\omega)$) with a different frequency with respect to the incident waves. In other words, the waves mutually interact through the non-linear polarization, and the frequency and phase matching conditions have to be satisfied in order to ensure the energy and momentum conservation laws. As a matter of fact, since $\hbar\omega$ and $\hbar k$ are the energy and momentum of a photon with a frequency ω and wavevector $\vec{k}$, the energy and momentum conservation law are:

$$\hbar\omega_{out} = \sum_i \hbar\omega_{i,in} \tag{3.21}$$

$$\hbar\vec{k}_{out} = \sum_i \hbar\vec{k}_{i,in} \tag{3.22}$$

As a consequence, the phase mismatch factor ($\Delta\vec{k} = \vec{k}(\omega_{out}) - \vec{k}(\omega_{in})$) is crucially important in determining the efficiency of non-linear optical interactions. Indeed, the conversion efficiency is useful to quantify the quality of the non-linear generation and is defined as the ratio between the generated field I(ω_{out}) and the input one I(ω_{in}):

$$\eta = \frac{I(\omega_{out})}{I(\omega_{in})} \tag{3.23}$$

3.2.2 Second-order non-linearity

In this section, the optical properties of a non-linear medium are discussed when non-linear terms of higher order than the second are neglected.

Two monochromatic waves with frequencies ω_1 and ω_2 are supposed to interact with the non-linear medium. As said before, the latter emits light waves with frequencies given by a combination of the incident ones, i.e. the three-wave interaction.
The solution to the three waves interaction leads to a non-linear polarization composed of the following terms:

$$\begin{aligned} &P^{(2)}(\omega_3 = 2\omega_i) = \epsilon_0 \chi^{(2)} E_i^2 \qquad i = 1,2 \qquad SHG \\ &P^{(2)}(\omega_3 = \omega_1 + \omega_2) = 2\epsilon_0 \chi^{(2)} E_1 E_2 \qquad SFG \\ &P^{(2)}(\omega_3 = \omega_1 - \omega_2) = 2\epsilon_0 \chi^{(2)} E_1 E *_2 \qquad DFG \\ &P^{(2)}(\omega_3 = 0) = 2\epsilon_0 \chi^{(2)} (E_1 E *_1 + E_2 E *_2) \qquad OR \end{aligned} \tag{3.24}$$

All these terms have the same non-linear susceptibility and each expression is labelled with the acronym of its physical process.
More specifically, the combination of the incident frequencies gives rise to new frequencies: $\omega_{3,4} = \omega_1 \pm \omega_2$ corresponding to the sum (SFG) and difference frequency (DFG). When $\omega_1 = \omega_2$, there are two special cases of conversion, namely, second–harmonic generation (SHG) and optical rectification (OR). The SHG ($\omega_3 = 2\omega_1$) is a special case of the sum frequency generation (SFG), while the OR ($\omega_4 = 0$) is a special case of difference frequency generation (DFG).
Considering the Maxwell equation, e.g. for the SFG, the coupled waves obtained from the eq.3.20 are:

$$\begin{aligned} (\vec{\nabla} \wedge (\vec{\nabla} \wedge -\frac{\omega_1}{c^2} \left(1 + \chi^{(1)}(\omega_l)\right) \vec{E}_1(\vec{k}_1, \omega_1) = \frac{\omega_1^2}{c^2} P^{(2)}(\omega_1) = \\ = \frac{\omega_1^2}{c^2} \chi^{(2)}(\omega_1 = -\omega_2 + \omega_3) : \vec{E}_2^*(k_2, \omega_2) \vec{E}_3(k_3, \omega_3) \\ (\vec{\nabla} \wedge (\vec{\nabla} \wedge -\frac{\omega_2}{c^2} \left(1 + \chi^{(1)}(\omega_2)\right) \vec{E}_2(\vec{k}_2, \omega_2) = \frac{\omega_2^2}{c^2} P^{(2)}(\omega_2) = \\ = \frac{\omega_2^2}{c^2} \chi^{(2)}(\omega_2 = \omega_3 - \omega_1) : \vec{E}_3(k_3, \omega_3) \vec{E}_1^*(k_1, \omega_1) \\ (\vec{\nabla} \wedge (\vec{\nabla} \wedge -\frac{\omega_3}{c^2} \left(1 + \chi^{(1)}(\omega_3)\right) \vec{E}_3(\vec{k}_3, \omega_3) = \frac{\omega_3^2}{c^2} P^{(2)}(\omega_3) = \\ = \frac{\omega_3^2}{c^2} \chi^{(2)}(\omega_3 = \omega_2 + \omega_1) : \vec{E}_1(k_1, \omega_1) \vec{E}_2(k_2, \omega_2) \end{aligned} \tag{3.25}$$

where the non-linear susceptibilities are coupled coefficients that determine the rate of the energy transfer between the waves. Furthermore, for a non-dissipative medium holds the commutation law $\chi_{ijk}^{(2)*}(\omega_3) = \chi_{jki}^{(2)}(\omega_1) = \chi_{kij}^{(2)}(\omega_2)$ which is the condition according to the fact that the energy of the three waves remains constant during the process.
In the state-of-art, SFG is frequently used for conversion of long-wave radiation, for instance, infrared (IR) radiation, to short–wave radiation, UV or

visible light. On the contrary, DFG is used for conversion of short–wave radiation to long–wave radiation. The latter is the physical process involved in the generation of the THz comb, for which particular attention will be given in the following section.

Difference Frequency Generation

In a DFG process the medium acts as a light source for a wave with a frequency given by the frequency difference of the input beams, i.e. $\omega_3 = \omega_2 - \omega_1$ (*frequency matching condition*). The electric field of the output beam propagates with a complex amplitude proportional to $exp(-i\Delta\vec{k'} \cdot \vec{r})$, where $\Delta\vec{k'} = \vec{k_3} - \vec{k_2} - \vec{k_1}$ according to the *phase matching condition*.
In order to retrieve the solution of the system (3.20) for the DFG, one can consider the transverse properties of an electromagnetic wave ($\nabla \cdot \vec{E} = i\vec{k} \cdot \vec{E} = 0$) and a field with linear polarization along z axis, propagating along x axis. After many mathematical steps, the equation for the generated wave is:

$$\frac{\partial E_{03}}{\partial x} = \frac{i\omega_3^2}{2k_3c^2}\chi^{(2)}E_{01}E_{02}e^{i(k_1+k_2-k_3)x} \tag{3.26}$$

and after some considerations about the DFG process, the expression for E_{03} is obtained and the conversion efficiency results:

$$\eta_{DFG} = \frac{8\pi^2}{\epsilon_0 c}\frac{d_1^2}{\lambda_1^2\lambda_2^2 n_1 n_2 n_3}\frac{L^2}{A}sinc^2\left(\frac{\Delta k' L}{2}\right) \tag{3.27}$$

where d_1 is the non-linear constant, λ_i (with $i = 1, 2$) is the wavelength of the incident beam, n_i (with $i = 1, 2, 3$) is the refractive index of the medium for each wave, L is the interaction length and A is the corresponding area.
In the previous equation, the term $sinc(\Delta k' L/2)$ comes from the interference between the waves. More specifically, when $\Delta k' \neq 0$, the power generated at some plane (z_1), after propagating to some other plane (z_2), is not in phase with the wave generated at z_2.
In order to maximize the efficiency, the factor L^2/A has to be improved. This can be done by focusing the incident beam to the smallest possible area A and provide the longest possible interaction length L. However, if the dimensions of the non-linear crystal are not limiting factors, the maximum value of L for a given area A is limited by beam diffraction. In this case, the efficiency is proportional to L. For a thin crystal, L is determined by the crystal and the beam should be focused to the smallest spot area A. For a thick crystal, the beam should be focused to the largest spot that fits within the cross-sectional area of the crystal.
To this purpose, guided-wave structures offer the advantage of light confinement in a small cross-sectional area over long distances. Since A is determined by the size of the guided mode, the efficiency is proportional to L^2. The advantages of using a waveguide concerns the possibility to confine the light throughout a long optical path in a small section. In this way, the light is confined near the surface of the crystal providing a smaller THz absorption

with respect to the one obtained with a bulk crystal, providing an improvement of the generation efficiency.

Optical rectification

As said before, the optical rectification is the degenerate case of difference frequency generation for which $\omega_2 = \omega_1$, $|\vec{k}_1|^2 = |\vec{k}_2|^2$ and a wave with $\omega_3 = 0$ is generated.
The process can be explained in the following way. The OR corresponds to a steady polarization density that creates a DC potential difference across the plate of a capacitor within which the non-linear material is placed. The generation of a DC voltage, because of an intense optical field, is the optical rectification.

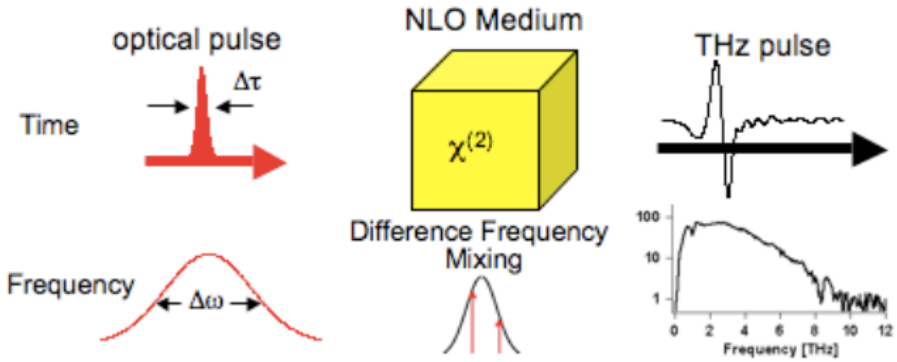

FIGURE 3.2: In the time domain, the THz pulse is the envelope of the optical pulse that interacts with the non-linear material. In the frequency domain, the THz spectrum is made of the difference frequency mixing of the frequencies contained into the input beam.

In the same way, when an ultra-short laser excites a non-linear medium, the latter performs, at any given time, a rectification of the input signal resulting in a pulse which is the envelope of the pump pulse.
In the frequency domain, as described in section 3.1, the pump pulse is made of a set of modes equally spaced by a quantity which is the repetition rate and shifted of a quantity that is the offset. An alternative way to explain OR is the frequency difference between each modes pair of the input beam. In other words, this process concerns as the DFG associated with the beating of the various Fourier components of the optical pulse (Fig.3.2).
As a consequence of the difference between each possible pair of frequencies, a new comb is generated with teeth equally spaced by the repetition rate and with zero offset. More specifically, by considering the frequencies of two teeth: $f_n = f_{off} + nf_{rep}$ and $f_m = f_{off} + mf_{rep}$, the resulting tooth is:

$$f_l = f_n - f_m = (n - m)f_{rep} \tag{3.28}$$

This means that, when the intense field of a visible/near infrared pulse excites a non-centro symmetrical crystal, terahertz comb can be generated according to this mechanism.

In this process, the resulting second-order non-linear source polarization, at a specific difference frequency (Ω) is expressed as:

$$\vec{P}^{(2)}(\Omega) = \int_{-\infty}^{+\infty} \chi^{(2)} : \vec{E}_{opt}(\omega + \Omega)\vec{E}^{*}_{opt}(\omega)d\omega \tag{3.29}$$

where $\vec{E}_i(\omega)$ with $i = (opt, THz)$ are, respectively, the Fourier components of the electric field of the optical and THz pulses, as defined by $\vec{E}_i(t) = \int_{-\infty}^{+\infty} \vec{E}_i(\omega)e^{-j\omega t}d\omega$. If the non-linear susceptibility is independent from the frequency, in the time domain, the non-linear source polarization of eq.3.29 is reduced to:

$$\vec{P}^{(2)}(t) = \chi^{(2)} : \vec{E}_{opt}(t)\vec{E}^{*}_{opt}(t) \tag{3.30}$$

Thus, for a non-linear medium with nearly instantaneous response, the slowly-varying component of the non-linear source polarization follows the intensity envelope of the optical excitation pulse. This is the reason why such a DFG process is generally referred to optical rectification process.
In this process, the way to improve the efficiency is connected to the thickness of the crystal and propagation effects has to be taken into account. Typically, the most critical effect is the interaction of the relative propagation of the optical and THz waves, which is the phase-matching condition, given by:

$$\Delta\vec{k} = \vec{k}(\omega + \Omega) - \vec{k}(\omega) - \vec{k}(\Omega) = 0 \tag{3.31}$$

In order to satisfy the phase-matching condition, different structures of crystal can be setup, as will be shown in the following section.

3.2.3 Non-linear crystals for THz generation

The commonly investigated materials for THz emission via OR mechanism include semiconductors [67] such as GaAs, ZnTe, InP, InAs, InSb, GaSe, CdTe, CdZnTe, dielectric crystals such as $LiNbO_3$, $LiTaO_3$, organic materials such as DAST [68], polymers, and thin layer of metals such as gold [69]. All these materials have some advantages and disadvantages.
For example, ZnTe guarantees phase matching of Ti:sapphire laser pulses ($\sim$ 800 nm wavelength) with a collinearly propagating wave. Nevertheless, the non-linear coefficient of ZnTe [70] is lower than the one of other materials, such as $LiNbO_3$, $LiTaO_3$, or DAST. In addition, ZnTe is affected by relatively high terahertz absorption ($\sim$ 10 cm^{-1} at room temperature) and strong two-photon absorption of the Ti:sapphire laser radiation at high laser intensities. These factors lead to saturation of terahertz field at high laser intensities and therefore the optical to terahertz conversion efficiency in ZnTe is typically around 10^{-6} - 10^{-5} [71], [72].
The most used crystal is the lithium niobate ($LiNbO_3$) [73], [74] because of its high non-linearity, high transparency in the near infrared frequencies and large band gaps even if in THz band presents a high absorption. Indeed, the $LiNbO_3$ intensity absorption coefficient increases from about 16 cm^{-1} at 1 THz to more than 170 cm^{-1} at 2.5 THz at room temperature [68], [75].

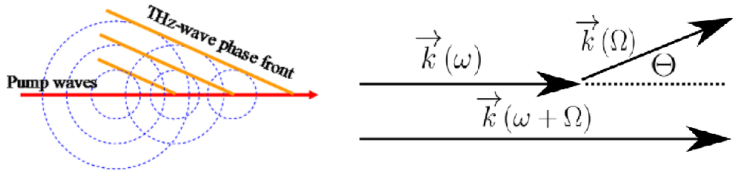

FIGURE 3.3: Cherenkov-type phase-matching condition in the temporal domain (on the left) and in the frequency domain (on the right). The THz wave ($\vec{k}(\Omega)$) is emitted at an angle of Θ coming from the difference of two wavefront vectors of the pump at two different frequencies ($\vec{k}(\omega)$, ($\vec{k}(\omega+\Omega)$)). Figure is reprinted from Ref.[76].

Looking at the physical process, when the pump laser interacts with the crystal, the excited non-linear polarization moves with the group velocity of the pulse. According to the dispersion properties of the crystal, the terahertz pulse can be faster or slower than the exciting polarization leading respectively to a superluminal or a subluminal regime [77].
In the latter regime, also known as phase-matched, the group velocity of the pump pulse is lower than the phase velocity of the THz wave that propagates in the material. On the other hand, in the superluminal regime, also known as Cherenkov or non-phase-matched, there is something like to what happens to a supersonic jet. The pump pulse is similar to a relativistic particle that emits a Cherenkov radiation [78]: THz wave is emitted in the same way as a Cherenkov radiation is emitted by a relativistic particle (Fig. 3.3).
Although the distinction of terahertz generation as subluminal and superluminal regimes is useful for wide optical beams, there are no principal differences between the two regimes for focused beams.
In the superluminal regime, phase matching is achieved between a strongly focused moving optical pulse and a plane terahertz wave propagating under some angle with respect to the laser path. The focused pulse excites a continuum of plane waves with different frequencies and different propagating angles because of the dispersion. Moreover, the area in which the optical pulse is focused must be smaller or equal to the terahertz wavelength. Indeed, recently, it has been demonstrated [79] that, when the size (r_o) of the optical beam is comparable to or smaller than the wavelength of the THz radiation, the THz pulse power increases as the beam size increases.
Typically, for these phenomena the excitation beam is a pulsed laser, centred at 800nm while, in this thesis the pump laser is centred at 1550nm. Up to now, the extension to 1550nm is motivated by the fact that this wavelength is typically used for telecommunications with the consequence that these lasers are inexpensive and compact.
As said before, the Cherenkov phase-matching condition is satisfied when the velocity of the polarization wave inside the nonlinear crystal is greater than the velocity of the radiated wave outside. In this way, the radiation angle is determined by the refractive index of the pumping wave in the crystal, and that of THz-wave in the crystal. For example, considering the crystal used in this thesis ($LiNbO_3$), the Cherenkov angle is given by:

$$\theta_C = arccos\left(\frac{n_{NIR}}{n_{THz}}\right) \approx 65^o \tag{3.32}$$

where the refraction index is $n_{NIR} = 2.2$ at infrared light and $n_{THz} = 5.2$ at terahertz waves.
Unfortunately, with such a crystal, i.e. a superluminal material, the terahertz wave undergoes to total internal reflection at the crystal boundary making difficult the extraction of the terahertz wave.

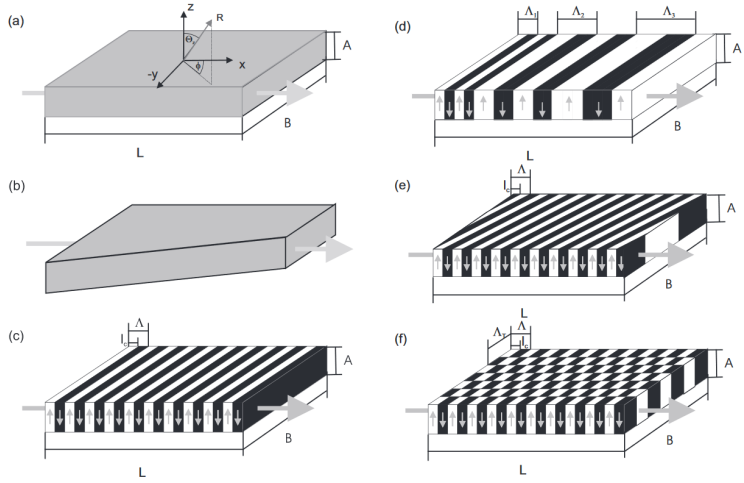

FIGURE 3.4: Different poling structures of superluminal crystal. a)bulk, b) Cherenkov cut, c) periodically poled, d) aperiodically poled, e) periodically tilted (slant stripe), f) chessboard type. Figure is reprinted from Ref. [80].

To exceed this obstacle, crystals are tailored at defined angle or coupled with extracting prism otherwise, superluminal crystals can be lithographed with different poling structure, such as periodically, aperiodically, periodically tilted, and uniform, as shown in Fig.3.4.
The efficiency of the optical to THz conversion is essentially depended on the structure and on the characteristic of the material such as its non-linear coefficient, velocity mismatch between the optical pulse and terahertz waves, optical transparency, and absorption at terahertz light.
To achieve the quasi-phase-matching condition for large aperture laser beams, it is more convenient the use of structures with periodically inverted sign of second-order susceptibility such as periodically poled lithium niobate crystal. Using this configuration, it is possible to extract a pulsed light with a spectral coverage of some THz.
Various materials with low loss in the FIR and favourable non-linear characteristics have been exploited to generate intense broadband THz radiation. Ultra-broadband radiation extending up to several tens of THz has been produced in GaAs crystals via the second-order non-linearity, but at the expense of efficiency, since only a thin layer of the sample (corresponding to the optical penetration depth) contributes to the signal.
In order to enhance the generation efficiency and the total power, longer interaction lengths are desirable, but requiring consideration of relevant wave propagation phenomena. These include linear propagation effects for both

the visible and THz pulses, as well as phase matching for the non-linear process. The latter turns out to be critical for efficient conversion of the broad bandwidth of ultrafast optical pulses into the THz spectrum.
In the actual state-of-art, relatively high conversion efficiencies (10^{-5}) have been reached for femtosecond pulses at 800 nm used to generate THz wave via optical rectification in a cryogenically cooled (18K) periodically poled lithium niobate crystal (PPLN) [81].
Another way to achieve phase matching in a superluminal material is the use pump pulses with tilted fronts.
The operation principle has been demonstrated by generating subpicosecond pulses at approximately 2 THz in $LiNbO_3$ crystal, cooled down to 77K, achieving a record conversion efficiency of $4.3x10^{-5}$[82]. In this context, the conversion efficiency reached in this work has achieved an important level. As will be shown, an efficiency of 10^{-4} has been reached at room temperature, by using a fs-fiber laser in a Cherenkov-configuration with a $LiNbO_3$ crystal.

3.3 Experiment

In this section, the experimental realization of the THz-FCS is described. First, the characterization of the pump source is performed, and the temporal width of its pulses is measured. Then, the pump is aligned into the waveguide of the non-linear crystal where the THz generation takes place. Finally, the detection of the generated THz light is optimized.

3.3.1 Pump characterization

The pump source is an erbium fiber fs-laser (MENLO), working at 1.5 μm wavelength, with 350 mW average power. The pulse temporal width is less than 50fs and the pulse repetition rate is 250 MHz.

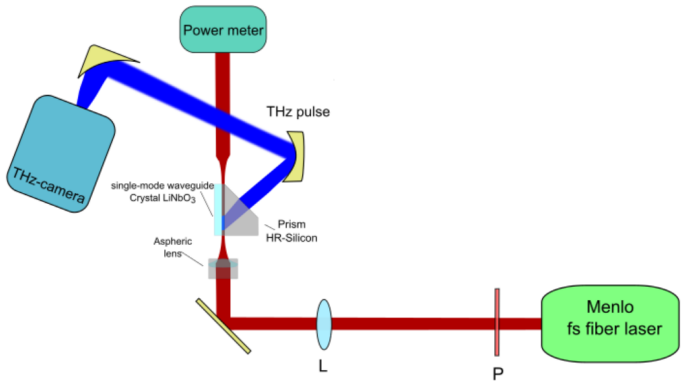

FIGURE 3.5: Experimental setup for the THz generation. The erbium fiber fs-laser (MENLO) is aligned into the crystal. The light emitted by the waveguide of the crystal is revealed with a power meter. The generated THz is collected with a cylindrical mirror and detected with a couple of a parabolic mirror and a THz-camera.

A sketch of the experimental setup, used to inject the pump laser in the crystal and to extract the THz comb, is shown in Fig.3.5.
The pump laser is focused on the single-mode linear waveguide of the crystal. In order to couple the light in the crystal waveguide, the beam section is required to be comparable with the dimension of the waveguide facet. To this purpose, the beam is pre-shaped with a lens (L), with a focal length of 500 mm, placed at 200 mm from the crystal. In this way, the beam section is adjusted to illuminate a collimator, placed at its focal length from the crystal and used to correct the beam waist.
A polarizer (P) is used to adjust the polarization of the incoming beam according to the one required by the crystal waveguide, i.e. polarization sensitive. More specifically, the required polarization is parallel to the axis of the crystal.
Once the infrared light has been coupled to the waveguide, the light is collected by a removable collimator in order to check the coupled signal. In this way, the alignment of the beam is optimized by improving the coupled light, easily measured as the ratio between the power of the input beam and the power of the output beam from the crystal. From the tabulated waveguide specifications, the expected maximum coupling factor is 52% but the measured value is 41% because of the absorption of the two collimators used to focus and to collect the beam.

Techniques for the measurement of the temporal width of a pulse

In many applications, the measurement of the laser pulse duration becomes necessary. In this case, the pulse temporal width of a fiber laser is hundreds of femtoseconds, and cannot be measured with detectors, that have a much slower time response.
The solution comes from the intensity autocorrelator technique that gives a direct measurement of the temporal width.
From a mathematical point of view, given a function $f(t)$, the respective autocorrelator function $A(t)$ is defined as:

$$A(\tau) = \int_{-\infty}^{+\infty} f(t) f^*(t+\tau) \tag{3.33}$$

where τ is a temporal delay.
The basic principle consists on the interference of the beam with its copy delayed in the time. These copies are superimposed in a nonlinear medium (a crystal or the detector itself) where a two-photons process ensures the interaction of the two beams. The acquired signal is exactly the autocorrelation.
Therefore, the assessment of the coherence properties of a mode locked laser is usually performed by an autocorrelation measurement on a non-linear crystal to reveal the temporal width of the optical pulse. In other words, optical autocorrelators result the best devices to measure the temporal width of a pulse.

This measurement can be done with a simple setup such as a Michelson-interferometer configuration. The field autocorrelation is measured by placing a slow detector at the output of the Michelson interferometer. Indeed, the beam is divided in two identical beams, one of which is directed on a translational stage to provide a time delay with respect to the other fraction. Then, the two beams are recombined and acquired by the slow detector.
In this case, the function $f(t)$ of eq. 3.33 is the electrical field of the laser source. More specifically, the output field ($E(t,\tau)$) from the Michelson interferometer, is given by the sum of two identical pulses delayed by τ with respect to each other:

$$E(t,\tau) = E(t+\tau) + E(t) = A(t+\tau)e^{j\omega_c(t+\tau)+j\phi_{ce}} + A(t)e^{j\omega_c t+j\phi_{ce}} \tag{3.34}$$

where $A(t)$ is the complex amplitude and $e^{j\omega_c t}$ describes the oscillation term with the carrier frequency ω_c and ϕ_{ce} is the carrier-envelope phase. The signal induces a non-linear polarization in the crystal or detector, expressed as:

$$P^{(2)}(t) \prec (A(t+\tau)e^{j\omega_c(t+\tau)+j\phi_{ce}} + A(t)e^{j\omega_c t+j\phi_{ce}})^2 \tag{3.35}$$

which is valid only for the ideal case in which the paths for both beams are identical, on the contrary a phase-shift has to be taken into account. Then, the electric field of the second harmonic radiation is directly proportional to the polarization:

$$E^{(2)}(t,\tau) \prec (A(t+\tau)e^{j\omega_c(t+\tau)+j\phi_{ce}} + A(t)e^{j\omega_c t+j\phi_{ce}})^2 \tag{3.36}$$

Instead, the photo-detector usually has a response much slower than the pulse width thus the integral of the signal over time is:

$$I(\tau) \prec \int_{-\infty}^{+\infty} |(A(t+\tau)e^{j\omega_c(t+\tau)} + A(t)e^{j\omega_c t})^2|^2 dt \tag{3.37}$$

By expanding the previous equation, the interferometric autocorrelation function can be expressed by the following terms:

$$I(\tau) = I_{back} + I_{int}(\tau) + I_{\omega}(\tau) + I_{2\omega}(\tau) \tag{3.38}$$

where I_{back} is the background signal, $I_{int}(\tau)$ the intensity autocorrelator, $I_{\omega}(\tau)$ is the coherence term oscillating with ω_c, and $I_{2\omega}(\tau)$ with $2\omega_c$.
Nevertheless, the correct determination of the pulse width using the intensity autocorrelation requires some previous knowledge of the pulse shape. In fact, if the pulse shape is known, the pulse width can be extracted with the deconvolution of the correlation function.
For example, for a Gaussian time profile, the autocorrelation width results $\sqrt{2}$ longer than the pulse while it is 1.54 times longer than the case of a hyperbolic secant squared (sech^2) pulse. This numerical factor, sometimes called "deconvolution factor", depends on the shape of the pulse. If this factor is known,

or assumed, the time duration (intensity width) of a pulse can be measured using an intensity autocorrelation, even if the phase cannot be measured.

Looking at the profile of the interferometric autocorrelator, e.g. for a sech-shaped pulse, the profile is symmetric ($I(\tau) = I(-\tau)$). Differently, when the pulse propagates through a medium with a dispersion, it broadens. If the dispersion is further increased, the broadening increases and the interferometric autocorrelation signals show some characteristic nodes in the wings. Moreover, it can be demonstrated [83] that, also for a chirped pulse, the envelope of the pulse profile is not any longer real and the chirp [2] in the pulse results in characteristic nodes in the wings.

Non-linear autocorrelator

The non-linear autocorrelator system, used to measure the temporal width of the laser, consists in a Michelson interferometer. The pulse is compared with a displaced copy of itself and the output signal is the intensity autocorrelation of the input signal.

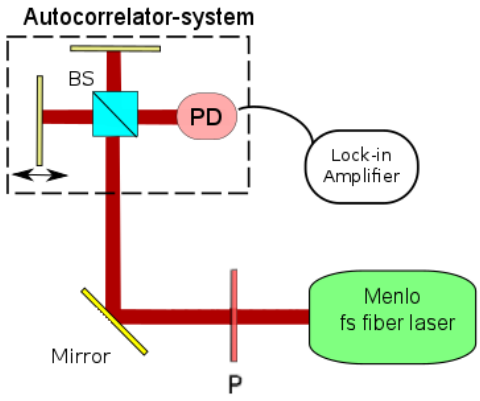

FIGURE 3.6: Experimental setup for the autocorrelator acquisition. A mirror is used to send the beam on the autocorrelator system in a Michelson configuration. The beam splitter (BS) divides the beam into two equal fractions. One of the two planar mirror is on a translational stage and the signal is detected by photodiode(PD) and with a lock-in amplifier.

The experimental setup used to perform the measurement of the temporal width is shown in Fig.3.6.
A removable mirror, placed before the crystal, is used to send the laser in the autocorrelator system. The beam is sent on a 50÷50 beam splitter (BS) that divides the beam into two fractions. Each beam is reflected by a planar mirror and sent to a BS where the two beams recombine. The resulting beam is acquired with a two-photon silicon photodiode (PD). A mechanical chopper modulates the beam intensity and a lock-in detection is performed.
In order to scan along the autocorrelator function, one of the planar mirrors

[2]The chirp of an optical pulse is defined as the time dependence of its instantaneous frequency. Specifically, an up-chirp (down-chirp) means that the instantaneous frequency rises (decreases) with time.

is mounted on a motorized translation stage (ThorLabs, mod. MTS25) controlled by a LabVIEW program. Moreover, the software allows to select the scanning speed (typical value 1 mm/s), the total scan length (typically 300μ m) and the acquisition rate (150 ms).

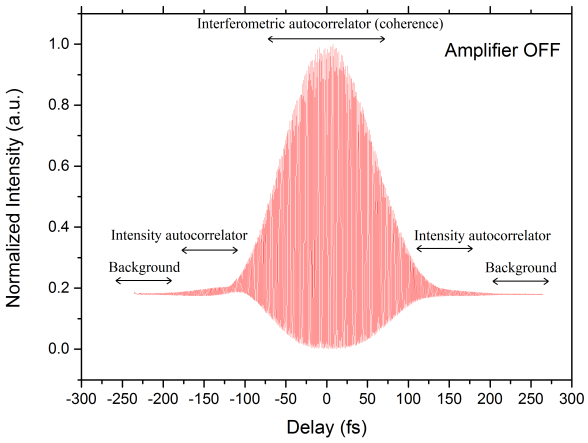

FIGURE 3.7: Autocorrelator function when the pump laser amplifier is switched off. The contributions of the signal (see eq.3.38) are shown.

The first acquisition is performed with the pump source amplifier switched off and the acquired signal is shown in Fig.3.7. Clearly the signal profile shows that phenomena such as chirping are absent since the signal profile is symmetric.

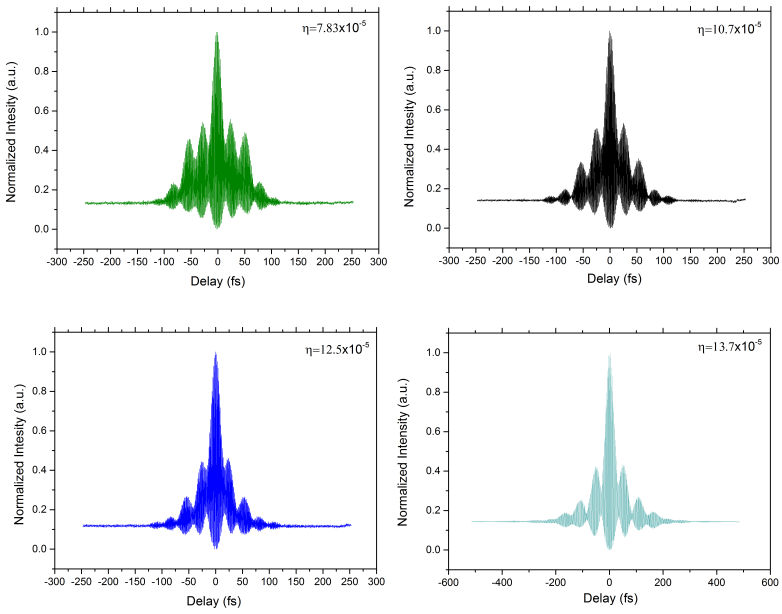

FIGURE 3.8: Sequence of autocorrelator function with the amplifier switched on, taken at different THz-generation efficiencies.

Differently, when the amplifier is switched on, the autocorrelator profiles show modulated structure due to the amplifier system. The reason is that

chirp effects are generated in the laser cavity. This means that the signal profile could change at different level of source power. For this reason, the autocorrelator signals are acquired at different THz-generation efficiency levels, as shown in Fig.3.8. More specifically, the efficiency of the process depends on the pump source, in this way, by changing the fs-laser parameters, the emitted THz power changes and the efficiency level is different.

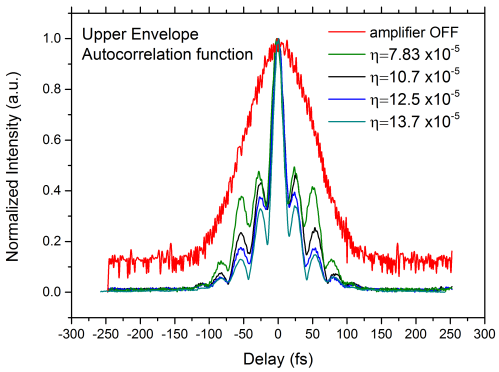

FIGURE 3.9: Upper envelope of the autocorrelator function for the configuration with the amplifier switched off and with the amplifier switched on at different THz generation efficiencies.

The profiles of the autocorrelator signals at different THz generation efficiencies are compared and reported in Fig.3.9. In order to easily compare the profiles, the upper envelope of the signals is reported. As expected, the narrower is the pulse, the more efficient results the generation process, according to eq.3.7.
The further step is the determination of the pulse temporal width. The estimation of the temporal width from the autocorrelator signal is not a trivial task especially when chirped effect are considered.
To this purpose, the temporal width can be approximately estimated with the following formula:

$$\tau = n\frac{\lambda}{2c\sqrt{2}} \tag{3.39}$$

where n is the number of fringes contained in the FWHM of the interferometric curve and λ is the wavelength of the laser.
In this way, the temporal width is measured and the results (τ) are reported in the table 3.1.

From this characterization, the fs-laser turns out to have a pulse with a temporal width of about 29 fs. Nevertheless, it is worth noting that the estimation of the temporal width has been performed with an approximately method as the chirp effect is present.

In order to complete the analysis, the previous data can be plotted in terms of the product of the temporal pulse width and generation efficiency of the non-linear process, that generates the THz-comb. The results are shown

TABLE 3.1: Measured temporal width at different THz-generation efficiency level.

Efficiency	n	τ (fs)
7.83 x 10^{-5}	16	29.41
10.7 x 10^{-5}	16	29.41
12.5 x 10^{-5}	15	27.65
13.1 x 10^{-5}	14	25.81

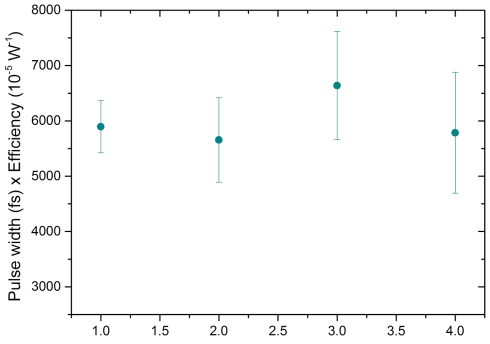

FIGURE 3.10: Product of the generation efficiency and temporal width of the data shown in Fig.3.8.

in Fig.3.10 and a constant trend is visible and compliant with the eq.3.7. Indeed, considering that:

$$\eta = \frac{P_{THz}}{P_{pump}^2} \prec \frac{1}{\tau f_{rep}} \tag{3.40}$$

the product of the generation efficiency and of the temporal pulse width is:

$$\eta\tau \prec \frac{1}{f_{rep}} \tag{3.41}$$

where the constant value is ensured by the fact that the repetition rate of the comb has been kept fixed during the measurements.

3.3.2 THz-FCS characterization

Once the pump source has been characterized and well aligned in the waveguide, the experiment concerns the extraction and optimization of the generated THz-comb. In the following, I will give details about the study and the measurement about the generated THz light.

Generation of THz light from Cherenkov emission

The non-linear medium used in this thesis is a $LiNbO_3$ crystal plate, fabricated by HC-Photonics company, with dimensions of $8 \times 10 \times 0.5mm^3$.

The surface of the crystal is equipped with a sequence of five linear MgO-doped waveguides obtained by ion implantation. The waveguides are oriented along the 10 mm-long side and their design has been optimized for single-mode propagation of 800 nm radiation, with an effective mode size of about 5μm diameter. The waveguides work also for the propagation of 1550nm radiation, as confirmed by the high fraction of light that can be coupled and by the value (52%) taken from the tabulated waveguide specifications.
According to the Cherenkov configuration, the crystal optical axis has been chosen parallel to the crystal surface and orthogonal to the waveguide input surface. This choice allows the maximization of the terahertz emission outgoing from the plate surfaces according to the relationship between the non-linear coefficient and the polarization of the pump.
Moreover, in order to efficiently extract the THz pulses, the crystal is coupled with a 45^o high resistivity float zone silicon prism. The Cherenkov emission is expected at an angle of 116^o with respect to the direction of the incoming field.

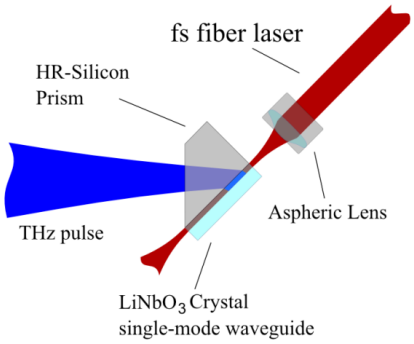

FIGURE 3.11: The fs laser is injected by an aspheric lens into the single-mode waveguide of the lithium niobate ($LiNb0_3$) crystal. The extraction of THz pulse is performed with a silicon prism.

The generated beam is composed of a series of pulse and each pulse consists of a single electric field cycle carring a large spectral content.

A conservative estimation of the spectral content is given by the spectrum (Fig.3.12) of the THz-comb generated in the same crystal but with a Ti:sapphire pump laser. This assumption can be assumed because the pump laser has a pulse temporal width similar to the Ti:sapphire laser pump, in this way their spectra can be supposed to be the same.
In addition, according to the theory of OR, the comb-like spectrum has a perfectly zero offset and a spacing corresponding to the 250MHz repetition rate of the pump laser. In the best conditions, the average power of the generated terahertz radiation is of the order of 14 μW, as measured with a calibrated pyroelectric detector placed in front of the silicon prism.

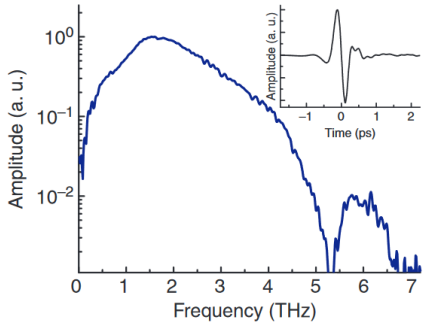

FIGURE 3.12: THz spectrum measured with the time-domain spectroscopy technique, using a photoconductive antenna as detector. The generation has been performed in a $LiNbO_3$ by using a femtosecond mode-locked Ti:sapphire laser at 800nm. Figure is reprinted from Ref. [66].

Improvement of the extraction of terahertz light

The THz light emitted by the crystal is divergent and very difficult to directly observe on a THz-camera (INO IRXCAM). To this purpose, a collection system has to be used to maximize as much as possible the detected light and a detailed analysis of the collection system has to be performed.
A system to collect THz light is placed along the direction of the Cherenkov emission and the beam shape is analysed with the THz-camera.
Initially, a parabolic off-axis mirror is used to collect the emitted beam and placed at about its focal length (25 mm) from the crystal. Then, the beam is focused on the THz-camera with another parabolic off-axis mirror.
Using this detection system, the beam section results stretched along the vertical plane. As a matter of fact, THz is generated by a fraction of the waveguide surface that is quite similar to a rectangular aperture, consequently the diffraction effect makes the beam astigmatic.

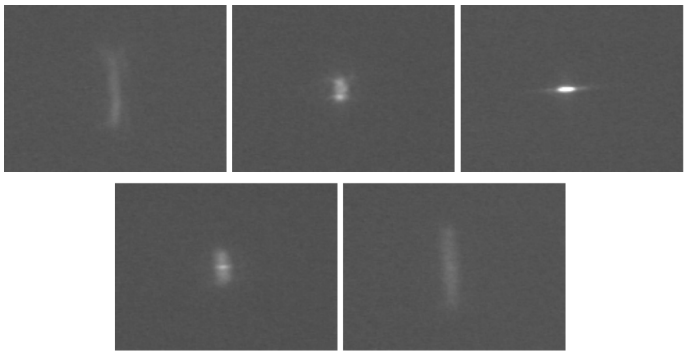

FIGURE 3.13: Sequences of THz beam sections at different focal length of the parabolic mirror. The signal is collected by a cylindrical mirror.

A more suitable way to collect the emitted light concerns the use of a cylindrical mirror. In this way, the beam is focused only in one direction (the direction in which the beam is stretched) and a higher power is measured since the light is well collected. The beam shape is shown in Fig.3.13 in a

sequence of images, taken at different focal distance from the crystal.
In this way, the collection of THz light has been optimized. The measured power is 15.3μW, detected by a power meter ($3A-P-THz$, Ophir Photonics), that is the highest value obtained.

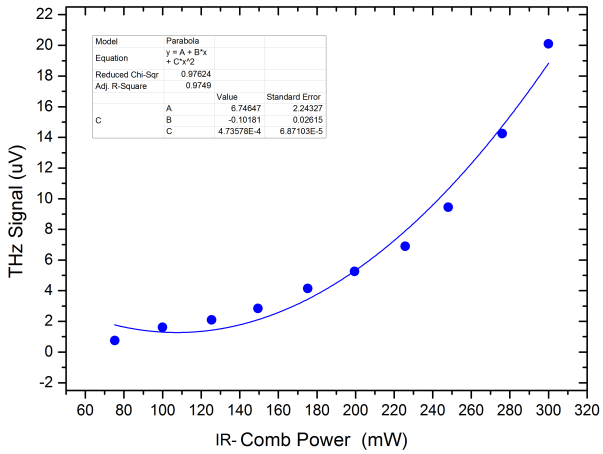

FIGURE 3.14: Generated THz signal versus IR-comb power.

A further optimization of the THz light, emitted by the crystal, can be done acting on the pump laser. The power of the pump pulse is slightly changed until the highest value of the THz power is measured.
A characterization of the THz power is performed and the data are shown in Fig.3.14. It is visible the quadratic dependence of the THz power on the power of the pump source, as expected for a second order non-linear process.
In conclusion, the results shown in this chapter give a clear knowledge of the THz and pump source, and about the physical process that governs the THz generation. In the following chapter applications of the generated THz comb are described.

Chapter 4

Exploration of QCL properties through beat-notes detection

This chapter focuses on the characterization and exploration of the properties of two different designs of QCL using the metrological grade system described in the previous chapter.
The characterization is performed through the detection of the beat-notes between the THz-comb and the THz QCL under analysis. This technique allows the measurement of the absolute frequency of the device emission with an uncertainty of a few parts in 10^{-10}. Furthermore, the detection of the beat-note is the first step for the phase-locking of the QCL to the THz comb. This allows to stabilize and control the QCL emission to perform high resolution spectroscopy.
The chapter is structured as follows. At first, the metrological system is presented with the description of the optical setup. Then, the method used to explore the QCLs characteristics and properties is presented.
The first characterized device has been set up by the group of M.Belkin at the Department of Electrical and Computer Engineering at the University of Texas in Austin. The device consists of a QCL based on intra-cavity difference-frequency generation. Its peculiarity concerns the capability to operate at nitrogen temperatures across the $1 - 6$ THz range. A full characterization of the device has been performed, including its emission frequency, tuning characteristics and emission linewidth. Exploring its spectral properties, the measured linewidth confirms its high potentiality as metrological tool for high-resolution spectroscopy at THz frequencies and as local oscillator for heterodyne detectors.
Afterwards, the chapter describes the second device, set up by the group of G.Scalari at the Institute of Quantum Electronics (ETH) in Zurich. The source is a broadband quantum cascade laser that can operate with a comb-like structure thanks to the non-linear process of four-wave mixing that takes place in its active region. As for the previous source, a complete characterization of the device emission has been performed. To confirm the true comb-like nature of such devices, preliminary studies of the coherence between the phases of different QCL modes have been performed.

4.1 Heterodyne metrological system

In order to explore the characteristics of the device emission, the beat-note signal arising from its beating with the THz-FCS is investigated.

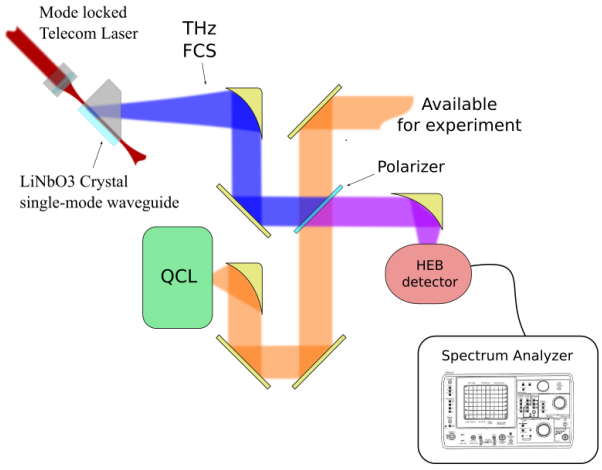

FIGURE 4.1: Experimental setup for the detection of the beat-note arising from the mixing between the QCL and the free standing THz FCS on a fast Hot Electron Bolometer (HEB) detector.

The experimental setup for the THz-FSC generation, described in Chapter 3, is upgraded to detect the optical beat-notes with a THz QCL (Fig.4.1). The fundamental element of the heterodyne system is a hot electron bolometer (Scontel model RS 0.3-3T-1) used as mixer to detect the beat-note between the QCL mode and a tooth of the THz comb (see 1.4).
Both the beams of the THz source and the THz comb are collected and collimated by a couple of 90^o off-axis parabolic mirrors with an equivalent focal length of 25.4 mm. The two beams are then combined on a THz beam splitter, and are sent to the HEB. The beam splitter is a wire-grid polarizer and its wires can be oriented in order to control the relative power of the two beams. The electrical signal from the HEB is sent to a fast Fourier transform real-time spectrum analyser (Tektronix RSA5106A) having a 40MHz real-time bandwidth. Since the THz comb repetition rate(f_{rep}) is very close to 250 MHz, any optical beat-note (OBN) signal can be analysed in a frequency window of 125 MHz band ($f_{rep}/2$), as described in the following section.

In other words, in order to detect the OBNs, a detector with a bandwidth of at least 125 MHz is required, therefore the electrical bandwidth of the detector is measured.
To this purpose, a strong signal of a beat-note is provided and observed on the spectrum analyser with the "max hold trace detector". The latter is useful to sweep frequency measurements and to acquire the history of peak values across the frequency axis, recording the maximum level the signal reaches. Indeed, the idea is to measure the signal to noise ratio (SNR) of the OBN at different OBN frequencies.
In order to sweep the OBN, the comb repetition rate is changed and the OBN

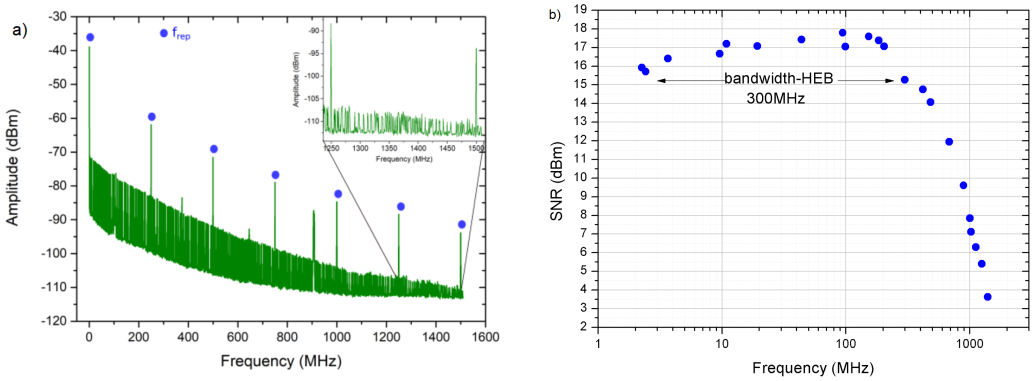

FIGURE 4.2: On the left: acquisition from the spectrum analyser (with the max hold trace detector) of the beat-note signal. The repetition rate of the THz comb is changed, and consequently the OBN slides towards right. On the right: measurement of the HEB bandwidth obtained by the data shown on the left.

shifts up to 1.5GHz, as shown in Fig.4.2 (a). In the graph, the OBN is shown for all the values of the repetition rate because of the max hold function.
Then, for each value of the repetition rate, the SNR of the OBN is measured and the electrical bandwidth is retrieved as the value at which the SNR is reduced of -3dBm (b). A bandwidth of 300 MHz is measured, ensuring the detection of the OBN.

4.1.1 Measurement of the absolute frequencies of QCL emission

The metrological grade THz FCS is used to measure the absolute frequencies of the QCL emission. The technique is described in the following.
When a CW, monochromatic source beats with a comb, several beat-notes are generated as a consequence of the beating with all the comb teeth.
For the sake of clarity, the condition under analysis is the beating of the source emission only with the two nearest teeth, one at lower frequencies and one at higher frequencies. Therefore, two optical beat-notes are generated with frequencies: $f_{b,1}$, smaller then $f_{rep}/2$ and $f_{b,2}$, in the range from $f_{rep}/2$ to f_{rep} (= 250MHz).
Considering the beating with all the other teeth of the OR-comb, the generated beanotes are a copy of the two previous ones. In other words, these beat-notes will have a frequency of $f_b = f_b + m_1 f_{rep}$ and $f_b = f_{b,2} + m_2 f_{rep}$ where m_1, m_2 are integer numbers that counts how many repetition rate are retrieved from the nearest tooth to the one that is actually beating with the QCL. The following description concerns with the measurement of the absolute frequencies of the source emission considering the beat-note in a frequency window ranging from 0 MHz to 125 MHz, that is the one labelled with $f_{b,1}$.
As said before, the detection system, made of the HEB and the spectrum analyser, ensures the detection of beat-notes in the frequency window until 300 MHz.

In order to identify the source emission frequency, its position with respect to the THz FCS tooth has to be determined. Indeed, the first step is to recognize if the source is beating with a tooth at lower or higher frequency.
This can be done by analysing the beat-note frequency swept when the THz-comb repetition rate is changed, as the only free parameter since the THz comb has a zero-offset. During this measurement, the temperature and the driving current of the source are stabilized to fix the spectral positions of the emission.
More specifically, the comb teeth are shifted by changing the repetition rate on a wide range. In fact, the accuracy on the absolute frequency of a mode is proportional to the width of the analysed frequency range.
In this way, the beat-note frequency evolution is observed analysing the direction of the shift (increasing or decreasing frequency) that is when the beat-notes slide left or right on the spectrum analyser.

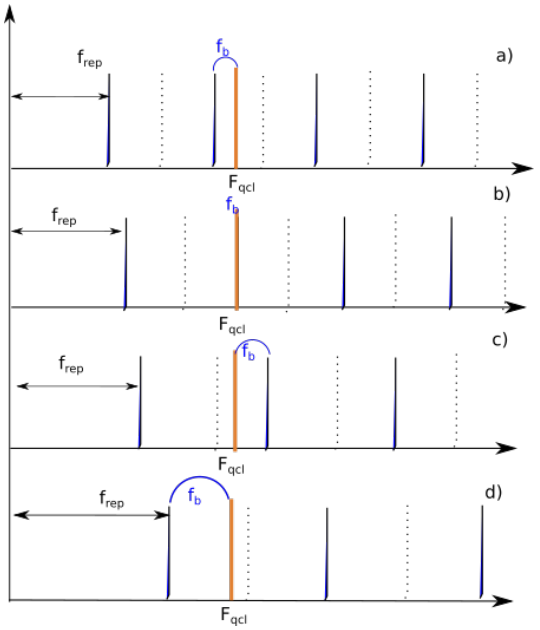

FIGURE 4.3: Schematic representation of the process used to retrieve the dependence of f_b on f_{rep} by measuring the beat-notes in the 0 to 125 MHz range.

A schematic representation, in the frequency domain, of the THz comb and a source emission, labelled with F_{qcl}, is shown in Fig.4.3.
In Fig.4.3 a), F_{qcl} is closer to the tooth at lower frequency and consequently its frequency is expressed as:

$$F_{qcl} = n * f_{rep} + f_b \tag{4.1}$$

Following the previous equation, the beat-note movement is analysed by keeping the laser modes fixed and by finely increasing the repetition rate. In this case, the beat-note f_b frequency decreases. If the repetition rate is progressively increased, Fig.4.3 b), the OBN f_b tends to zero. More specifically, one expects that, in the spectrum analyser window, f_b will slide towards lower frequencies, until it disappears when the tooth is at the same frequency of the mode. This happens when the mode frequency is exactly an

integer multiple of f_{rep} ($f_b = 0$ and $F_{qcl} = n * f_{rep}$).
By further increasing the repetition rate, F_{qcl} is always beating with the same tooth but now it is on the other side (Fig.4.3 (c)):

$$F_{qcl} = n * f_{rep} - f_b \tag{4.2}$$

Then, Fig.4.3 (d), the mode beats with the previous tooth ($n - 1$):

$$F_{qcl} = (n - 1) * f_{rep} + f_b \tag{4.3}$$

These equations allow to determine the absolute frequency of the QCL emission, following the procedure described below. It is worth noting that the same procedure could be adopted in the case of a tooth at higher frequency, by changing the sign of f_b.
The procedure to measure the absolute frequency of the source emission requires the identification of the THz-FCS tooth order (n) involved in the beating. In order to determine n, and therefore F_{qcl}, the experiment consists on the measurement of the linear frequency shift of the beat-note f_b while tuning the repetition rate f_{rep} of the THz FCS pump laser. For example, the repetition rate can be tuned in a range of approximately $\pm 0.4\%$ around 250 MHz (precisely, f_{rep} varies approximately from 249 to 251 MHz).
The spectral positions of the comb lines shift accordingly by as much as $\pm 0.4\%$, and the beat-note of the n_{th} comb mode with the laser line might change by as much as 20 GHz, largely exceeding the 300 MHz HEB detector electrical bandwidth.
Nevertheless, it is always possible to indirectly retrieve the frequency of this beat-note by observing the transition from the beat-note of the laser line with the n_{th} comb mode to the beat-note involving the $n-1$, $n-2$,...or $n+1$, $n+2$,... modes of the comb.
In this way, the variation of the beat-note frequency f_b between the THz-QCL line and the n_{th} mode of the THz FCS is obtained as a function of f_{rep}. The unknown index n was then determined by fitting the results with Eq.4.1 and rounding to the nearest integer. It is worth to note that the uncertainties in the fit parameters are reduced as the variation of f_{rep} increases; hence, the value of f_{rep} over the entire range possible in the FCS system is changed.

4.2 THz QCL based on intra-cavity difference frequency generation

The first characterized device is an intracavity difference-frequency generation quantum cascade lasers (THz DFG-QCLs). These kinds of sources, as discussed in Chapter 1, are expected to revolutionize THz research field. In fact, thanks to their properties such as the single-frequency operation with wide continuous tunability, narrow emission bandwidth, room temperature operation, this device is suitable for many applications. Among them it is worth mentioning high-resolution spectroscopy, the use as local oscillators for radio astronomy, THz sensing and imaging.

THz DFG-QCLs have demonstrated an extremely broad tuning range of nearly $1-6$ THz, and have achieved a dramatic improvement in output power that now exceeds 1 mW in pulsed mode and 10 μW in continuous-wave regime, at room temperature.

4.2.1 Details about the device

The device under analysis [84] has been set up by Prof.Belkin's group in the Department of Electrical and Computer Engineering at the University of Texas in Austin.
The QCL has been designed to select a high mid-IR pump frequency (ω_1) and a low pump frequency (ω_2) that, for a DFG process in the active region, results into a THz emission ($\omega_{THz} = \omega_1 - \omega_2$). In fact, the frequency separation between ω_1 and ω_2 has been chosen to provide THz emission at a required frequency.
The THz tuning can be achieved by changing mid-IR frequencies (ω_1 or ω_2): a small shift in mid-IR pump frequency translates into a large fractional change of THz emission frequency, leading to a wide tunability range.

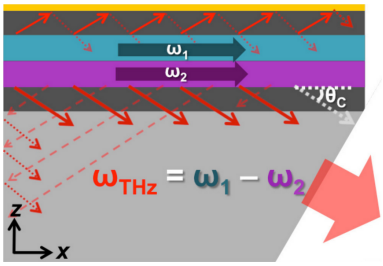

FIGURE 4.4: Schematic of Cherenkov THz DFG in the devices under analysis. Figure is reprinted from Ref. [84].

To indipendently control the two mid-IR frequencies, the device can be designed with two indipendently biased grating. In this case, the front section is designed with a grating to select high (ω_1) mid-IR pump frequency while the back section with a grating to select low (ω_2) pump frequency (Fig.4.4).
By applying an increase of DC bias current to the grating, only a red-shift of mid-IR frequencies can be induced while THz emission can be both blue or red shifted dependently on the choice of the mid-IR to tune.
The active region of the devices employed in this work is based on the bound-to-continuum active region design, designed to provide peak gain at $\lambda_1 = 8.5\mu$m and $\lambda_2 = 9.5\mu m$.
The laser band structure has been designed to have giant second-order optical nonlinearity, associated with intersubband transitions. The front facet of the laser bar substrate has been polished at 30^o for out-coupling of the THz Cherenkov DFG emission, while the back-device facet was covered with a high reflective coating. The laser bars have been mounted on a copper block and cooled in at liquid helium temperature in a cryostat.

4.2.2 Experimental characterization

The preliminary characterization of the DFG-QCL has been performed in the CNR-NANO in Pisa. After the characterization of the voltage-current and the light-current characteristics of mid-IR and THz outputs, the emission spectra have been acquired.
The measurement on the emissions of the two mid-IR pumps and the THz DFG emission from the device, have been performed using low resolution (3.75GHz) Fourier-transform infrared spectrometers (FTIRs).

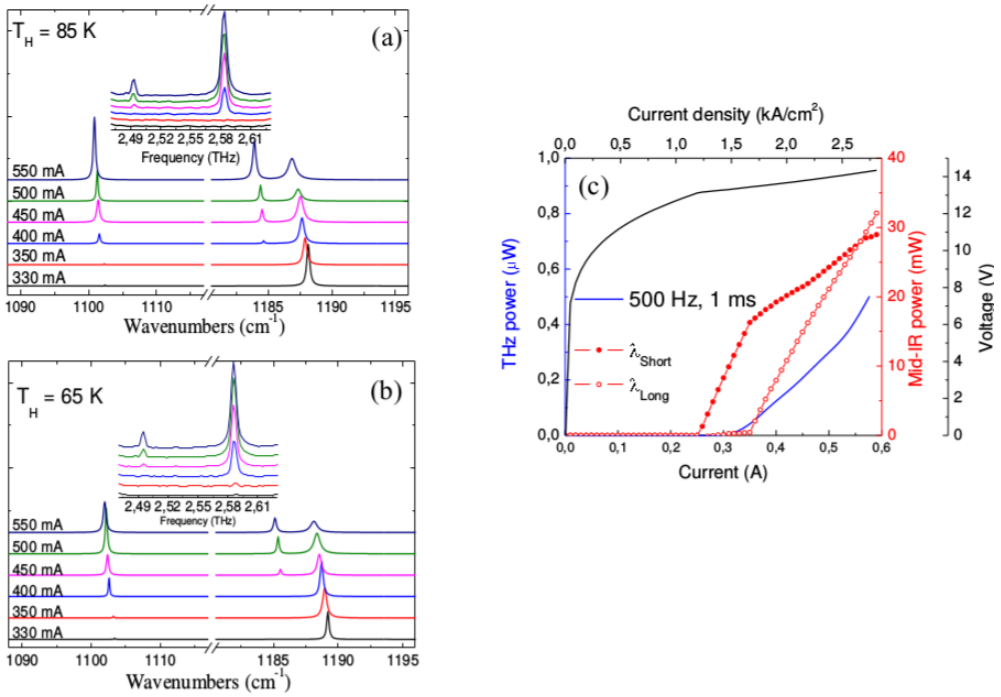

FIGURE 4.5: On the left: measured emission data of the THz DFG-QCL operated in CW mode at $T = 65K$ and $T = 85K$. On the right: voltage-current and light-current characteristics of mid-IR and THz outputs.

The measured emission spectra of the THz DFG-QCLs operated in CW at $T = 85$ K (a) and $T = 65$ K (b) are shown in Figure 4.5. The two values of temperature are the ones selected for this study.
More specifically, at low pump currents, this device emits a single THz frequency centred at approximately 2.58 THz. At pump currents above 450 mA, a second THz DFG emission line at 2.49 THz appears in the spectra.
Moreover, when the bias current is increased, a red shift in the frequency of the mid-IR pumps and for the THz difference-frequency is observed. This dependence is attributed to an increase of the active region temperature as the pump current increases. Finally, in Fig. 4.5 (c), the voltage-current and light-current characteristics of mid-IR and THz outputs are shown.

Then, the characterization consists on the determination of the temperature tuning. To this purpose, the emission spectra have been acquired at heat-sink temperatures (T_H) varied from 45 K to 200 K and the device is used in pulsed mode (400 ns pulses at 25 kHz repetition frequency). The spectral

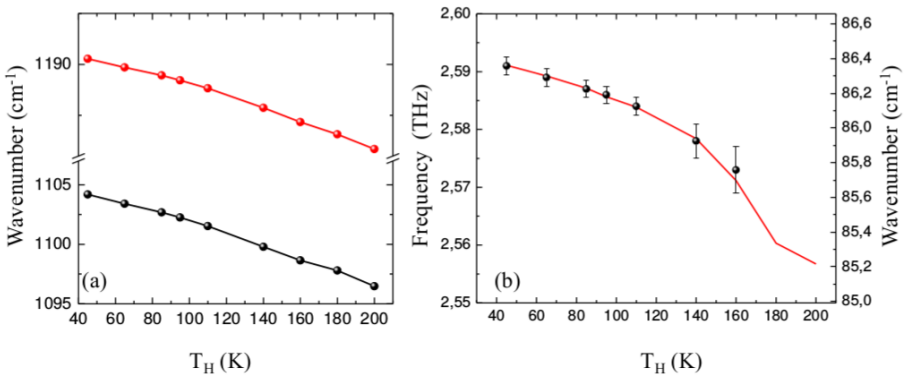

FIGURE 4.6: Dependence of mid-IR pump frequencies (A) and THz difference frequency (B) of the THz DFG-QCL on the temperature (T_H). The device was operated in pulsed mode, as described in the main text. The solid line in (B) represents the frequency difference of the two mid-IR peaks as extracted from (A), and the round symbols with error bars indicate the experimentally measured THz peak positions.

positions of the mid-IR pumps and the THz difference-frequency as a function of T_H are given in Fig.4.6.

4.2.3 Measurement of the absolute frequency

The two beat-note signals, corresponding to the two modes of the DFG-QCL are detected and their absolute frequencies are measured. The measurement is performed, for both mode independently, while driving the QCL at a current of 540 mA and a T_H of 75 K.
The absolute frequency of each of the two THz emission peaks in the spectra, shown in Fig.4.5, is determined and high-resolution studies of the dependence of the emission frequency on the DFG-QCL operating conditions are performed.

More specifically, the absolute frequency is determined with the method described in section 4.1.1 and summarized in the following.
In this case, the mode is beating with the right (higher-frequency) comb tooth, and the beat-note frequency (f_b) is given by:

$$f_b = n f_{rep} - f_{qcl} \tag{4.4}$$

where f_{QCL} is the THz DFG-QCL frequency, and n is the order of the closest THz FCS tooth involved. As already said, the first step is the identification of the order of the OR-comb tooth involved in the beating with the QCL mode. To this purpose, the repetition rate f_{rep} of the THz FCS pump laser is tuned from 249 MHz to 251 MHz. By changing f_{rep} and by measuring f_b, at a fixed value of f_{QCL}, the value of n can be retrieved by fitting of the data with eq.4.4, as shown in Fig.4.7.
By fitting the two different data sets (in Fig.4.7), n_1 and n_2 are determined rounding the value of the slope to the nearest integer. For the first mode, the

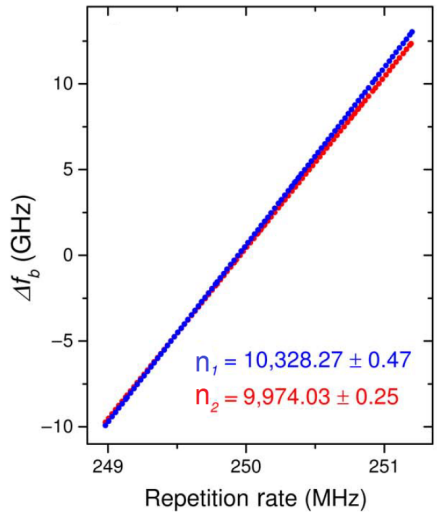

FIGURE 4.7: Measurement of the absolute frequencies of the two QCL modes.

fit returns the parameter $n_1 = 10,328.27(\pm 0.47)$, allowing the determination of the order of the comb tooth involved in the beating: $n_1 = 10,328$ (for the second mode, $n_2 = 9974$ is obtained).
Once n is determined, the same eq. 4.4 allows for the calculation of the absolute frequency of the free-running QCL from the measurement of f_b.
The value of nf_{rep} is known with an accuracy of the order of 100 Hz, whereas f_b is given by the centre frequency of the Gaussian fit with a 1 kHz uncertainty. The resulting relative accuracy on the QCL frequency is therefore on the order of $4x10^{-10}$. As an example, the absolute centre frequency of the first mode is $\nu_1 = 2,581,470,537(\pm 1)$ kHz. It is worth noting that the obtained uncertainties are much smaller than the spacing of the THz comb teeth. This allows to univocally determine the orders n_1 and n_2 of the comb teeth that are beating with the two modes, as confirmed by the errors on n that are smaller than unity.

4.2.4 Measurement of the current and temperature frequency tuning

The beat-note signal is given by the beating of the THz comb and the QCL emission under analysis. In this way, the detection of the beat-note signal allows to continuously follow the emission frequency of the THz QCL, while varying the QCL operational parameters.
In order to explore the DFG-QCL spectral properties, its current and its temperature are changed while fixing the THz FCS repetition rate. In fact, as the THz comb teeth are kept fixed through the stabilization of the repetition rate, all the variations in the beat-note frequency are related to variations of the QCL frequency.
Through these trends, the temperature and current tuning coefficients of the QCL are retrieved. The dependence of the frequency on the temperature device has been retrieved for the first THz mode by varying the temperature T_H in a range from 45K to 85K.

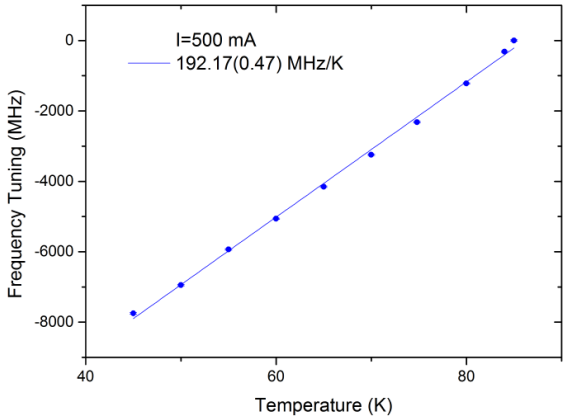

FIGURE 4.8: QCL frequency tuning as a function of the QCL temperature. The comb repetition rate and the QCL driving current have been kept fixed.

The emission frequency tunes with respect to temperature variations as shown in Fig. 4.8. The dependence is not exactly linear, but an average tuning coefficient of:

$$(+197.17 \pm 0.47)\ \ MHz/K \tag{4.5}$$

has been extrapolated by a linear fit.

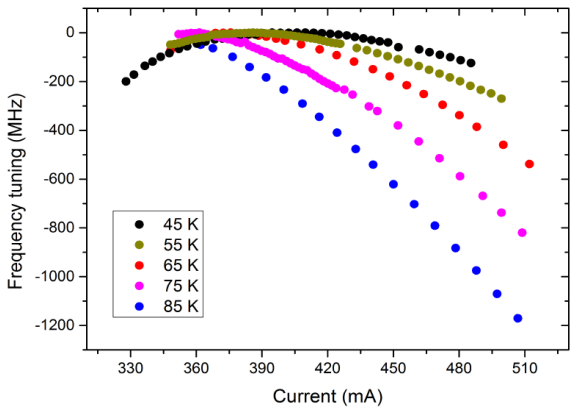

FIGURE 4.9: QCL frequency tuning as a function of the QCL driving current at different temperatures.

Then, the QCL current is changed while keeping constant its temperature and the repetition rate of the comb. The QCL frequency dependence on the driving current is shown in Figure 4.9.
When the device operates at a temperature $T_H = 45K$ and when the injection current is slightly above the laser threshold, the THz emission frequency initially blue-shifts with a tuning rate of about:

$$(+3.3 \pm 0.2)\ \ MHz/mA. \tag{4.6}$$

Then, a turning point is retrieved around 400 mA, and at higher currents the DFG-QCL frequency red-shifts with a tuning coefficient of approximately:

$$(-2.16 \pm 0.07)\ MHz/mA \tag{4.7}$$

This parabolic trend progressively disappears at lower temperatures as the "parabola" vertex shifts towards the laser threshold.
In fact, the inversion pointat 65 K is shifted towards lower currents. By further increasing T_H to 85 K, the data show a monotonic decrease in THz frequency with pump current with a slope of approximately $-6MHz/mA$.

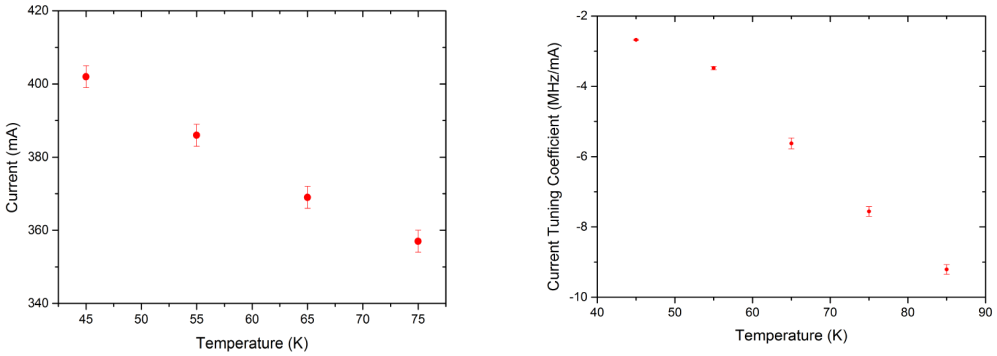

FIGURE 4.10: On the left: the "inversion points" of the parabolic current tuning trend in fig.4.9 are reported with respect to the device temperature. On the right: the red shift current tuning coefficients of fig.4.9 are reported with respect to the device temperature.

From the plot reported in Fig.4.9 information about the parabolic trend can be extracted (see Fig.4.10). The "inversion points" of the parabolic current tuning trend (Fig.4.9) are reported with respect to the device temperature. A linear dependence of the inversion point from the temperature emerges.
On the right of the Fig.4.10 the red shift current tuning coefficients are reported with respect to the device temperature and a linear trend is retrieved.

4.2.5 Spectral purity and tunability

In the previous analysis, described in section 4.2.3, the best evaluation of the line centre of the beat-note signal has been provided by fitting the signal with a Gaussian function that better describes the OBN profiles as shown in Fig.4.11.

At the same time, by the Gaussian fit other information on the QCL emission can be provided. For example, the FWHM of the Gaussian profiles represents an accurate estimation of emission linewidth of the device. To this purpose, the beat-note linewidth is assumed to represent the one of the QCL emission since the linewidth of the THz comb tooth involved in the beating process is negligible with respect to the QCL one, as demonstrated in [32], [66], [85], [86], [87].

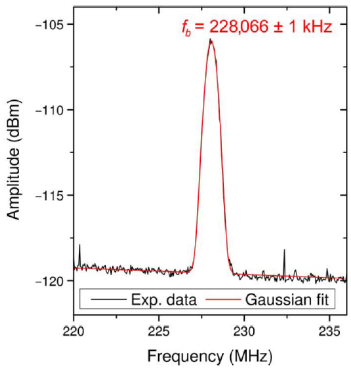

FIGURE 4.11: Typical beat-note signal (in black) and a fit with the Gaussian function (in red).

A very interesting study is the analysis of the linewidth as function of the observation time. Indeed, different time scales (ranging from 1ms to few seconds) can be changed in the acquisition mode of the FFT spectrum analyser. At first, the analysis has been performed at different QCL driving current to retrieve possible dependence of the QCL spectral properties on its operational parameters.

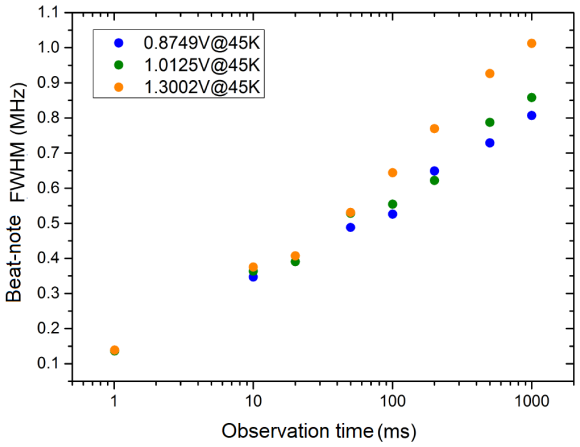

FIGURE 4.12: Width of the beat-note at different time scales and for different driving current/temperature values.

More specifically, the emission linewidth of the 2.58 THz emission line of the device has been measured at 45K for three different values of the QCL driving current.
The results are reported in Fig.4.12 where each experimental point is a result of a statistic of about ten measurements. The emission linewidth in the three experimental conditions does not show any significant difference.

To better explore the spectral properties, a comparison at different temperatures (45K and the one at 78K) is reported in Fig.4.13 (A). From this comparison, many information can be retrieved, and the spectral noise has been calculated, shown on the right of the same figure (B). The laser was operated with a pump current of 450 mA for both measurements by using an ultra-low noise current driver (ppqSensemodel QubeCL05). The range of analysis

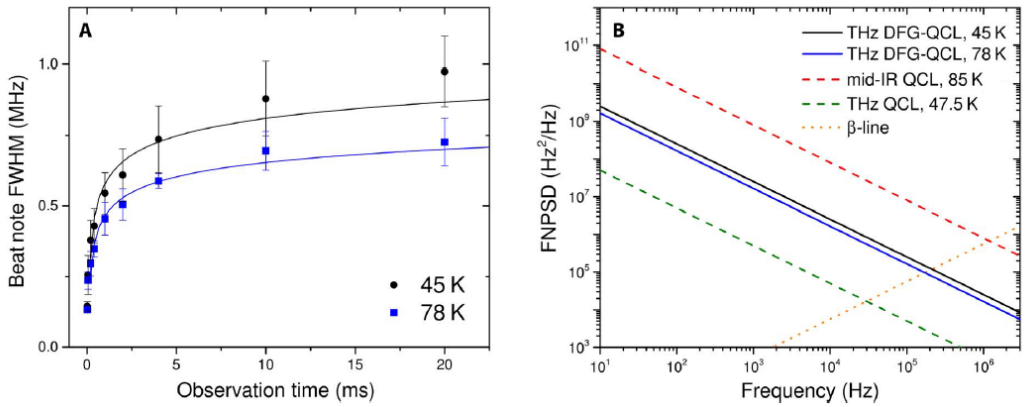

FIGURE 4.13: (A) Width of the beat-note at different time scales measured at two different operating temperatures of the device. Solid lines are fits with a logarithmic function. (B) Reconstruction of the FNPSD of the THz DFG-QCL emission. The dashed red and green lines refer to the measurements performed by Bartalini et al. [17] and Vitiello et al. [31] for the mid-IR and THz QCLs, respectively, whereas the solid lines refer to the measurements presented in this work.

is limited at short time scales at 20 ms, corresponding to the acquisition time of the single FFT spectrum in which the beat-note width starts to be limited by the resolution bandwidth of the instrument (in this case, 100 kHz). At this time scale, an upper limit of the QCL LW of 125 kHz is measured.
First, the data show that the LW of THz emission from the device is reduced as the operating temperature increases. This is consistent with the previously observed narrowing of the emission LW of mid-IR QCLs at higher temperatures [17] [88].
Moreover, the LW has a logarithmic dependence on the time. This indicates the presence of a $1/f$ noise component in the frequency noise spectrum between 1 Hz and 1 kHz that likely comes from the typical "pink" frequency noise of the mid-IR pumps of the DFG-QCLs. This is also confirmed by the noise decrease at increasing temperatures, in agreement with previous experiments on the $1/f$ noise of mid-IR QCLs that showed a similar trend [17], [89], [90].
A quantitative comparison with previous LW measurement reports of mid-IR QCLs can help in understanding the possible correlations between the emission LW of the mid-IR pumps and the THz emission LW. To this purpose, the inverse method proposed by Di Domenico et al. [91] has been applied to the data in Fig.4.13 (A) to retrieve the frequency noise power spectral density (FNPSD) of the devices (B).
The method described by Di Domenico et al. is summarized in the following. The LW of any laser source over a given observation time t_0 from its FNPSD $(S(f))$ is retrieved in a simplified method. In fact, assuming a monotonic trend for the FNPSD, the laser LW $d\nu(t_0)$ (FWHM) is recovered by a simple integration of $S(f)$:

$$\delta\nu(\tau_o) = \sqrt{8ln2 \int_{f_0}^{f_1} S(f)df} \tag{4.8}$$

In this equation $f_0 = 1/t_0$, while f_l is defined as the frequency at which the FNPSD crosses the so-called β-separation line:

$$S(f_1) = \frac{8ln2}{\pi^2} f_1 \tag{4.9}$$

The procedure well approximates the true value only if the following condition is fulfilled

$$S(f_0) > \frac{8ln2}{\pi^2} f_0 \tag{4.10}$$

Assuming that in the explored frequency range (10 Hz to 10 kHz), the FNPSD of the laser has a flicker-type origin, that is $S(f) = A/f$. Eq.4.9 gives a logarithmic-type function that can be used to fit the experimental values $d\nu(t_0)$ of the laser LW at different time scales (Fig. 4.13), thus allow to determine the parameter A.
With this method, the graph on the right of figure 4.13 (B) can be checked. The crossing point with the β-separation line falls above 10 kHz, which validates the model assumptions for the explored frequency range of 10 Hz to 10 kHz.
Figure 4.13 (B) shows the two flicker-type functions that reproduce, via Eq. 4.8, the experimental LWs of the device operated at 45 and 78 K, together with the two flicker-type functions that directly fit the experimental FNPSDs measured from a mid-IR QCL operating at 85 K [17] and a THz QCL operating at 47.5 K [31].
The plot shows that the FNPSD of the DFG-QCL, even in the upper edge of the investigated temperature range (T_H = 45 to 85 K), is almost one order of magnitude lower than that of the mid-IR QCL. The reduction in the emission LW of THz DFG can be explained by the correlation between the phase/frequency noises of the two mid-IR pumps of our device that are, in part, compensated by the DFG process.
On the other hand, the FNPSD of a single-mode bound-to-continuum THz QCL exploiting a single plasmon waveguide shows a significantly narrower LW (by approximately a factor of 7). Nevertheless, the reported measurements indicate that the LW of THz DFG-QCLs is already suitable for heterodyne THz detection, and it is expected that it can be further reduced with frequency/phase stabilization. Note that no significant dependence of the LW on the driving current is evident.
In conclusion, the THz emission of the THz DFG-QCLs has a linewidth of few hundreds kHz over a 1ms observation timescale. Peculiar current and temperature tuning characteristics have been characterized and an evidence of frequency noise cancellation of the mid-IR pumps in the THz output has been provided.

4.3 Four-wave mixing THz QCLs

The second device characterized in this thesis is a four-wave mixing terahertz quantum cascade laser (THz FWM-QCL) which is a continuous-wave multimode broadband source. The device has been manufactured at the Institute of Quantum Electronics (ETH) in Zurich by G.Scalari's group.
This kind of QCL is very promising for metrological-grade applications, such as high precision spectroscopy. The aim of the studies is to demonstrate that these devices show a comb-like emission regime with up to 600 GHz spectral coverage.
In the following sections, results about the spectral characterization of the THz FWM-QCL are reported. I will describe the measurement of the absolute frequencies of the QCL modes, performed with the heterodyne system presented in section 4.1. Then, I will describe the acquisition and analysis of the electrical intermodal beat-note (IBN) between the QCL-modes.
The following studies focus on the study of the QCL emission that has a true comb-like feature. Indeed, in analogy with conventional OFCSs, parameterized by the "offset" and "repetition rate", the QCL can be parametrized in the same way with the two parameters "offset" and "spacing". More specifically, the "spacing" is measured through the intermodal beat-note (IBN) and the dependence of offset and IBN from operational parameters (such as driving current) has been characterized.
For this reason, it would be very important to completely control this kind of device, through variation of the two typical comb quantities. To this purpose, two independent actuators have to be found to lock both its IBN and its offset. Detailed studies about two possible actuators are described here.
In the last part of the experiment, the frequency of an optical beat-note (OBN) has been subtracted to the other OBNs in order to remove the offset contribution. In this configuration, the phase coherence between the QCL modes has been directly observed and characterized. The measurement has been performed by stabilizing the QCL-IBN to a microwave local oscillator.

4.3.1 Details about the device

The QCL has been fabricated with a design based on a broadband active region. In this case, the very short upper state lifetime is responsible for a very broadband four-wave mixing process.
More specifically, the process of non-linear mixing is based on the resonant excitation of the large $\chi^{(3)}$ of the laser intersubband transition. This effect, together with the rather broad gain curve of QCLs, leads to typical lasing bandwidths of a few THz and of a few hundreds of GHz in the mid-IR and THz ranges respectively.

The process can be explained in the following way, as described in [92]. In the case of non-degenerate four-wave mixing the importance of a short τ_{NR} can be seen from the scheme of Fig.4.14 where the process has been sketched in two consecutive steps.
Initially, through laser induced saturation, the population inversion (hence

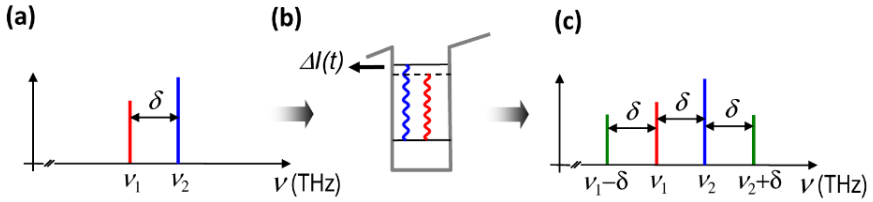

FIGURE 4.14: The resonant non-degenerate four-wave mixing is sketched. (a) Initial mode frequencies, ν_1 and ν_2, separated by δ. (b) Resonant non-linear mixing of the two photons at ν_1 and ν_2 (wavy red and black lines). The electronic potential profile (in grey) confines the upper and lower laser levels, represented by the horizontal black lines. (c) Final frequencies resulting from four-wave mixing, with the two sidebands at $\nu_1 - \delta$ and $\nu_2 + \delta$ (in green). Figure is reprinted from Ref. [92].

the gain) is modulated at the different frequency between two neighboring modes at ν_1 and ν_2. This modulation will subsequently produce two sidebands around each original mode frequency at $\nu_1 + \delta = \nu_2$, $\nu_1 - \delta = 2\nu_1 - \nu_2$ and $\nu_2 + \delta = 2\nu_2 - \nu_1$, $\nu_2 - \delta = \nu_1$.

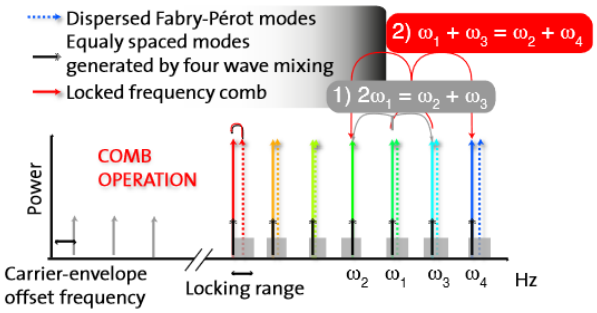

FIGURE 4.15: Schematic of the operation of the FWM-QCL. Figure is reprinted from Ref. [93].

This mechanism is expected in broadband QCLs with low group velocity dispersion (GVD) where the frequency comb operation is achieved by using four-wave-mixing as a phase-locking mechanism. In fact, the ability of four-wave mixing to generate mode proliferation — and ultimately comb operation — depends critically on the group velocity dispersion of the cavity, as described in [93].
Degenerate and non-degenerate four-wave mixing processes lead a proliferation of modes over the entire laser spectrum. The dispersed Fabry-Pérot modes – which are present in the case of a free-running multimode laser and are not phase-locked – are then injection-locked by the modes generated by the FWM process, thus creating a comb-like structure (Fig.4.15).
A device with a comb-like structure in its emission can be parameterized by the two typical comb quantities: "offset" and "spacing". More specifically, the offset is defined as the frequency of the first mode while the "spacing" is the frequency separation between the modes, i.e. the intermodal beat-note (IBN). In fact, in this case, the device has a comb-like regime and the modes are equally separated.

Additionally, these devices suffer from the general drawbacks of THz QCLs: operation is limited to cryogenic temperatures. For this reason, the laser is soldered to a copper bar, wire bonded and mounted on the cold finger of a liquid helium cryostat.

4.3.2 Experimental characterization

The preliminary characterization of the device, concerning the electrical and the optical spectrum, has been provided by the ETH group. These results are shortly reported in the following since these are useful indication about the laser operation.

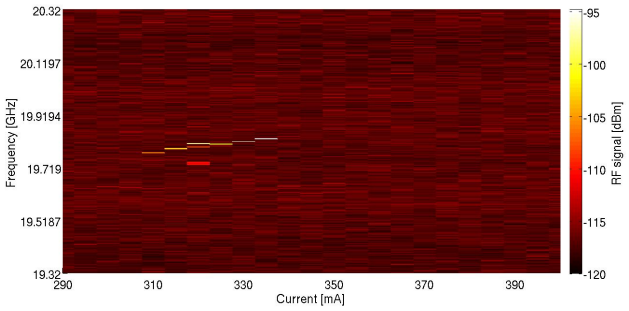

FIGURE 4.16: Evolution of the electrical beat-note spectra as function of bias current.

A complete colour scale intensity mapping of the IBN spectra as function of bias current is shown in Fig.4.16. In the spectra, the intermodal beat-note power is displayed in dBm. The electrical intermode beat-note mapping identifies the driving current at which a comb-like regime can be achieved.
As described before, this kind of QCL has a broadband emission. When the device does not work in the comb-like regime, the modes are not equally separated and the electrical intermodal beat-note progressively broadens as the emission bandwidth covers a wider spectral region. For istance, looking at the previous graph, this condition is achieved around 320mA where several peaks are visible.
Differently, when the injection-locking of the QCL modes is achieved, the modes are equally spaced. In this case, the beat-note collapse is a clear indication that the laser is operating in a comb-like regime. Throughout this entire region a very narrow beat-note is observed at a current of 310mA where the IBN is 19.7 GHz. Moreover, the IBN value can be theoretically estimated considering that the spacing is exactly the free spectral range ($FSR = c/2nL$) of the laser cavity. In this case, the laser bar has a length of $L = 2$ mm and the refraction index of the active region, which is a semiconductor, is $n = 3.8$. Consequently, the IBN results 19.7 GHz according with the spectra.

The emission spectrum is the second set of measurements provided by ETH. The comb-like regime is also revealed in the emission spectrum of the QCL at the temperature of 20K and for a current of 310mA, shown in Fig.4.17 that clearly shows a broadband emission.

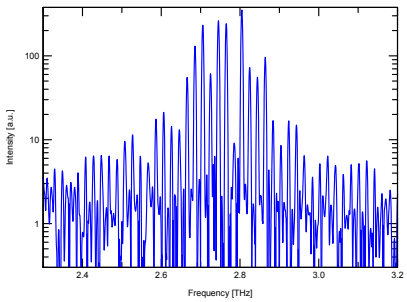

FIGURE 4.17: Spectral performance at the temperature of 20K and current of 310 mA.

In order to proceed with the characterization of the QCL operation, the experimental setup has been arranged to simultaneously detect both the IBN and the beatnote signals with the FCS.
The optical beat-notes, generated with the FCS, are useful to characterize the THz emission. Indeed, these ones are detected with the heterodyne system shown in Fig.4.1.
On the other hand, the IBN, which is an electrical RF-signal, is detected with a bias-tee installed very close to the QCL device, ensuring a good SNR.

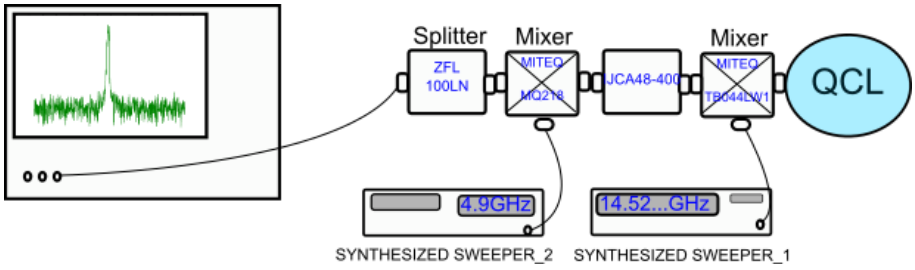

FIGURE 4.18: Electrical setup used for the detection of the IBN.

The IBN is down converted to MHz frequencies in order to be simultaneously observed with the optical beat-notes on the same spectrum analyser. Moreover, the spectrum analyser used in this work, has a frequency bandwidth of 6 GHz, smaller than the 19.7 GHz of the IBN, so the RF signal of the IBN needs to be down-converted (Fig.4.18). Therefore, the signal at 19.7 GHz has been mixed with a 14.6 GHz signal and then, the resulting signal has been mixed with a 5 GHz signal obtaining a final signal at about 100 MHz.

4.3.3 Measurement of the absolute frequencies of QCL modes, intermodal beat-note and offset

The first part of the experiment concerns the measurement of the absolute frequencies of the QCL modes. Thereafter, this set of emitted frequencies is parameterized using only the intermodal beat-note and the offset.
Looking at the absolute measurement of the QCL modes, a simple setup (shown in Fig.4.1) and a commercial HEB detector are used to directly observe the beat-note between individual comb teeth and a small fraction of

the terahertz QCL emission. The QCL is housed in a liquid helium cryostat, and driven in continuous-wave mode at fixed heat sink temperature $T_0 = 20$ K and at a current of $I = 310$ mA. These are the working conditions of the comb-like regime, as indicated by ETH characterization (Fig. 4.17).
More specifically, the emission is analysed in a configuration in which the strongest beat-note signals are observed in a span of 40 MHz.

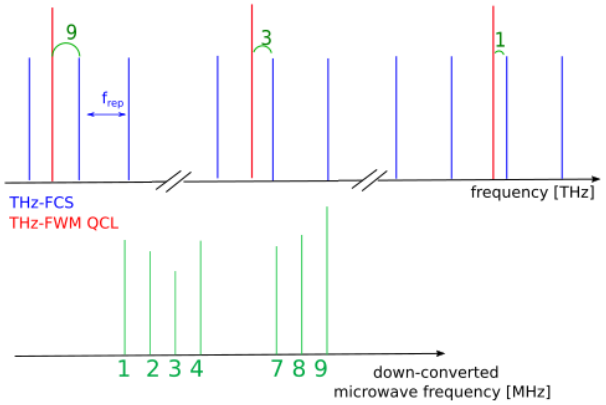

FIGURE 4.19: Sketch of the beating (in green) between the OR-comb (in blue) and the QCL modes (in red).

In fact, tuning the comb-OR repetition rate a condition in which the spacing is an integer multiple of the THz-FCS repetition rate can be found. In this condition the train of "optical" beatings collapse into one frequency. Starting from this condition, by slightly determining the THz-FCS f_{rep}, it is possible to remove the degeneracy of the OBNs and to resolve them one by one in a small frequency span (40 MHz= real-time bandwidth of the spectrum analyser). For the sake of clarity, the OBNs have been labelled with a numeric progression considering that the OBN, indicated with the number "1", has the highest frequency, as shown in Fig.4.19.

Absolute frequencies

In the comb-like regime, the seven strongest optical beat-note signals are detected and used for the spectral characterization of the device.

The seven OBNs are shown in Fig.4.20. As said before, the acquisition has been performed by changing the repetition rate of the comb OR to have the OBNs in 40MHz of span.
It is worth noting that the configuration of the OBNs changes with the QCL working condition and with its alignment. Indeed, during the daily alignment procedure, useful to optimize the signal/noise ratio, the OBNs change in their relative amplitude. In addition, some OBNs can disappear and new ones can appear because the different modes are not uniformly distributed in the QCL spatial emission.
The operational parameters of the device are the same of Fig.4.17. By the comparison with Fig. 4.20, the emission spectrum seems to be centred in a range from 2.70THz to 2.90THz since the strongest OBNs are detected.

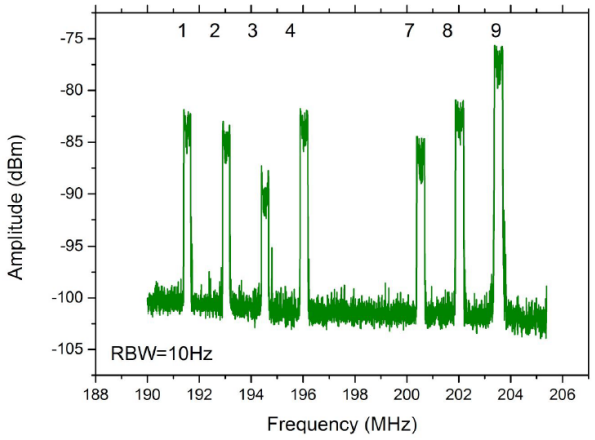

FIGURE 4.20: Optical beat-notes between the QCL-modes and the OR-comb. The acquisition has been performed by changing the repetition rate of the comb OR to have the OBNs in 40MHz of span.

Thereafter, the absolute frequencies of the OBNs are measured with the method described in section 4.1.1. To this purpose, the THz comb repetition rate is finely tuned and the beat-note frequencies change. In this way, from the direction of the movement (increasing or decreasing frequency) one can understand whether the QCL mode is beating with a tooth at higher or lower frequency.

The evolution of the beat-notes is observed increasing the repetition rate, as shown in Fig.4.21.

More specifically, referring to fig.4.21(a) seven QCL modes are observed. The modes beat with seven different THz comb teeth all on their right since the beat-notes move towards higher frequencies when increasing f_{rep}. Increasing the repetition rate, the beat-notes tends to move close together until they superimpose (b). In this case, the QCL modes are equally spaced from the tooth of the comb OR. By further increasing the repetition rate, the beat-notes spread out again inverting their order (c). The reason is that the modes beat with a different side of different teeth.

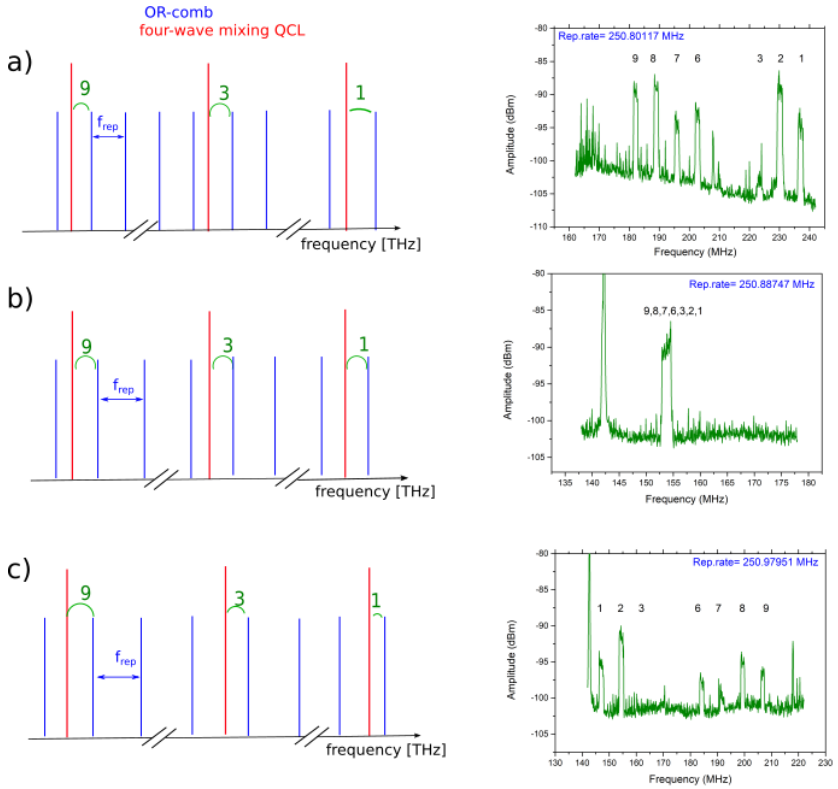

FIGURE 4.21: On the left: sketch of the beating (in green) between the OR-comb (in blue) and the QCL modes (in red). On the right: evolution of the beat-note frequency when the OR-comb repetition rate is increased.

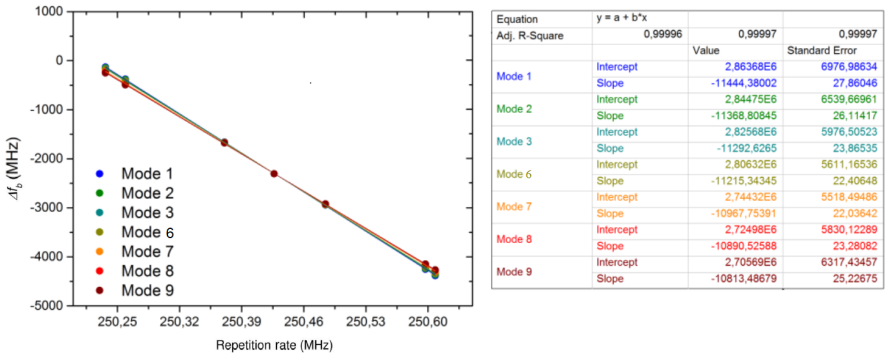

FIGURE 4.22: Measurement of the emission frequency of the seven QCL-modes at different OR-comb repetition rate.

TABLE 4.1: The absolute frequencies, and the respective uncertainty, of the QCL modes are reported. The label identifies the modes shown in Fig.4.20.

Label	f(THz)	Δf (MHz)
1	2.8636	6976
2	2.8485	6539
3	2.8294	5976
6	2.8101	5811
7	2.7481	5518
8	2.7248	5830
9	2.7094	6317

Once the position of the THz emission with respect to the THz FCS tooth has been determined, the order of the comb tooth involved in the beating has to be retrieved.
To this purpose, the repetition rate of the THz FCS pump laser is tuned from 250.25 MHz to 250.60 MHz. By measuring f_b for each mode, at a fixed value of f_{QCL}, the value of n can be retrieved by fitting the results in Fig.4.22 and rounding to the nearest integer.
In this way, for each mode, n is determined from the measurement of the beat-note frequency. Then, it is possible to retrieve back the instantaneous absolute frequency of the free-running QCL with Eq.4.2. The absolute frequencies at the emission modes are reported in table 4.1.
As a matter of fact, the errors that affect the beat-note signals can derive both from QCL or comb frequency oscillations. Otherwise f_{rep} of the THz comb is known at sub-Hz level, and it is phase-locked to the primary frequency standard. As a consequence, the instabilities of the QCL mode frequencies can be observed and measured directly from the corresponding beat-note signals. One should be able to distinguish between QCL offset drift that rigidly moves all the beat-note signals at the same time, and QCL spacing oscillations that makes the OBNs shifts proportional to their order.

Determination of the QCL comb parameter: the intermodal beat-note

As described before, the QCL has a broadband emission with optical modes equally separated of about 19.7GHz. The measurement of the radio-frequency spectrum of the laser emission, i.e. the intermodal beat-note (f_{IBN}), is fundamental to complete the spectral characterization of the device.
A very precise measurement can be performed directly through the spectrum analyser. Nevertheless, the RF-signal has been down-converted with two mixing steps, as shown in Fig.4.18. Therefore, the exact value is retrieved by considering the frequencies of the two synthesizers:

$$f_1 = 14.781236016\, GHz \qquad f_2 = 4.900467102\, GHz \tag{4.11}$$

Considering that the measured down-converted frequency is around 99.75 MHz, the intermodal beatnote is:

$$f_{IBN} = 19.781453118\, GHz \tag{4.12}$$

which matches perfectly with the value indicated in Fig. 4.16.

Determination of the QCL comb parameter: the offset

To complete the spectral characterization of the device, information about the offset can be retrieved by a simultaneous analysis of IBN and OBNs. In this way, a complete knowledge of the device is obtained.
At first, each QCL mode can be identified with the parameter N which is the order of the QCL modes, easily obtained by the ratio f/f_{IBN}, where f is the absolute emission frequency of the mode under analysis. Then, the ratio is rounded up and its rest (f_{abs} Mod $[f_{IBN}]$) gives the value of the QCL offset.

This estimation can be made if the uncertainty on the absolute frequency is less than the IBN, as already verified in the previous measurements.

TABLE 4.2: Overview of the absolute frequency of each mode. The error in the determination of the frequency (Δf), the number of the mode and the retrieved offset value are reported.

f(THz)	Δf (MHz)	$N = f/f_{IBN}$	$f_{off} = f_{abs}$ Mod $[f_{IBN}]$ (MHz)
2.8636	6976	145	-4630.70
2.8485	6539	144	-3776.24
2.8294	5976	143	-3067.79
2.8101	5811	141	-3646.34
2.7481	5518	139	-5301.98
2.7248	5830	138	-4960.53
2.7094	6317	137	-4379.07

In absence of errors, for each mode the same value of the offset has been obtained. However, different values are retrieved due to the statistical error in the determination of the absolute frequencies (Δf).
The obtained values are shown in table 4.2 where the minus sign is according to the choice of rounding up the ratio $N = f/f_{rep}$.
Finally, the offset results -4251.81MHz, obtained as the average of the retrieved values for each mode.

4.3.4 Actuators for controlling the QCL parameters: current, visible light and temperature

It would be very important to completely control this kind of device, through variation of its two parameters: spacing and offset. To this purpose, two independently actuators are required.
A first natural candidate is the QCL driving current, from which the frequency emission depends. In the same way, also the temperature could be used as actuator. Nevertheless, the latter is excluded because the stabilization in temperature is very slow and could not ensure an efficient control with kHz bandwidth (at least).
The second natural candidate is the visible light. In fact, during the alignment step, it has been observed that the optical beat-notes were shifted for an external modulation at 100 Hz coming from the lab lights.
The idea is to use both the visible light and the QCL current as actuators to lock both the spacing and offset. This task can be realized if the two actuators act in different way on the two parameters. In other words, the complete control could be obtained if one actuator acts on the spacing and the other one on the offset.
Therefore, as a first step, the orthogonal condition between the two actuators has to be verified and preliminary characterization is required.
To this purpose, it has been measured how the modulation by the visible light and current acts on both the optical and intermodal beatnote. For this preliminary characterization only one optical beat-note is analysed. The one

selected is the OBN, previously labelled with the number "9".
Looking at the first actuator, which is the visible light, the measurements are performed with a white LED, mounted in front of the cryostat window.
The LED intensity is modulated and the frequency shift amplitude of the OBN and IBN is acquired at different LED modulating frequencies.

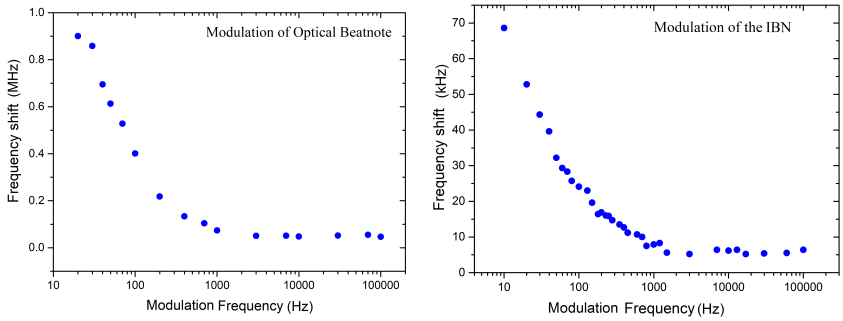

FIGURE 4.23: The LED modulation is applied. On the left: frequency shift of the optical beat-note, labelled with n.9. On the right: frequency shift of the IBN.

The results are shown in figure 4.23 for both the optical (on the left) and the intermodal (on the right) beat-note. In the two graphs the same trend is observed and the frequency (called "cut-off") at which the signal is reduced of 3 dB, is about 100 Hz.
To understand the origin of the cut-off frequency, the LED is independently characterized at the same working condition of the previous measurement.

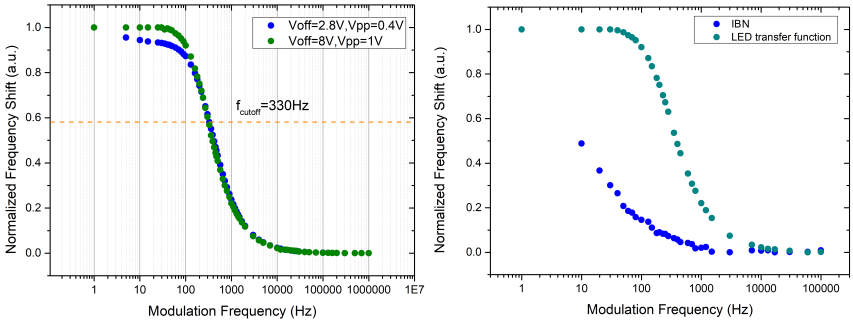

FIGURE 4.24: On the left: LED cut-off frequency measurement. On the right: comparison of the LED cut-off frequency measurement with the frequency shift of the electrical beat-note, shown in Fig.4.23.

The LED is biased by a power supply with an output signal as sinusoidal wave with a peak to peak voltage of 1 V, and an offset of 8 V. At this working condition, the LED transfer function is measured and compared with a different working condition to observe possible differences. The results are shown in Fig.4.24 together with the comparison with the graph shown in Fig.4.23.
From this characterization, it can be noted that the effect of the light modulation of the QCL frequencies is quite slow. A first hypothesis, to be confirmed, is the thermal effect of the light heating on the device.
Looking at the second actuator, the QCL driving current, the measurement is performed by applying a sinusoidal wave to the QCL power supply. The

IBN and the OBN are observed by acquiring their frequency shift amplitude, caused by the current modulation, at different modulating frequencies.

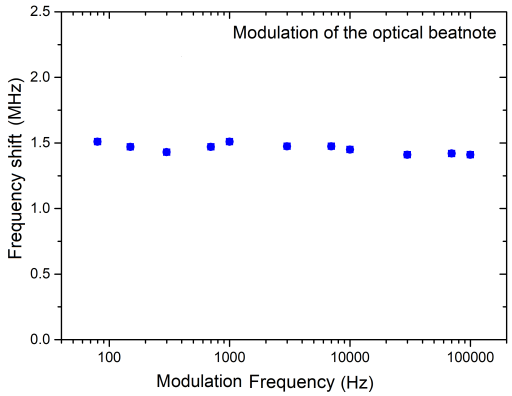

FIGURE 4.25: Current modulation on. Measurement of the frequency shift amplitude of the optical beat-note at different frequencies modulation. The optical beat-note is the one labelled with number 9.

The same trend for both the IBN and the OBN (shown in Fig.4.25) is obtained. Differently from the LED actuator, the current has a wide bandwidth enough to use it as actuator for the phase-locking of the OBNs.

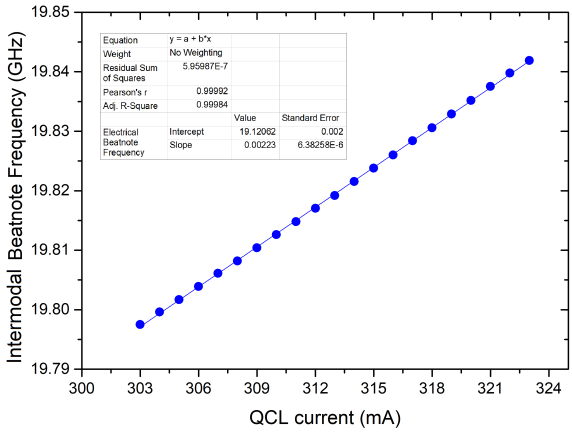

FIGURE 4.26: IBN frequency at different QCL driving current. The tuning coefficient is retrieved by a linear fit.

Finally, the IBN current tuning coefficient is measured. To this purpose, the IBN centre frequency is acquired at different current modulating frequencies, as shown in Fig.4.26. From a linear fit of these data, a tuning coefficient of 2.2 MHz/mA is obtained.

Temperature tuning characterization

In order to have a more complete knowledge of the device, the QCL temperature tuning coefficient is measured. Nevertheless, this measurement can be a proof about the LED effect, supposed to be thermal.

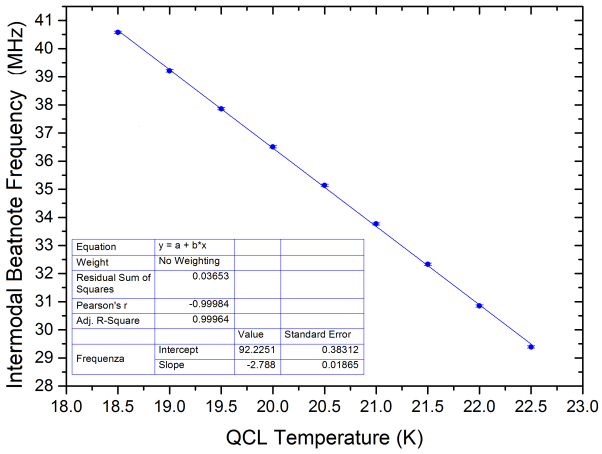

FIGURE 4.27: Electrical beat-note frequency (expressed in MHz) at different bias temperature. The tuning coefficient is retrieved by a linear fit.

The intermodal beat-note frequency is measured at different temperature values in a range of 18.5-22.5 K, as shown in Fig.4.27. As expected, a linear trend is obtained and from a linear fit of the data, the temperature tuning coefficient results -2.788 MHz/K.
As said before, it has been supposed that the LED light induces a heating on the laser bar. Consequently, a demonstration of the hypothesis is performed by observing if the LED modulation produces the same frequency shift obtained with a temperature variation.
To this purpose, a summary of the signs of the IBN and OBN frequency shifts due to the current, LED and temperature is reported in the following table. The reported signs indicate the sign of the dependence on the corresponding actuators. In other words, the signs concern the movement of the beat-notes, towards higher frequencies (+) or lower frequencies (-), while the temperature, LED or current intensity are increased.

TABLE 4.3: Schematic of the IBN and OBN frequency shift caused by the modulation of the actuator (current or LED) or temperature. The plus sign (+) denotes shift towards higher frequencies. The minus sign (-) denotes for shift towards lower frequencies.

Increase of	IBN	OBN
Current	+	-
LED	-	+
Temperature	-	-

As visible from the table, the temperature acts differently from the LED. This result excludes the hypothesis that the LED actuator has a purely thermal effect on the device. Indeed, this hypothesis could be confirmed only if the LED and the temperature acting in the same way on both the OBN and IBN. Differently, the effect observed is probably due to some phenomena in the QCL active region.

However, the current and the LED induce different frequency shift, meaning that they act differently on the QCL parameters. Nevertheless, this condition should be confirmed with further studies, described in the following section.

4.3.5 Current and LED modulation

After a preliminary characterization of the two actuators, their effects on the offset and IBN are separately observed. More specifically, with this measurement, the spacing and offset shift can be retrieved using the procedure described in the following.
The goal of the measurement is the determination of the four "actuator coefficients" which are the quantities that account how the modulation of LED or current acts on the spacing or the offset.
For a more elaborated analysis the spectrogram of the intermodal and optical beat-notes is acquired and the time evolution is analysed.
The following graphs have been obtained with a program, written in *Wolfram Mathematica* [94], in order to extract the time evolution with an elaboration of the real-time data (tiq file) taken by the spectrum analyser.

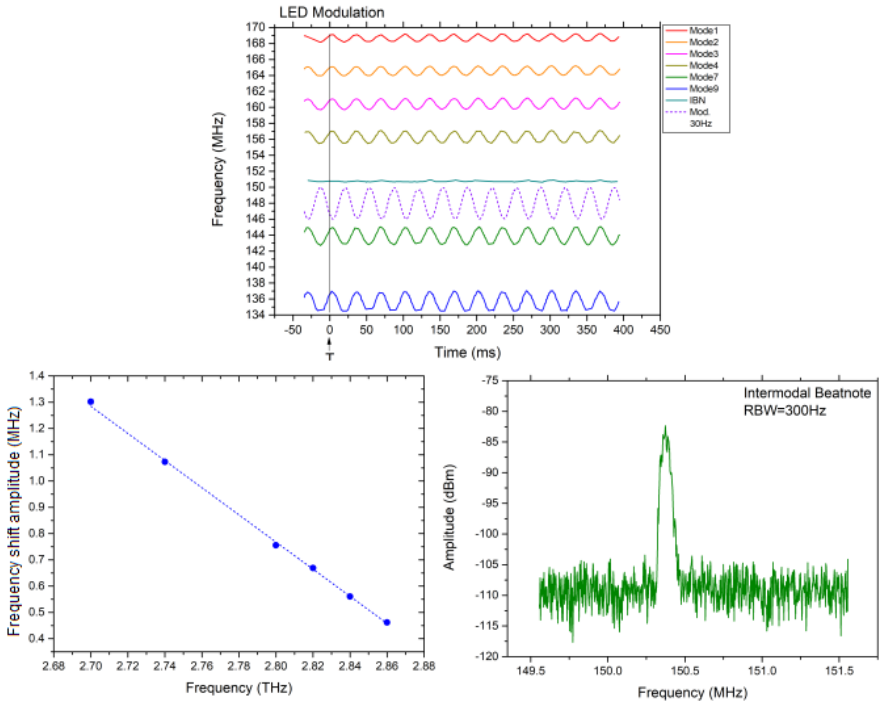

FIGURE 4.28: LED modulation on. On the top: time evolution of the IBN and OBNs. On the bottom: OBNs (on the left) and IBN (on the right) frequency shifts.

TABLE 4.4: LED modulation on. The LED is biased with a voltage $V = 1V$. The data extracted from the Fig.4.28 are reported in the table. For each QCL mode the frequency shift of the respective optical beat-note and IBN is reported.

f(THz)	Δf_{OBN} (MHz)	N	Δf_{IBN} (MHz)	N*Δf_{IBN}	Δf_{off} (MHz)
2.8636	-0.46174	145	0.125	18.125	-18.58674
2.8485	-0.56065	144	0.125	18.000	-18.56065
2.8294	-0.66903	143	0.125	17.875	-18.54403
2.8101	-0.75563	141	0.125	17.625	-18.38063
2.7481	-1.07333	139	0.125	17.375	-18.44833
2.7094	-1.30221	137	0.125	17.125	-18.42721

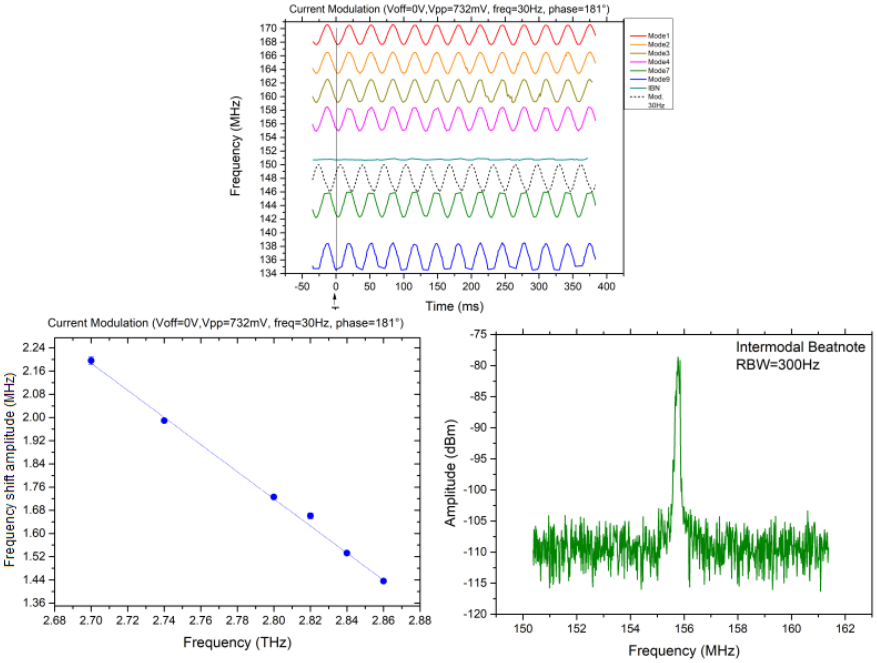

FIGURE 4.29: Current modulation on. On the top: time evolution of the IBN and OBNs. On the bottom: OBNs (on the left) and IBN (on the right) frequency shifts.

TABLE 4.5: Current modulation on. The driving current is biased with a voltage $V = 366mV$. The data extracted from the Fig.4.29 are reported in the table. For each QCL mode the frequency shift of the respective optical beat-note and IBN is reported.

f(THz)	Δf_{OBN} (MHz)	N	Δf_{IBN} (MHz)	N*Δf_{IBN}	Δf_{off} (MHz)
2.8636	1.43621	145	-0.125	-18.125	19.56121
2.8485	1.53247	144	-0.125	-18.000	19.53247
2.8294	1.66092	143	-0.125	-17.875	19.53592
2.8101	1.72549	141	-0.125	-17.625	19.35049
2.7481	1.98937	139	-0.125	-17.375	19.36437
2.7094	2.1958	137	-0.125	-17.125	19.3208

The time evolutions and the measured frequency shift of OBNs and IBN are shown in Fig.4.28 for the LED modulation and in Fig.4.29 for the current modulation.
It is clear that, in both cases, the optical beat-notes do not have the same frequency shift and this quantity is higher for lowest frequencies.
It is worth noting that the frequency shift is calculated as the half of the peak to peak value. Moreover, it is worth mentioning that the modulation with the QCL current requires an additional phase of 180^o due to the electronic of the driver circuit that includes an inverting operational amplifier.
The data, extracted by the time evolutions, are reported in the tables 4.4 (for the LED), 4.5 (for the current) where the offset contribution for each mode has been calculated with the following method.
First, one can simply verify that the OBN frequency shift is given by both the contribution of offset and spacing. To this purpose, the OBN frequency

shift can be theoretically calculated considering only the contribution of the spacing (IBN). More specifically, considering the order of the QCL mode (N) and the measured Δf_{IBN}, the frequency shift of its OBN can be estimated as N*Δf_{IBN}. This value results different from the measured one (Δf_{OBN}) as a confirmation that the OBN frequency shift involves also the offset contribution (Δf_{off}).
As a result, the OBN frequency shift can be theoretically calculated by a combination of the contribution Δf_{off} (to be retrieved) with the quantity N*Δf_{IBN}. In other words, I suppose a combination like the following:

$$\Delta f_{OBN} = N\Delta f_{IBN} \pm \Delta f_{off} \tag{4.13}$$

In the previous equation the sign $\pm$ indicates that it cannot predict the exact way in which the two contributions combine to match the measured value. Nevertheless, the exact combination can be retrieved noting that the offset contribution (Δf_{off}) has to have, by definition, a constant value for all the OBNs. The idea is to use both the two combinations and select the one that give a constant value. This can be done, if the linear contribution of Δf_{off} with N*Δf_{IBN} matches Δf_{OBN}.
More specifically, using the inverse formula ($\Delta f_{off} = N\Delta f_{IBN} \pm \Delta f_{OBN}$), the terms N*$\Delta f_{IBN}$ and Δf_{OBN} are combined once with a sum combination and then with a difference combination. The correct combination is the one for which the Δf_{off} is more similar to a constant value for all the optical beatnotes.
Following this method, the offset contribution has been calculated, a constant value has been obtained and shown in the previous tables.
Thereafter, these data are analysed to calculate the tuning coefficient.

TABLE 4.6: The tuning coefficient of current and LED modulation are estimated by the data shown in the previous tables 4.4, 4.5.

Mod.	V_{pp}(V)	$\Delta f_{off,pp}\,(MHz)$	$\frac{f_{off}}{V_{pp}}\left(\frac{MHz}{V}\right)$	$\Delta f_{IBN,pp}\,(MHz)$	$\frac{f_{IBN}}{V_{pp}}\left(\frac{MHz}{V}\right)$	$\frac{\Delta f_{off}}{\Delta f_{IBN}}$
LED	2	-36.98	+18.5	0.25	-0.125	-147.9
i	0.732	+38.88	-53.11	-0.25	+0.34	-155.5

A further elaboration of the previous results is summarized in table.4.6. The voltage tuning coefficient for both the IBN and offset, and for both the actuators is calculated.
In this way, an estimation about the possibility that the two actuators act differently on offset and IBN is given by the ratio $\Delta f_{offset}/\Delta f_{IBN}$.
The retrieved results show that, for both the cases in which the modulation of the light and of the current is applied, the IBN results to be less perturbed with respect to the offset. Moreover, the current modulation has a stronger effect on the offset with respect to the LED.
Furthermore, the results reported in the table show that the offset contribution has a different sign for the two kinds of modulation. This suggests that if the two modulations are applied and summed in phase, the total contribution on the offset is zero. From an experimental point of view, this effect can be easily verified observing the IBN frequency shift until it reaches a zero

value.
The idea is to combine the two modulations in order to cancel the IBN modulation with a compensation between two opposite effects. In this way, their relative phase is adjusted with an iterative procedure until the IBN seems to be as stable as possible, like when a phase locked is applied.

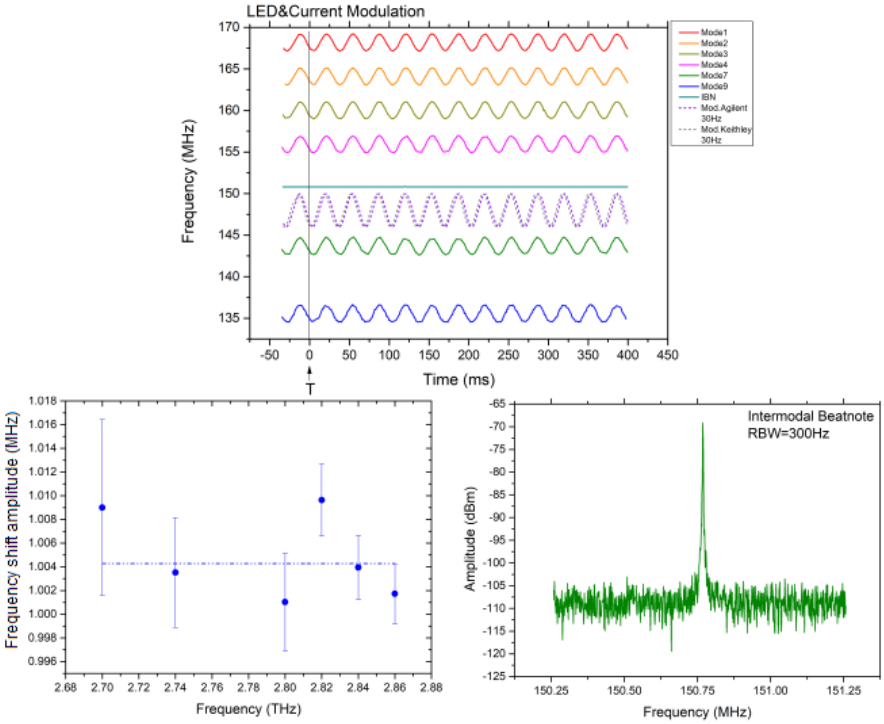

FIGURE 4.30: LED and current modulation on. On the top: time evolution of the IBN and OBNs. On the bottom: OBNs (on the left) and IBN (on the right) frequency shifts.

TABLE 4.7: LED and current modulation on. The data extracted from the Fig. 4.30 are reported in the table. For each QCL mode the frequency shift of the respective optical beat-note and IBN is reported.

f(THz)	Δf_{OBN} (MHz)	N	Δf_{IBN} (MHz)	N*Δf_{IBN}	Δf_{off} (MHz)
2.8636	1.00173	145	0	0	1.00173
2.8485	1.00395	144	0	0	1.00395
2.8294	1.00964	143	0	0	1.00964
2.8101	1.00103	141	0	0	1.00103
2.7481	1.00352	139	0	0	1.00352
2.7094	1.00901	137	0	0	1.00901

In this condition, the time evolution and the measured frequency shift of OBNs and IBN are shown in Fig.4.30. The IBN appears very stable and its frequency shift is negligible. As a consequence, the optical beat-notes have the same frequency shift. The reason is that the contribution of the IBN has been reduced and the OBNs frequency shifts are mainly due to the offset. The elaboration of these data and the estimation of the offset contribution are reported in table 4.7.

Derivation of the fixed-point

From the measurement just described, it can be determined the frequency point that does not undergo a frequency shift when the LED or current modulation is applied. Generally, the response of a frequency comb's modes to a specific control can be intuitively described in terms of an elastic ribbon model and a fixed-point of the comb. The latter is a single frequency which remains stationary while the comb expands or contracts about it [95].
The expression for the point in the comb that remains fixed can be obtained by requiring the differentiation of the comb equation ($f = m * f_{IBN} + f_{off}$):

$$\Delta f_{fix} = m_{fix}\Delta f_{IBN} + \Delta f_{offset} = 0, \tag{4.14}$$

where Δ indicates a variation due to intensity modulation and m_{fix} is, in general, not an integer. Substituting m_{fix} into $f = m_{fix}f_{IBN} + f_{off}$ yields the fixed-point frequency:

$$f_{fix} = f_{offset} + \left(-\frac{\Delta f_{offset}}{\Delta f_{IBN}}\right) f_{rep} \tag{4.15}$$

With this expression the frequency of the fixed-point can be calculated for both the two actuators:

$$LED: \qquad N = (-\frac{\Delta f_{offset}}{\Delta f_{IBN}}) = 148 \rightarrow f_{fix} = 2.9222\,THz \tag{4.16}$$

$$Current: \qquad N = (-\frac{\Delta f_{offset}}{\Delta f_{IBN}}) = 155 \rightarrow f_{fix} = 3.060\,THz \tag{4.17}$$

where $f_{off} = -5301$ MHz and $f_{IBN} = 19.781$ GHz.

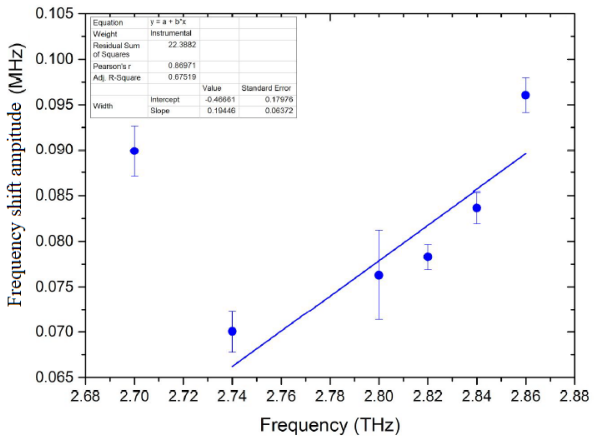

FIGURE 4.31: Measurement of the frequency of the fixed-point in the free-running condition.

Moreover, the fixed-point is calculated in the free running operation. In this condition, the frequency shifts of the optical beat-notes are measured and reported in function of their absolute frequencies. The intercept of the linear fit gives the frequency at zero width which is the fixed-point (Fig.4.31):

$$Free - running: \qquad f_{fix} = 2.421\,THz. \tag{4.18}$$

4.3.6 Phase Locking

Phase locking a laser to a reference involves to precisely control the phase of the laser radiation field. In this way, the frequency is stabilized and the line profile of the reference is transferred to the laser.
As said before, the idea is to use the driving device current and the white led to lock both QCL-IBN and the offset, the latter by locking one OBN to the FCS.
In order to perform a double phase lock, four possible combinations can be performed, as sketched in the following table 4.8.

TABLE 4.8: Schematic of the four possible phase-lock combinations.

	OBN	IBN
LED	⋆	⋆
Current	⋆	⋆

The first step consists on the analysis of each single phase-lock.

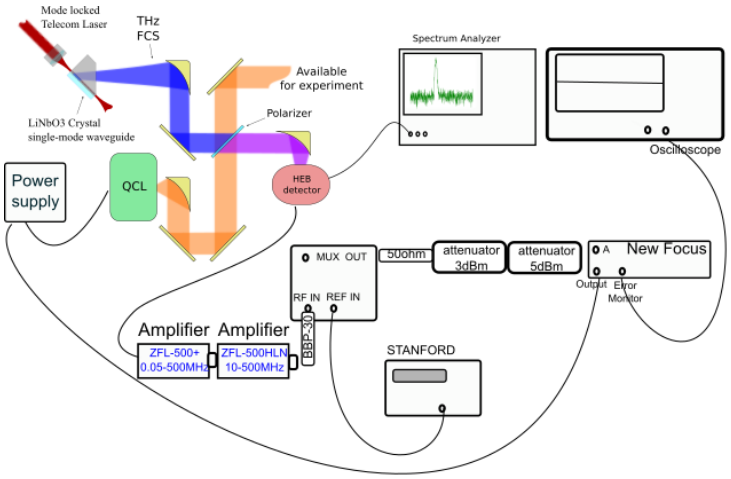

FIGURE 4.32: Schematic of the electronic setup for the phase-lock of the OBN with the driving current actuator.

Two examples of the electronic setup used for the phase lock are sketched. The phase-lock of the OBN with the current is shown in Fig.4.32, while the phase lock of the IBN with the LED is shown in Fig.4.33.
A typical phase-lock loop circuit consists of a phase detector, loop filter, voltage controlled oscillator (VCO) and a divider. The beat-note to be phase-locked is processed by a home-made phase-detection electronic, which compares it with a 40-MHz local oscillator (LO) and provides the error signal for closing the phase-locked loop (PLL). The actuator (LED or current) compensates the error signal.

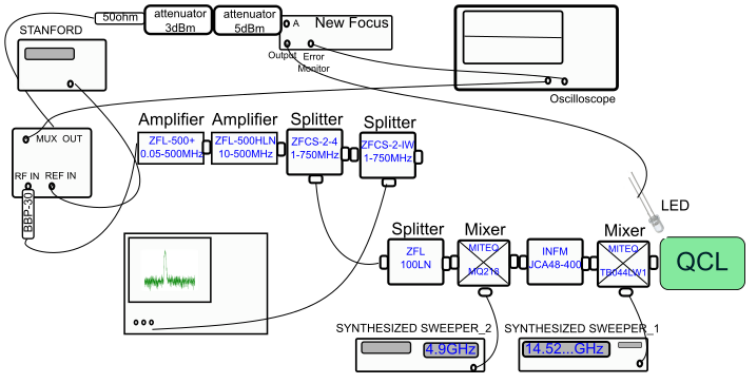

FIGURE 4.33: Schematic of the electronic setup for the phase-lock of the IBN with the LED actuator.

Locking the intermodal beat-note

The phase-lock of the intermodal beat-note is discussed in this section.

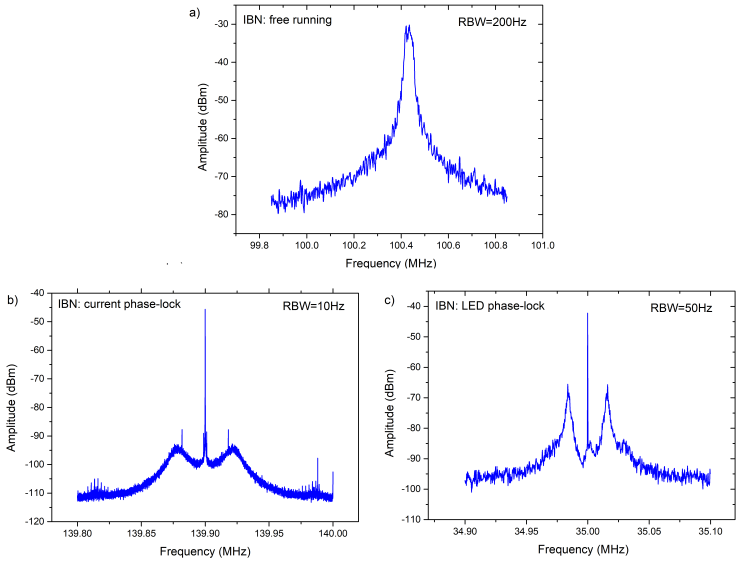

FIGURE 4.34: Intermodal beat-note in the free running condition (a) and in the phase-lock condition alternatively with the current (b) and with the LED (c).

The IBN is shown in Fig.4.34 in the free running (a), in the phase lock condition with the QCL driving current (b) and with the LED light (c).
When the IBN is phase-locked, the servo bands in (b) and (c) have different shapes. The reason is that the two phase-locks have different gain parameters, loop performance and bandwidth of lock. More specifically, for the current, the servo bands are broader. Indeed, as analysed in section 4.3.4, the LED actuator has a reduced bandwidth.

Locking the optical beat-note

Concerning the phase-lock of the optical beat-note, it is worth noting that the OBN under analysis is the one labelled with the number "9".

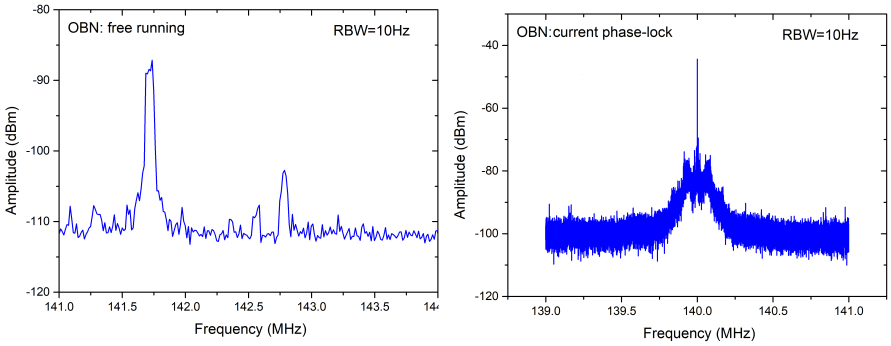

FIGURE 4.35: Optical beat-note in the free running condition (on the left) and in the phase-lock condition with the current (on the right).

The OBN is shown in Fig.4.35 in the free running (on the left) and in the phase lock condition with the QCL driving current (on the right).
The phase lock of the OBN with the LED actuator has not been performed because some problems with the electronic setup have been encountered. Indeed, as described before, the LED is a slow actuator that has a reduced bandwidth. In this way, the phase-lock with the LED is not a trivial task. This kind of phase lock works correctly on signal with a width of few kHz, as done with the IBN. Indeed, the OBNs have a width of few MHz and the phase-lock with the LED actuator does not work. Further improvements of the electronic phase-lock loop will be considered.

Effect of the IBN locking an OBNs

During the phase-lock of the IBN some induced perturbation on the OBN have been observed and analysed.

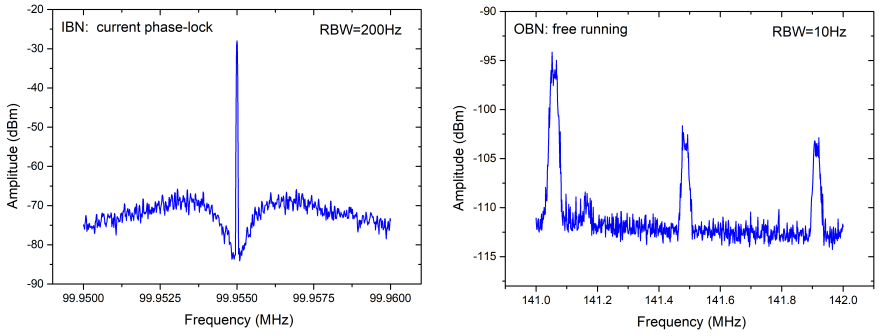

FIGURE 4.36: On the left: intermodal beat-note phase-locked. On the right: optical beat-note when the intermodal beat-note is phase-locked.

The IBN and three OBNs are reported in Fig.4.36 when the IBN is phase-locked with the current actuator.
As shown in figure 4.36, closing the loop on the electrical beat-note clearly broadens the optical signals as clearly if one compares with the free running condition shown in Fig.4.35. This is probably due to the fact that the current

actuator acts not only on the IBN but also on the offset. In this way, an additional shift is observed.
Moreover, a small contribution is due to the ground loop in the lab, as the laser current supply is battery driven.

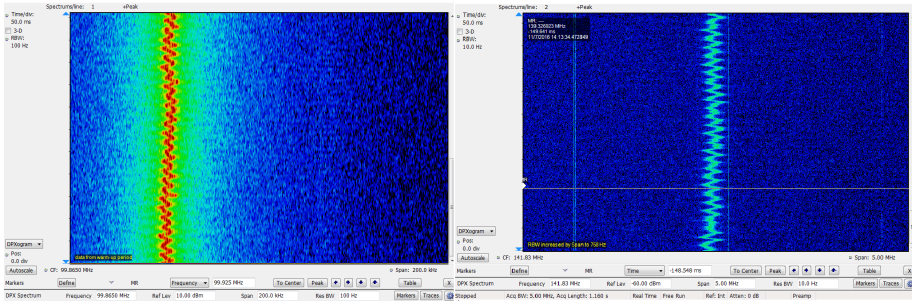

FIGURE 4.37: Time evolution of the IBN (on the left) in the free-running condition and of the OBN (on the right) when the IBN is phase-locked.

In order to explain the effect, time evolution of the signals is shown in Fig.4.37. On the left, the acquisition of the IBN in free running conditions (like Fig.4.34) is reported. On the right, the acquisition of the OBN (n.9) with the IBN phase locked (like Fig.4.35) is reported. It is clear that the phase lock transfers the noise from one signal to the other.

Active compensation

To conclude, a detailed analysis of the contribution of the IBN on the OBNs is described. The goal is to observe how the free-running or the phase-locking condition of the IBN can produce a frequency shift on the OBNs. In this way, the offset contribution can be calculated.

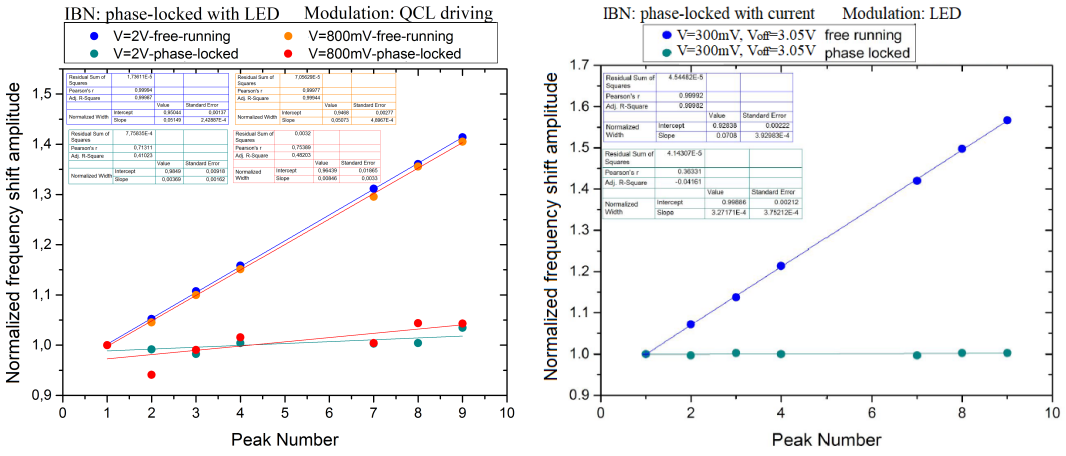

FIGURE 4.38: Normalized frequency shift of the optical beat-notes in the free running condition and when the IBN is phase locked. On the left: current modulation on. On the right: LED modulation on.

The frequency shift amplitude of each OBN are measured when the IBN is phase-locked with the LED, shown in Fig.4.38 (left) and when the IBN is

phase-locked with the current, shown in Fig.4.38 (right). When the IBN is phase-locked, the current or alternatively the LED are modulated to observe their effects on the OBNs. The frequency shifts of the OBNs are measured at two different working conditions of the two actuators.
As shown in the graphs, when the IBN is phase-locked, the OBNs have the same frequency shift as clearly if one considers that $\Delta f_{IBN} = 0$. In other words, their frequency shifts now depend only on the offset.
Differently, when the IBN is free-running, the OBNs frequency shifts include also the IBN contribution and its effect is highest for highest frequencies.
Moreover, the OBNs at highest frequencies result narrowest. In order to understand these phenomena, a further analysis concerns how the contribution of the offset and IBN acts to the total frequency shift of the OBNs, as described in section 4.3.5.

TABLE 4.9: Current modulation on. The driving current is biased with a voltage $V = 2V_{pp}$. The data extracted from the Fig. 4.38 are reported in the table. The frequency shifts of the OBNs, IBN and offset contribution are reported.

f(THz)	Δf_{OBN} (MHz)	N	Δf_{IBN} (MHz)	N*Δf_{IBN}	Δf_{off}
2.8636	9.19599	145	0.48	69.6	78.79599
2.8485	9.67661	144	0.48	69.12	78.79661
2.8294	10.18413	143	0.48	68.64	78.82413
2.8101	10.65022	141	0.48	68.16	78.81022
2.7481	12.05877	139	0.48	66.71	78.77877
2.7249	12.5134	139	0.48	66.24	78.7534
2.7094	13.00046	137	0.48	65.76	78.76046

TABLE 4.10: LED modulation on. The LED is biased with a voltage $V = 300mV_{pp}$. The data extracted from the Fig.4.38 are reported in the table. The frequency shifts of the OBNs, IBN and offset contribution are reported.

f(THz)	Δf_{OBN} (MHz)	N	Δf_{IBN} (MHz)	N*Δf_{IBN}	Δf_{off}
2.8636	7.56059	145	0.54	69.6	77.16059
2.8485	8.06886	144	0.54	69.12	77.18886
2.8294	8.61523	143	0.54	68.64	77.25523
2.8101	9.05704	141	0.54	68.16	77.21704
2.7481	10.71791	139	0.54	66.72	77.43791
2.7249	11.23571	139	0.54	66.24	77.47571
2.7094	11.72015	137	0.54	65.76	77.48015

The tables 4.9 and 4.10 are equivalent to the tables 4.5, 4.4. As explained before, the frequency shifts of the OBNs are given by the contribution of the offset and IBN. Moreover, in the phase-lock condition, the offset has the same contribution for all the modes.

Finally, it is shown how the two actuators act differently on offset and IBN, as summarized in table.4.11. The retrieved values are similar to the one shown in table 4.2.

TABLE 4.11: Tuning coefficient of current and LED modulation estimated with the data shown in the tables 4.10 and 4.9.

Mod.	V_{pp}(V)	$\Delta f_{off,pp}\ (MHz)$	$\frac{f_{off}}{V}\ \left(\frac{MHz}{V_{pp}}\right)$	$\Delta f_{IBN,pp}\ (MHz)$	$\frac{f_{IBN}}{V_{pp}}\ \left(\frac{MHz}{V}\right)$	$\frac{\Delta f_{off}}{\Delta f_r}$
LED	0.300	77.21	257	0.540	1.8	143
i	2	78.8	39.4	0.480	0.240	164

Locking both the QCL offset and the intermodal beat-note

The further step is the double phase-lock of both the offset (through the OBNs) and the IBN. Nevertheless, some problems have been encountered.

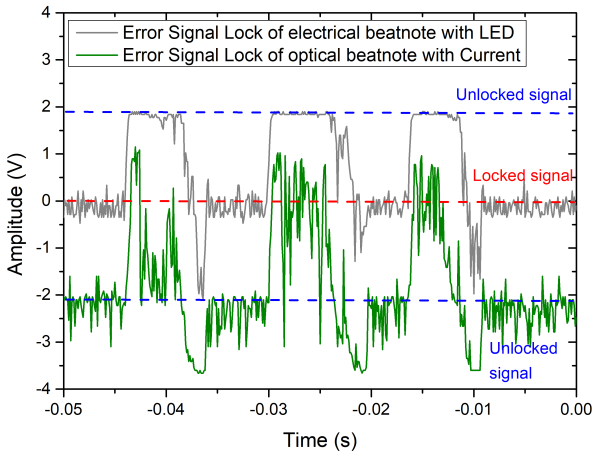

FIGURE 4.39: Signals errors of the phase lock with LED and current, observed on the oscilloscope.

In order to better explain the reason why the double phase-lock does not work, the signal errors of the phase lock with LED and current, observed on the oscilloscope are shown in the figure 4.39.
The two actuators are exclusive: when one actuator is locked (level $+0$V), the other one is out of lock (level -2V or $+2$V). In other words, the two actuators cannot work simultaneous to perform a double phase-lock of IBN and offset.

4.3.7 Frequency difference: an alternative way to phase lock

In order to overcome the problems in the double phase-lock, described before, a tempting idea is to simulate a phase-lock loop by subtracting the frequency of one OBN to the other ones. The difference operation would subtract the offset contribution. In this way, if the common oscillation to all the OBNs is removed, the frequency difference will reduce the OBNs frequency shifts.
More specifically, the frequency shift of the OBN n.9 is subtracted to the other OBNs (8-1), that is mixing the whole train of beating notes with the ninth one.

The electronic setup, shown schematically in Fig.4.40, is almost equivalent to a phase-lock of one beat-note. The signal from the HEB is sent to a

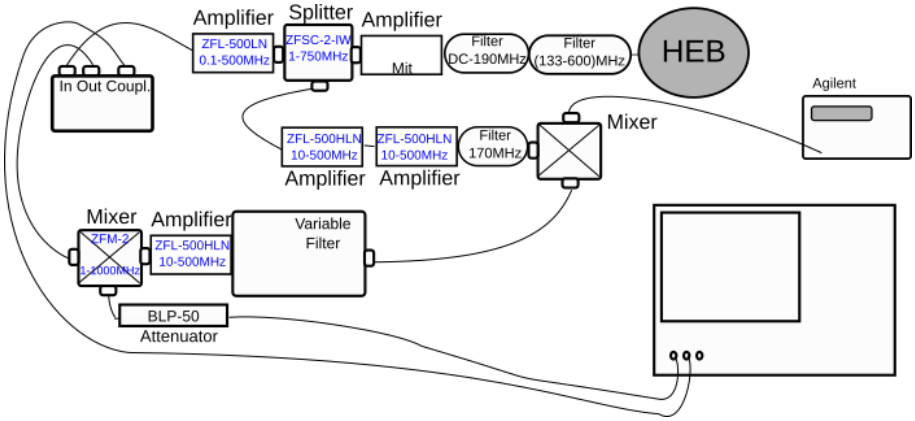

FIGURE 4.40: Electronic set-up used for the frequency difference operation.

couple of filters in order to extract the band from 133MHz to 190MHz. A splitter divides equally the signal in two parts. One fraction is amplified, filtered and then mixed with the signal of the power generator, which provides the shift of the signal. Differently, the other fraction is sent in a mixer where, recombined with the shifted signal, and the subtraction is performed.

Free running operation

In the frequency difference configuration, the frequency noise of the first OBN is subtracted (with an offset) to all the others.
This operation is the opposite to the one described in 4.3.5. In that case, the LED and the current modulations are both applied to the device in order to stabilize the IBN and the IBN contribution is suppressed. Differently, in this case, the offset contribution is subtracted to all the OBNs.
Nevertheless, the noise compensation on the other OBNs (8-1) is not perfect, indicating that not all the QCL frequency noise is a common-mode (offset) noise. Despite this, a residual noise due to the fluctuations of the QCL teeth spacing is still present.

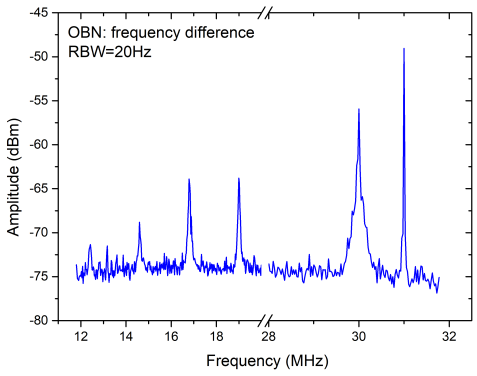

FIGURE 4.41: Optical beat-notes after the subtraction of the frequency of the first OBN, labelled with n.9.

The frequency of the OBN, labelled with n.9, is subtracted to the others that were just shifted in order to avoid a zero-resulting frequency of the 9-OBN. The acquired spectrum is shown in Fig.4.41.

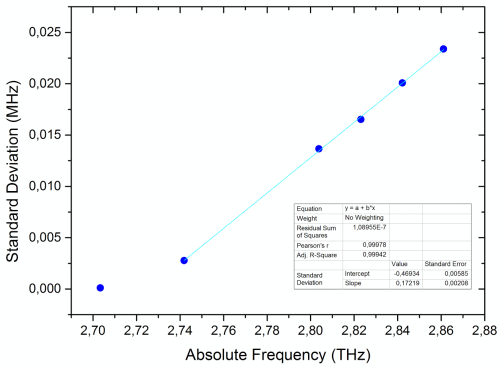

FIGURE 4.42: Standard deviation obtained by the linear fit of the OBN frequency shift versus the frequency mode.

The frequency shift of the OBNs, when the frequency difference is applied, has been analysed and several measurements have been performed. The results are reported in Fig.4.42. The data concern successive acquisitions in time of the OBNs. During these acquisitions, fluctuations are still present. For this reason, the average value of the standard deviation obtained by a linear fit of each acquisition is reported.

Application of the LED modulation

After removing the offset contribution, the OBNs, in the frequency difference operation, are observed when the LED intensity is modulated. In this way, the perturbation could concern only the IBN and the frequency shift could be the same for all the OBNs.

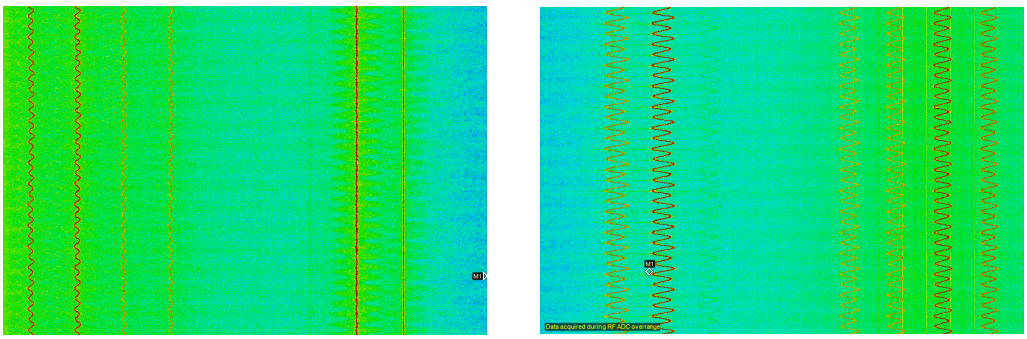

FIGURE 4.43: Screen-shot of the spectrum analyser (RBW=20kHz, Span=40MHz). The optical beat-notes are shown when the frequency difference is performed (on the left) and when the LED modulation is applied (on the right). For clarity in comparison, their time evolutions are reported.

The time evolution of two different spectra in the difference frequency operation are shown in Fig.4.43. The images are screen-shots directly taken

from the spectrum analyser.
The time evolution of the OBNs when the frequency difference is applied, shown in the spectrum on the left. It is visible that the OBN subtracted to the others, is clearly very narrow because of the difference with itself. Instead, the widths of the OBNs increase with the distance from the first one.
Differently, when the LED intensity is modulated, the frequency shift of the OBNs seems to be the same as shown in the spectrum, reported on the right of the figure.

Locking the electrical beat-note

In the frequency difference configuration, the phase-lock of the IBN can be a way to simulate a double phase lock. In this way, the frequency shift of the OBNs is measured as an estimation of the condition in which both the offset and the IBN are locked.

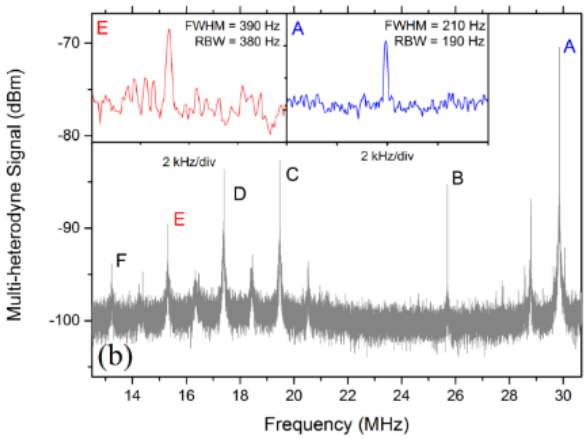

FIGURE 4.44: Example of the multi-heterodyne signal spectrum showing the optical beatings between QCL and the THz FCS (labelled from A to F), while the QCL modes spacing is phase locked to a microwave local oscillator and the QCL-comb offset frequency has been subtracted.

In this configuration, by stabilizing the QCL-comb spacing to a microwave local oscillator, the phase coherence between the QCL modes has been directly observed and characterized (see fig. 4.44). Clearly this graph puts in evidence that any single beat-note is narrowed down the instrumental limit (see insets for beat-notes A and E) and confirms that modes are highly coherent.
The locked tooth emission linewidth is therefore narrowed down to the level of about 100 Hz. If a double phase-lock is performed, it will allow the narrowing of all the comb teeth down to the above-mentioned level.

4.3.8 Measurement of the phases of the QCL-comb modes

The measurements described in the previous sections have shown that the QCL emission has a true comb-like structure, which can be parameterized

by the two typical comb quantities "offset" and "spacing". A mandatory step is the demonstration that the QCL emits as a coherent optical comb with a phase relation between the QCL modes.
To this purpose, the measurement requires a QCL spectrum as stable as possible by reducing the frequency shifts. As already described, in the last part of the experiment, the offset fluctuations are removed with a frequency difference operation and the IBN is phase locked. This configuration is a proven way to simulate a double phase-lock of the device. Moreover, by locking the comb-OR repetition rate, the phase coherence between the QCL modes can be directly observed and characterized.
The measurement is performed as follows. The optical beat-notes are observed with the spectrum analyser and data are acquired with a kind of time-evolution acquisition (IQT) that gives the in-phase and in-quadrature component of the signal.
The data stream has a total acquisition time of 440 ms, with a 37.5 Msample of acquisition rate, and is divided, for istance, into 20 frames of 22.3 ms acquisition time. Afterwards, for each frame the Fast Fourier Transformation (FFT) of the signal (amplitude and phase) has been computed with a data-analysis program.

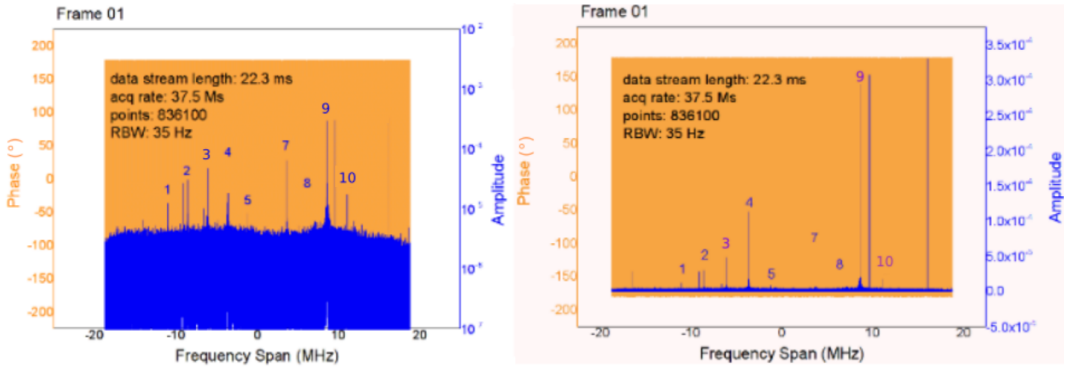

FIGURE 4.45: Phase (orange) and amplitude (blue) of the acquired spectra, obtained with a Fast Fourier Tramsformation. The optical beat-notes are labelled. On the left: amplitude expressed in dBm. On the right: amplitude expressed in linear scale.

The obtained amplitude (in blue) and phase (in orange) of the acquired spectra, obtained with the FFT are shown in Fig.4.45. From these data, the spectrum of the OBNs is retrieved and the phase appears as an apparently noise band.

In order to elaborate the data, the phase signal on the single peak, shown in Fig.4.46 is analysed. Considering that the FFT is a discrete operation, the mode phase is assumed to be the phase of the FFT point corresponding to the peak in the amplitude spectrum. More specifically, the value of the phase (tagged with a red point) is taken at the centre frequency of the peak. This procedure is performed for each peak and then, for each frame, using a program written in *Mathematica*.

After the elaboration of the data, the residuals are reported in function of the QCL modes at different frames (Fig.4.47). Within each group, one can

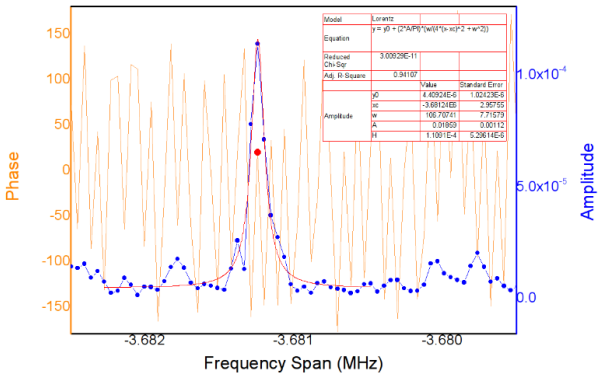

FIGURE 4.46: Amplitude (in blue) and phase (in orange) of the peak nr.4 of the graph shown in Fig.4.45.

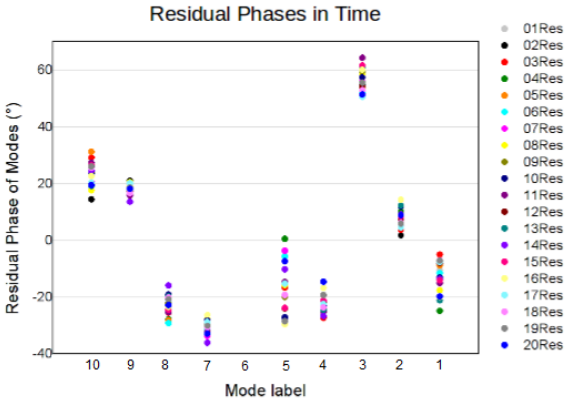

FIGURE 4.47: Phase analysis. Elaboration of the data extracted from the graph 4.45.

say that the phases of the modes are constant over a 440 ms timescale. Apart from that the data are affected by errors in the measurement and systematic residual effect, it is clear that the phase of each mode is well defined and constant in the time as follows from the fact that the relative value of each mode is quite the same for all the frames. In other words, the measurement provides that the phase is clearly stable over the whole acquisition. However, these results are still preliminary, and a more detailed analysis is necessary. Nevertheless, this measurement is an unequivocal proof of a phase-relation between the QCL modes, demonstrating the comb-like nature.

Conclusion

To conclude, I report here a summary of the main results obtained in this work, along with some future perspectives.
The main theme of this work has been the development and application of terahertz spectroscopy tools. The goal was to improve the performance of the THz spectrometer developed in the past years by my advisor's group and based on THz frequency comb synthesizer in combination with THz quantum cascade lasers. To this purpose, high-resolution THz spectroscopic techniques have been developed. In order to increase the sensitivity of the spectroscopic system, resonant THz cavities have been set up and characterized. Then, the metrological-grade system has been improved and employed for the characterization and exploration of the properties of THz sources.

The first part of this work concerns the study and the experimental realization of three different resonant cavities (V-shaped, ring-shaped and bow-tie cavity), tested with a THz QCL. The cavities are based on Au-coated mirrors and free-standing wire-grid polarizers acting as input/output couplers. A complete characterization is reported, and their parameters, experimentally obtained, result to be in good agreement with the calculated ones.
The V-shaped and the ring-shaped cavities reach a finesses $F \approx 60$ proving to be the first resonators with $Q > 10^5$ at frequencies well above 1 THz (in this case 2.55 THz).
The present work also shows the effect of the optical feedback from an external resonator (the V-shaped cavity) on the QCL frequency. The validation of this effect has been made possible by using the second cavity (the ring-shaped one) as transducer of the QCL frequency fluctuation under OF condition. This first evidence opens up interesting perspectives on the narrowing and control of the emission frequency of a QCL by means of THz resonant cavities.
Moreover, the third cavity, i.e. the bow-tie shaped, has been designed to push the current finesse value towards higher level with respect to the previous geometries (V-shaped and ring-shaped). The bow-tie cavity represents a way to keep the key aspects of the V-shaped and ring-cavity, improving the Q-value to 8.1×10^6.
Further improvements are expected by using metallic mirrors with larger reflectivity (e.g. unprotected gold coated mirrors), with respect to the ones used in this work, thus leading to $Q > 10^6$.
THz cavities with this performance will be fundamental tools for the next generation of high-sensitivity and high-resolution THz spectroscopic experiments based on QCLs. In this way, not only an outstanding enhancement of the available optical power will be provided, but also a narrow reference for

the QCL frequency.
The second activity of this work deals with the improvement of the metrological grade system developed in the past years. The system consisted in a FCS generated by a non-linear crystal ($LiNbO_3$) by optical rectification of a Ti:Sapphire fs laser, emitting at 800 nm, and the generation was based on Cherenkov emission.
Concerning the performance of the THz FCS, an upgrade of this system is proposed by changing the pump source. The latter has been upgraded to an Erbium fiber fs-laser, working at 1.5 μm wavelength, with 350 mW average power and 250 MHz of repetition rate and with $\sim 60 fs$ width pulses.
With this system, a generation efficiency of 10^{-4} at room temperature has been reached. The light emitted is a THz comb, with the repetition rate of the pump laser and a zero-offset.
Then, the work deals with the detection of beat-notes between the THz-comb and a THz-QCL. The detection of these beat-notes is the first step for the phase-locking of a QCL to the THz comb in order to stabilize and control the QCL emission, performing high resolution spectroscopy.
Furthermore, the detection of the beat-notes is useful to measure the tuning characteristics and the absolute emission frequency of terahertz sources. As a matter of fact, this metrological grade system has been used to characterize two different designs of QCLs.
The first characterized device is based on intracavity difference-frequency generation in QCL. Recently, this kind of source has emerged as the first monolithic electrically pumped semiconductor source capable of operating at room temperature across the 1-6 THz range. In this thesis, for the first time, the free-running emission linewidth, the tuning characteristics, and the absolute emission frequencies of this source have been measured with an uncertainty of $4x10^{-10}$.
The measured emission linewidth (400 kHz at 1-ms integration time) indicates that DFG-QCLs are well suited to operate as local oscillators and so they could be exploited in a variety of metrological, spectroscopic, communication, and imaging applications that require narrow-linewidth THz sources. Furthermore, the accuracy of the techniques used in this work allows to unveil the current- and temperature-induced tuning, so providing relevant information for the building of low-chirp and low–frequency noise THz emitters by a novel design of the gain media for these devices.
Finally, the second kind of QCL that has been characterized is a broadband multimode QCL, specifically developed for a coherent comb-like operation thanks to the four-wave mixing processes occurring in its active region. Its tuning characteristics and the absolute centre frequencies of its modes are measured as done for the previous device.
The characterization of this device demonstrates that the QCL emission has a true comb-like structure, which can be parametrized by the two typical comb quantities "offset" and "spacing". Their dependence from the operational parameters (such as driving current) is characterized and explored. Further analyses are motivated by the fact that it would be very important to completely control this kind of device, through the two equivalent comb

quantities: the offset and the intermodal beatnote. Indeed, these investigations have concerned a careful analysis on the possibility to use the driving current and the light of a LED as two independent actuators to phase lock both the QCL offset and IBN. Despite the two actuators have revealed to be far from the orthogonal condition, the QCL parameters can be separately controlled to explore their properties.
For this reason, a detailed analysis about the way in which the two actuators act on the IBN and offset is reported. The two parameters are investigated when the modulation of the LED intensity or the driving current is applied. In both cases, the offset results to be more perturbed with respect to the IBN. Furthermore, by properly combining the two actuators, it has been demonstrated that the IBN fluctuation can be compensated.
In the final part of the experiment, a phase lock is separately performed on both the IBN and on an optical beatnote. Despite problems have been encounted for the double phase-lock, the latter is simulated with an alternatively method. The latter consists on the elimination of the offset fluctuations by means of a frequency difference operation while the IBN is phase locked. In this configuration, the phase coherence between the QCL modes has been directly observed and characterized. Whilst these studies are preliminary, the measurement is an unequivocal proof of the phase relation between the QCL modes, confirming the comb-like nature.
Moreover, the possible availability of a second independent actuator for the QCL parameters, that is presently under investigation, will likely enable a full control of the whole emitted spectrum allowing the narrowing of all the comb teeth down to the retrieved level (100 Hz). However these results represent the first milestone towards a full control of the device by means of the double phase lock of the two QCL parameters.

Acknowledgements

Alla fine di questo percorso universitario desidero ringraziare il Dott. Paolo De Natale per avermi dato la possibilità di fare parte del suo gruppo di ricerca in cui ho svolto il mio lavoro di tesi magistrale ed il mio dottorato di ricerca.
Il più sentito ringraziamento va al mio relatore Saverio Bartalini, che mi ha accolto nel suo laboratorio. Lo ringrazio per la conoscenza che mi ha trasmesso, da cui ho appreso la scrupolosa e puntuale precisione nel lavoro.
Un importante punto di riferimento è stato Luigi Consolino, con cui ho condiviso l'esperienza in laboratorio e da cui ho appreso l'arte del lavoro sperimentale.
Ringrazio il prof. M.Belkin ed il prof. G.Scalari per aver fornito i due laser QCL, parte fondamentale del mio lavoro di tesi, permettendo il raggiungimento di alti risultati scientifici.
Ringrazio il prof. Oscar Adriani con il quale ho svolto l'attività di tutor studenti durante questi anni di dottorato. Lo ringrazio per avermi aggiunto un tassello di crescita professionale che ricorderò sempre con piacere.
Dietro questo lavoro, c'è inoltre il contributo di diverse persone che, ognuno in forma diversa, hanno contribuito alla riuscita di questo percorso.
Ringrazio i miei colleghi di ufficio: Alberto, Stefano, Davide, Demetrio che più che colleghi si sono mostrati amici soprattutto grazie ai loro fondamentali consigli che mi hanno sostenuto nei momenti più intensi del dottorato.
Ringrazio Rocco, Gabri, Wies, Tommy e Marco con i quali ho condiviso le tante pause pranzo ma soprattutto le tante serate trascorse insieme, ricche di tanti ricordi positivi.
Ricordo e ringrazio Polina e Katia per le giornate condivise insieme. Un grazie va a Beatrice per i consigli e l'incoraggiamento che mi ha dato, ma soprattutto per le serate piene di divertimento che hanno reso così piacevole anche i periodi più intensi.
Un grande ringraziamento va alla mia oramai storica amica, Sissi, con la quale ho avuto la fortuna di condividere il mio percorso universitario durante il quale ha sempre creduto in me e nelle mie capacità, spingendomi sempre ad andare avanti.
Infine, il più grande ringraziamento va alla mia famiglia, che ha costituito il più grande contributo per la riuscita di questo percorso grazie ai loro consigli e per il sempre costante ed eterno sostegno.

List of Publications:

"Unveiling spectral purity and tunability of terahertz quantum cascade laser sources based on intra-cavity difference frequency generation", L.Consolino, S.Jung , **A.Campa** , M.De Regis, S.Pal, J.Hyun Kim , K.Fujita , A.Ito , M.Hitaka , S.Bartalini, M.Belkin, P.De Natale*, Science Advances, **9**, 1-8, (2017).*

‘’Towards Doppler-Free QCL-based Metrological THz Spectroscopy” , L. Consolino, S. Bartalini, **A.Campa**, M. Ravaro, H. E. Beere, D. A. Ritchie, M. S. Vitiello, P. Cancio, D. Mazzotti, P. De Natale*, Conference paper: Cleo 2014:Science and Innovations,10.1364, 2014.*

*”Saturated absorption in a rotational molecular transition at 2.5 THz using a quantum cascade laser”,*L.Consolino, **A.Campa**, M.Ravaro, D.Mazzotti, M.S.Vitiello, S.Bartalini. P.De Natale*, Appl. Phys. Lett.**106**, 021108-021112 (2015).*

“High-Q resonant cavities for terahertz quantum cascade lasers”, **A.Campa**, L.Consolino, M.Ravaro,D.Mazzotti, M.S.Vitiello, S.Bartalini. P.De Natale*, Optics Express, Special issues QCL, **23**, 3751-3761 (2015).*

Works presented at national/international conferences:

”Bow-tie cavity for THz light”, **A.Campa**, L. Consolino, D. Mazzotti, M. S. Vitiello, S. Bartalini, and P. De Natale*, International Quantum Cascade Lasers School and Workshop, 4-9 September 2016 Cambridge, UK, poster presentation.*

”Bow-tie cavity for THz light”, **A.Campa**, L. Consolino, D. Mazzotti, M. S. Vitiello, S. Bartalini, and P. De Natale*, Quantum Cascade Lasers School and Workshop, 28-30 August 2016 Ile de Porquerolles, France, poster presentation.*

”Bow-tie cavity for THz light”, **A.Campa**, L. Consolino, D. Mazzotti, M. S. Vitiello, S. Bartalini, and P. De Natale*, Fotonica 2016, Università di Roma La Sapienza, 6-8 June 2016, Roma, Italia, oral presentation.*

‘’New tools for QCL-based THz Spectroscopy”, **A.Campa**, L. Consolino, M. Ravaro, D. Mazzotti, M. S.Vitiello, S. Bartalini, and P. De Natale*, FisMat 2015, Univeristà di Palermo, 28 September- 2 October2015, Palermo, Italia, oral presentation.*

‘’QCL-based metrological-grade THz spectroscopy tools‘’, **A.Campa**, L. Consolino, M. Siciliani de Cumis, D. Mazzotti, M. Ravaro, M. S. Vitiello, S. Bartalini, P. Cancio, and P. De Natale*, LENS Poster session, 26 May 2015, Firenze.*

*"Evidence of saturation effects in CH3OH molecule by means of THz QCL based spectroscopy",***A. Campa** , L. Consolino, S. Bartalini , M. Ravaro , H. E. Beere D. A. Ritchie, M. S. Vitiello,P. Cancio, D. Mazzotti, P. De Natale*, INO Annual Symposium, Brescia , 1-3 October, 2014, poster resentation.*

*"Evidence of saturation effects in CH3OH molecule by means of THz QCL based spectroscopy",***A. Campa** , L. Consolino, S. Bartalini , M. Ravaro , H. E. Beere D. A. Ritchie, M.

S. Vitiello,P. Cancio, D. Mazzotti, P. De Natale*, International Quantum Cascade Lasers School& Workshop 2014, Policoro (Matera), 7-12 September, 2014, poster presentation.*

‘’Toward metrological-grade sub-Doppler THz spectroscopy”, M. Ravaro, L. Consolino, **A.Campa**, D.Mazzotti, M.S. Vitiello, S.Bartalini, and P.De Natale*, FisMat 2015, Università di Palermo, 28 September –2 October 2015, Palermo, Italia.*

‘’ High-Q resonant cavities in the terahertz range: optical feedback effects on quantum cascade lasers”, **A.Campa**, L. Consolino, M. Ravaro, D. Mazzotti, M. S. Vitiello, S. Bartalini, and P. De Natale*, 11th International User Meeting and Summer School on Cavity Enhanced Spectroscopy, 16 – 19 June,2015, Boulder, Colorado, USA.*

‘’QCL-based metrological-grade THz spectroscopy tools‘’, L. Consolino, M. Siciliani de Cumis, D.Mazzotti, **A.Campa**, M. Ravaro, M. S. Vitiello, S. Bartalini, P. Cancio, and P. De Natale *, 2015Conference on Lasers and Electro-Optics (CLEO 2015), San Jose, USA, 10-15 May 2015.*

‘’Towards Doppler-Free QCL-Based THZ Metrology” , L. Consolino, **A.Campa**, S. Bartalini, M. Ravaro,H. E. Beere, D. A. Ritchie, M. S. Vitiello, P. Cancio, D. Mazzotti, P. De Natale*, Convegno italiano delle tecnologie fotoniche, Fotonica 2014, AEIT, Torino 6-8 May 2014.*

‘’QCL-based Metrological-grade THz Spectroscopy Tools”, L. Consolino, M.Siciliani De Cumis, D.Mazzotti, **A.Campa**, M. Ravaro, M. S. Vitiello, S.Bartalini, P.Cancio Pastor, P. De Natale*, Cleo 2015:Conference on Lasers and Electro-Optics, San Jose, CA, USA, 8-13 June.*

"QCL- based Metrological THz Spectroscopy", S. Bartalini, L. Consolino, **A. Campa**, M. Ravaro , H.E. Beere D. A. Ritchie, M. S. Vitiello, P. Cancio, D. Mazzotti, P. De Natale*, International Quantum Cascade Lasers School& Workshop 2014, Policoro (Matera), 7-12 September, 2014.*

‘’Towards Doppler-Free QCL-based Metrological THz Spectroscopy” , L. Consolino, S. Bartalini,**A.Campa**, M. Ravaro, H. E. Beere, D. A. Ritchie, M. S. Vitiello, P. Cancio, D. Mazzotti, P. De Natale,*Convegno italiano delle tecnologie fotoniche, Fotonica 2014, AEIT, Napoli 12-14 May 2014.*

Bibliography

[1]C. Wang, C.Lin, Q.Chen, X.Deng, and J.Zhang, "0.14 THz high speed data communication over 1.5 kilometers", in 37th international conference on infrared, millimeter, and terahertz waves (IEEE, 2012), pp. 1–2.

[2]M.Locatelli, M.Ravaro, S.Bartalini, L.Consolino, M.S.Vitiello, R.Cicchi, F. S. Pavone, and P.DeNatale, "Real time terahertz digital holography with a quantum cascade laser", Scientific Reports **5**, 1–7 (2015).

[3]C.Yu, S.Fan, Y.Sun, and E.P.MacPherson, "The potential of terahertz imaging for cancer diagnosis: a review of investigations to date", Quantitative Imaging in Medicine and Surgery **2**, 33–45 (2012).

[4]J.F.Federici, B.Schulkin, F.Huang, D.Gary, R.Barat, F.Oliveira, and D.Zimdars, "THz imaging and sensing for security applications-explosives, weapons and drugs", Semiconductor Science and Technology **20**, 266–280 (2005).

[5]J.B.Jackson, J.Bowen, G.Walker, J.Labaune, G.Mourou, M.Menu, and K. Fukunaga, "A survey of terahertz applications in cultural heritage conservation science", IEEE Transactions on Terahertz Science and Technology **1**, 220–231 (2011).

[6]Y. C. Shen, T. Lo, P. F. Taday, B. E. Cole, W. R. Tribe, and M. C. Kemp, "Detection and identification of explosives using terahertz pulsed spectroscopic imaging", Applied Physics Letters **86**, 241116–241119 (2005).

[7]L. Testi, M. Zwaan, C. Vlahakis, and S. Corder, "Science verification datasets on the ALMA science portal messenger", Astronomical Science **17**, 59–60 (2012).

[8]M.Bellini, P.DeNatale, G.DiLonardo, L. Fusina, M. Inguscio, and M.Prevedelli, "Tunable far infrared spectroscopy of $16O_3$ ozone", Journal of Molecular Spectroscopy **152**, 256–259 (1992).

[9]F. DeLucia, "The submillimeter: a spectroscopist's view", Journal of Molecular Spectroscopy **261**, 1–17 (2010).

[10]W. Faries, K. A. Gehring, P. L. Richards, and Y. R. Shen, "Tunable far infrared radiation generated from difference frequency between two ruby lasers", Physical Review Journals Achieve **2**, 363–365 (1969).

[11]J. R. Morris and Y. R. Shen, "Far-infrared generation by picosecond pulses in electro-optical materials", Optics Communications **3**, 81–84 (1971).

[12]K. H. Yang, P. L. Richards, and Y. R. Shen, "Generation of far infrared radiation by picosecond light pulses in $LiNbO_3$", Applied Physics Letters **9**, 320–323 (1971).

[13]P.Shumyatsky and R. R. Alfano, "Terahertz sources", Journal of Biomedical Optics **16**, 1–9 (2011).

[14]A. Davies, E. Linfield, and M. Johnston, "The development of terahertz sources and their applications", Physics in Medicine and Biology **47**, 3679–3689 (2002).

[15]M. Belkin and F.Capasso, "New frontiers in quantum cascade lasers: high performance room temperature terahertz sources", Physica Scripta **90**, 18002–18015 (2015).

[16]J.Q.Lu, D.Wu, S.Sengupta, S.Slivken, and M.Razeghi, "Room temperature continuous wave, monolithic tunable THz sources based on highly efficient mid-infrared quantum cascade lasers", Science Report **6**, 23595–23602 (2016).

[17]S. Bartalini, S. Borri, P. Cancio, A. Castrillo, I. Galli, G. Giusfredi, D. Mazzotti, L. Gianfrani, and P. DeNatale, "Observing the intrinsic linewidth of a quantum-cascade laser: beyond the Schawlow-Townes limit", Physical Review Letters **104**, 1–4 (2010).

[18]H.Odashima, M.Tachikawa, L.R.Zink, and K.M.Evenson, "Extension of tunable far-infrared spectroscopy to 7.9 THz", Optics letters **22**, 822–824 (1997).

[19]K. M. Evenson, D.A.Jennings, and F.R.Petersen, "Tunable far-infrared spectroscopy", Applied Physics Letters **44**, 366–370 (1984).

[20]G.Mourou, C.V.Stancampiano, A.Antonetti, and A.Orszag, "Picosecond microwave pulses generated with a subpicosecond laser-driven semiconductor switch", Applied Physics Letters **4**, 295–296 (1981).

[21]V. Wallace, "Terahertz imaging detects cancerous tissue", SPIE Newsroom **10**, 1200812–1200814 (2008).

[22]Y.-S. Lee, *Principles of terahertz science and technology, Chap.1* (Springer, 2008).

[23]G.Piau, F.X.Brown, D.Dangoisse, and P.Glorieux, "Heterodyne detection of tunable FIR sidebands", IEEE Journal of Quantum Electronics **23**, 1388–1391 (1987).

[24]J.VanSlageren, S.Vongtragool, B. Gorshunov, A. A. Mukhin, N. Kar, J. Krzystek, J. Telser, A. Muller, C. Sangregorio, D. Gatteschif, and M. Dressela, "Frequency domain magnetic resonance spectroscopy of molecular magnetic materials", Physical Chemistry Chemical Physics **18**, 3837–3843 (2003).

[25]B. Gorshunov, A. Volkov, I. Spektor, A. Prokhorov, A. Mukhin, M. Dressel, S. Uchida, and A. Loidl, "Terahertz BWO-Spectrosopy", International Journal of Infrared and Millimeter Waves **26**, 1217–1240 (2005).

[26]R. F. Kazarinov and R. A. Suris, "Possibility of the amplification of electromagnetic waves in a semiconductor with a superlattice", Soviet Physics - Semiconductors **5**, 707–709 (1971).

[27]J. Faist, F. Capasso, D. L. Sivco, C. Sirtori, A. L. Hutchinson, and A. Y. Cho, "Quantum cascade laser", Science **264**, 553–556 (1994).

[28]R. Kohler, A. Tredicucci, F. Beltram, H. E. Beere, E. H. Linfield, A. G. Davies, D. A. Ritchie, R. C. Iotti, and F. Rossi, "Terahertz semiconductor heterostructure laser", Nature **417**, 156–159 (2002).

[29]B. S. Williams, "Terahertz quantum-cascade lasers", Nature photonics **1**, 517–525 (2007).

[30]B. S. Williams, "Terahertz quantum cascade lasers", PhD thesis (Massachusetts Institute of Technology, 2003).

[31]M. S. Vitiello, L. Consolino, S. Bartalini, A. Taschin, A. Tredicucci, M. Inguscio, and P. DeNatale, "Quantum-limited frequency fluctuations in a terahertz laser", Nature Photonics **6**, 525–528 (2012).

[32]A. Betz, R. Boreiko, B. Williams, S.Kumar, Q.Hu, and J.L.Reno, "Frequency and phase-lock control of a 3 THz quantum cascade laser", Optical Letters **30**, 1837–1839 (2005).

[33]M.Ravaro, V.Jagtap, G. C.Sirtori, L.Li, S.Khanna, E.H.Linfield, and S.Barbieri, "Continuous-wave coherent imaging with terahertz quantum cascade lasers using electro-optic harmonic sampling", Optics Express **102**, 7525–7532 (2013).

[34]D. Rabanus, U. U. Graf, M. Philipp, O. Ricken, J. Stutzki, B. Vowinkel, M. Wiedner, C. Walther, M. Fischer, and J. Faist, "Phase locking of a 1.5 Terahertz quantum cascade laser and use as a local oscillator in a heterodyne HEB receiver", Optics Express **17**, 1159–1168 (2009).

[35]P. Khosropanah, W. Zhang, J. N. Hovenier, J. R. Gao, T. M. Klapwijk, M. I. Amanti, G. Scalari, and J. Faist, "3.4 thz heterodyne receiver using a hot electron bolometer and a distributed feedback quantum cascade laser", Journal of Applied Physics **104**, 113106–113112 (2008).

[36]A. Danylov, A.R.Light, J.Waldman, N.R.Erickson, X.Qian, and W.D.Goodhue, "2.32 thz quantum cascade laser frequency-locked to the harmonic of a microwave synthesizer source", Optics Express **20**, 27908–27914 (2012).

[37]H.W.Hubers, R. Eichholz, S.G.Pavlov, and H.Richter, "Dispersion in a broadband terahertz quantum cascade laser", Applied Physics Letters **109**, 221107–221111 (2016).

[38]T.Loffler, T.May, C.Weg, A.Alcin, B.Hils, and H.G.Roskos, "Continuous-wave terahertz imaging with a hybrid system", Applied Physics Letters **9**, 091111 (2007).

[39]M. Ravaro, S. Barbieri, G. Santarelli, V. Jagtap, C. Manquest, C. Sirtori, S. Khanna, and E. Linfield, "Measurement of the intrinsic linewidth of terahertz quantum cascade lasers using a near-infrared frequency comb", Optics Express **20**, 25654–25661 (2012).

[40]L.Consolino, S.Jung, A.Campa, M.DeRegis, S.Pal, J.H.Kim, K.Fujita, A.Ito, M.Hitaka, S.Bartalini, P.DeNatale, M. A. Belkin, and M. Vitiello, "Spectral purity and tunability of terahertz quantum cascade laser sources based on intracavity difference-frequency generation", Science Advances **9**, 1–8 (2017).

[41]F. Sizov, "THz radiation sensors", Opto-electronics review **18**, 10–36 (2010).

[42]S. Haroche, "Nobel lecture: controlling photons in a box and exploring the quantum to classical boundary", Reviews of Modern Physics **85**, 1083–1102 (2013).

[43]G. Gagliardi and H. Loock, *Cavity-enhanced spectroscopy and sensing* (Springer Series in Optical Sciences, 2014).

[44]S. Kuhr, S. Gleyzes, C. Guerlin, J. Bernu, U.B.Hoff, S.Deleglise, S.Osnaghi, M.Brune, J.M.Raimond, S. Haroche, E. Jacques, P. Bosland, and B. Visentin, "Ultrahigh finesse Fabry–Perot superconducting resonator", Applied Physics Letters **90**, 164101–164103 (2014).

[45]G. A. Gary, E. A. West, D. Rees, J. A. McKay, M. Zukic, and P. Herman, "Solar CIV vacuum-ultraviolet Fabry–Perot interferometers", Astronomy and Astrophysics **461**, 707–722 (2007).

[46]A. A. Savchenkov, A. B. Matsko, V. S. Ilchenko, and L. Maleki, "Optical resonators with ten million finesse", Optics Express **15**, 6768–6773 (2007).

[47]B. A. Saleh and M.C.Teich, *Fundamentals of photonics, Chap.10* (Wiley Interscience, 2007).

[48]D. Romanini, A. A. Kachanov, N. Sadeghi, and F. Stoeckel, "CW cavity ring down spectroscopy", Chemical Physics Letters **264**, 316–322 (1997).

[49]A. O'Keefe and D. Deacon, "Cavity ring-down optical spectrometer for absorption measurements using pulsed laser sources", Review of Scientific Instruments **23**, 2544–2554 (1988).

[50]B. A. Paldus, C. C. Harb, T. G. Spence, R. N. Zare, C. F. Gmachl, F. Capasso, D. L. Sivco, J. N. Baillargeon, A. L. Hutchinson, and A. Y. Cho, "Cavity ringdown spectroscopy using mid-infrared quantum-cascade lasers", Optics Letters **25**, 666–668 (2000).

[51]G. Giusfredi, S. Bartalini, S. Borri, P. Cancio, I. Galli, D. Mazzotti, and P. DeNatale, "Saturated-absorption cavity ring-down spectroscopy", Physical Review Letters **104**, 110801–110804 (2010).

[52]L. A. Surin, B. S. Dumesh, F. Lewen, D. A. Roth, V. P. Kostromin, F. S. Rusin, G. Winnewisser, and I. Pak, "Millimeter wave intracavity jet OROTRON spectrometer for investigation of van der waals complexes", Review of Scientific Instruments **72**, 2535–2542 (2001).

[53]P.Maddaloni, M.Bellini, and P.DeNatale, *Laser-based measurements for time and frequency domain applications: a handbook* (CRC Press, 2013).

[54]M. Bellini, P. DeNatale, and M. Inguscio, "Progress in the far infrared pecision spetroscopy", Laser Physics **4**, 408–411 (1994).

[55]R. Braakman and G. A. Blake, "Principles and promise of Fabry-Perot resonators at terahertz frequencies", Laser Physics **109**, 063102–063111 (2011).

[56]A.Campa, L.Consolino, M.Ravaro, D.Mazzotti, M.S.Vitiello, S.Bartalini, and P.DeNatale, "High-Q resonant cavities for terahertz quantum cascade lasers", Optics Express **23**, 3751–3761 (2015).

[57]P.F.Goldsmith, *Quasioptical system gaussian, Chap.5* (Springer, 1997).

[58]L.Consolino, A.Campa, M.Ravaro, D.Mazzotti, M.S.Vitiello, S.Bartalini, and P.DeNatale, "Saturated absorption in a rotational molecular transition at 2.5 THz using a quantum cascade laser", Applied Physical Letter **106**, 021108–021112 (2015).

[59]U. Gravitational Wave Group Birmingham, *Frequency domain INterfErometer Simulation SoftwarE (Finesse)* (http://www.gwoptics.org/finesse).

[60]S. Bartalini, L. Consolino, P. Cancio, P. DeNatale, P. Bartolini, A. Taschin, M. DePas, H.Beere, D. Ritchie, M. Vitiello, and R. Torre, "Frequency comb assisted terahertz quantum cascade laser spectroscopy", Physical Review X **4**, 021006–021013 (2004).

[61]L. Consolino, A. Taschin, P. Bartolini, S. Bartalini, P. Cancio, A. Tredicucci, H. Beere, D. Ritchie, R. Torre, M. Vitiello, and P. DeNatale, "Phase-locking to a free-space terahertz comb for metrological-grade terahertz lasers", Nature Communications **3**, 1040–1044 (2012).

[62]R.Holzwarth, Th.Udem, T. W.Hansch, J. C. Knight, W. J.Wadsworth, and P. S. J.Russell, "Optical frequency synthesizer for precision spectroscopy", Physical Review Letters **85**, 2264–2267 (2000).

[63]T. W. Hansch, "Nobel lecture: passion for precision", Reviews of Modern Physics **7820**, 6851–6859 (2006).

[64]T. Udem, R. Holzwarth, and T. W. Hansch, "Optical frequency metrology", Nature **416**, 233–237 (2002).

[65]P.Maddaloni, P.Cancio, and P.DeNatale, "Optical comb generators for laser frequency measurement", Measurement Science and Technologies **20**, 1–18 (2009).

[66]L. Consolino, A. Taschin, P. Bartolini, S. Bartalini, P. Cancio, A. Tredicucci, H. E. Beere, D. A. Ritchie, R. Torre, M. S. Vitiello, and P. DeNatale, "Phase locking to a free space terahertz comb for metrological grade terahertz lasers", Nature Communications **3**, 1040 (2012).

[67]M. I. Bakunov, S. B. Bodrov, and M. V. Tsarev, "Terahertz emission from a laser pulse with tilted front: phase matching versus Cherenkov effect", Review of Scientific Instruments **69**, 1236–1239 (1998).

[68]J. Hebling, A. Stepanov, G. Almasi, B. Bartal, and J. Kuhl, "Tunable THz pulse generation by optical rectification of ultrashort laser pulses with tilted pulse fronts", Applied Physics B **78**, 593–599 (2004).

[69]G.Ramakrishnan and P.C.M.Planken, "Percolation-enhanced generation of terahertz pulses by optical rectification on ultrathin gold films", Optics Letters **36**, 2572–2574 (2011).

[70]A. Tomasino, A. Parisi, S. Stivala, P. Livreri, A. C. Cino, A. C. Busacca, M. Peccianti, and R. Morandotti, "Wideband thz time domain spectroscopy based on optical rectification and electro-optic sampling", Scientific Reports **3**, 1–8 (2013).

[71]T. Loffler, T. Hahn, M. Thomson, F. Jacob, and H. G. Roskos, "Large-area electro-optic znte terahertz emitters", Optics Express **13**, 5353–5362 (2005).

[72]M. I. Bakunov, S. B. Bodrov, A. V. Maslov, and M. Hangyo, "Strongly subluminal regime of optical to terahertz conversion in gap", Journal of Applied Physics **105**, 133–141 (2009).

[73]S. B. Bodrov, M. I. Bakunov, and M. Hangyo, "Efficient cherenkov emission of broadband terahertz radiation from an ultrashort laser pulse in a sandwich structure with nonlinear core", Journal of Applied Physics **101**, 093105 (2008).

[74]M. I. Bakunova, E. A. Mashkovich, M. V. Tsarev, and S. D. Gorelov, "Efficient Cherenkov-type terahertz generation in Si-prism-LiNbO3-slab structure pumped by nanojoule-level ultrashort laser pulses", Applied Physical Letters **101**, 151102 (2012).

[75]G. Gallot, J. Zhang, R. W. McGowan, T. Jeon, and D. Grischkowsky, "Measurements of the THz absorption and dispersion of ZnTe and their relevance to the electro-optic detection of THz radiation", Applied Physical Letters **74**, 3450–3452 (1999).

[76]K. Suizua, T. Shibuya, and K. Kawase, *Cherenkov phase matched monochromatic tunable terahertz wave generation*, Vol. Optics and Lasers (Recent Optical and Photonic Technologies, Chap. 7, 2010).

[77]T. E. Stevens, J. K. Wahlstrand, J. Kuhl, and R. Merlin, "Cherenkov radiation at speeds below the light threshold: phonon-assisted phase matching", Science **291**, 627–630 (2001).

[78]D. H. Auston, K. P. Cheung, J. A. Valdmanis, and D. A. Kleinman, "Cherenkov radiation from femtosecond optical pulses in electro-optic media", Physical Review Letters **53**, 1555–1558 (1984).

[79]J.Z.Xu and X.C.Zhang, "Optical rectification in an area with a diameter comparable to or smaller than the center wavelength of terahertz radiation", Optics letters **27**, 1067–1069 (2002).

[80]J. L'Huillier, G. Torosyan, M. Theuer, Y. Avetisyan, and R.Beigang, "Generation of thz radiation using bulk, periodically and aperiodically poled lithium niobate part 1: theory", Applied Physics B **86**, 185–196 (2007).

[81]Y.-S. Lee, T. Meade, M. DeCamp, T. Norris, and A. Galvanauskas, "Temperature dependence of narrow-band terahertz generation from periodically poled lithium niobate", Applied Physics Letters **77**, 1244–1246 (2000).

[82]A. G. Stepanov, J. Hebling, and J. Kuhl, "Efficient generation of subpicosecond terahertz radiation by phase-matched optical rectification using ultrashort laser pulses with tilted pulse fronts", Applied physics letters **83**, 3000–3002 (2003).

[83]F.Trager, *Handbook of lasers and optics, Chap.12* (Springer).

[84]S.Jung, A.Jiang, Y.Jiang, K.Vijayraghavan, X.Wang, M.Troccoli, and M. A. Belkin, "Broadly tunable monolithic room-temperature terahertz quantum cascade laser sources", Nature Communications **5**, 4267–4274 (2014).

[85]S. Bartalini, L. Consolino, P. Cancio, P. DeNatale, P. Bartolini, a. Taschin, M. DePas, H. Beere, D. Ritchie, M. S.Vitiello, and R. Torre, "Frequency-comb-assisted terahertz quantum cascade laser spectroscopy", Physical Review X **4**, 021006–021007 (2014).

[86]S. Barbieri, P.Gellie, G.Santarelli, L.Ding, W.Maineult, C.Sirtori, R.Colombelli, H.Beere, and D.A.Ritchie, "Phase-locking of a 2.7-THz quantum cascade laser to a mode-locked erbium-doped fibre laser", Nature Photonics **4**, 636–40 (2010).

[87]M. Tonouchi, "Cutting-edge terahertz technology", Nature Photonics **1**, 97–105 (2007).

[88]L. Tombez, S. Schilt, J. DiFrancesco, P. Thomann, and D. Hofstetter, "Temperature dependence of the frequency noise in a mid-IR DFB quantum cascade laser from cryogenic to room temperature", Optics Express **20**, 6851–6859 (2012).

[89]S.Bartalini, S.Borri, I.Galli, G.Giusfredi, D.Mazzotti, T.Edamura, N.Akikusa, M.Yamanishi, and P.DeNatale, "Measuring frequency noise and intrinsic linewidth of a room-temperature dfb quantum cascade laser", Optics express **19**, 17996–18003 (2011).

[90]S. Borri, S. Bartalini, P. C. Pastor, I. Galli, G. Giusfredi, D. Mazzotti, M. Yamanishi, and P. DeNatale, "Frequency-noise dynamics of mid-infrared quantum cascade lasers", IEEE Journal of Quantum Electronics **47**, 984–988 (2011).

[91]G. DiDomenico, S.Schilt, and P.Thomann, "Simple approach to the relation between laser frequency noise and laser line shape", Applied Optics **49**, 4801–4807 (2015).

[92]H. Li, P. Laffaille, D. Gacemi, M. Apfel, C. Sirtori, J. Leonardon, G. Santarelli, M. Rosch, G. Scalari, M. Beck, J. Faist, W. Hansel, R. Holzwarth, and S. Barbieri, "Dynamics of ultra-broadband terahertz quantum cascade lasers for comb operation", Optics Express **23**, 33270–33294 (2015).

[93]J.Faist, G.Villares, G.Scalari, M.Rosch, C.Bonzon, A.Hugi, and M.Beck, "Quantum cascade laser frequency combs", Nanophotonics **5**, 272–291 (2016).

[94]Wolfram, *Mathematica* (https://www.wolfram.com/mathematica/).

[95]D. R. Walker, T. Udem, C. Gohle, B. Stein, and T. W. Hansch, "Frequency dependence of the fixed point in a fluctuating frequency comb", Conference on Lasers and Electro-Optics and 2008 Conference on Quantum Electronics and Laser Science **89**, 535–538 (2008).